



저작자표시-비영리-변경금지 2.0 대한민국

이용자는 아래의 조건을 따르는 경우에 한하여 자유롭게

- 이 저작물을 복제, 배포, 전송, 전시, 공연 및 방송할 수 있습니다.

다음과 같은 조건을 따라야 합니다:



저작자표시. 귀하는 원저작자를 표시하여야 합니다.



비영리. 귀하는 이 저작물을 영리 목적으로 이용할 수 없습니다.



변경금지. 귀하는 이 저작물을 개작, 변형 또는 가공할 수 없습니다.

- 귀하는, 이 저작물의 재이용이나 배포의 경우, 이 저작물에 적용된 이용허락조건을 명확하게 나타내어야 합니다.
- 저작권자로부터 별도의 허가를 받으면 이러한 조건들은 적용되지 않습니다.

저작권법에 따른 이용자의 권리는 위의 내용에 의하여 영향을 받지 않습니다.

이것은 [이용허락규약\(Legal Code\)](#)을 이해하기 쉽게 요약한 것입니다.

[Disclaimer](#)

Doctoral Thesis

Morphology Control of Photoactive Layer for Highly
Efficient Perovskite solar cells

Jaeki Jeong

Department of Energy Engineering

Graduate School of UNIST

2019

Morphology Control of Photoactive Layer for Highly Efficient Perovskite solar cells

Jaeki Jeong

Department of Energy Engineering

Graduate School of UNIST

Morphology Control of Photoactive Layer for Highly Efficient Perovskite solar cells

A thesis/dissertation
submitted to the Graduate School of UNIST
in partial fulfillment of the
requirements for the degree of
Doctor of Philosophy

Jaeki Jeong

Month/Day/Year of submission

Approved by



Advisor

Jin Young Kim


Morphology Control of Photoactive Layer for Highly Efficient Perovskite solar cells

Jaeki Jeong

This certifies that the thesis/dissertation of Jaeki Jeong is approved.

12/13/2018

signature




Advisor: Jin Young Kim

signature



Sang Il Seok: Thesis Committee Member #1

signature




Myoung Hoon Song: Thesis Committee Member #2

signature



Hyunhyub Ko: Thesis Committee Member #3

signature



Dong Suk Kim: Thesis Committee Member #4

Abstract

Considerable effort to develop renewable energy sources has been expended over the last several decades, leading to the demonstration of several new classes of highly efficient photovoltaic cells. organic, inorganic and hybrid light absorbers such as organic bulk heterojunctions, colloidal quantum-dots and dye-sensitized metal oxide devices have been demonstrated as next generation photovoltaic materials. Among them, hybrid organic-inorganic perovskite materials have attracted substantial attention as photovoltaic light absorbers due to their outstanding electrical and optical properties. Since the processing for obtaining compact and uniform perovskite photoactive layer has intensively studied last few years to achieve high PCEs in solar cells, recent PCEs of perovskite solar cells (PeSCs) have exceeded 23% which is approaching those of commercialized PVs. These achievements have been marked by a constant improvement of deposition techniques by understanding of the crystallization processes. In this perspective, here, we demonstrate several deposition techniques which has a great influence on the crystallization kinetics.

First, p-i-n structure PeSCs by optimizing the morphology of perovskite films via solvent mixtures in which all layers are deposited with solution processing at low temperature. we employ a simple device configuration of indium tin oxide (ITO)/poly(3,4-ethylenedioxythiophene):polystyrene sulfonic acid (PEDOT:PSS)/CH₃NH₃PbI₃ perovskite/PCBM/aluminum (Al). Improved morphology is obtained in the perovskite film deposited from mixed solvents, leading to improved exciton dissociation efficiency and reduced recombination losses at the interface between perovskite and PCBM and improvements in device efficiency to over 6%.

Second, we employed cesium-doped methylammonium lead iodide perovskites (Cs_xMA_{1-x}PbI₃) photoactive layer to improve the performance of planar heterojunction PeSCs. The Cs_xMA_{1-x}PbI₃ perovskite with optimized 10% Cs doping concentration remarkably improves device efficiency from 5.51% to 7.68% due to increases in short-circuit current density and open-circuit voltage by improving light absorption at optimum device thickness and morphology of perovskite film, and widening the energy difference between energy difference between the valence band of the perovskite and low unoccupied molecular orbital level of PCBM

Third suggestion is a bridged ternary halide approach to process materials with the formula MAPbI₃_{1-y-x}Br_yCl_x which yields high PCEs in planar, p-i-n type heterojunction PeSCs. This ternary halide perovskite system improves device performance from 12% to 16% when an optimal concentration of 10% Br is incorporated into the binary Cl – I systems, via increases in short-circuit current density (J_{SC}), open-circuit voltage (V_{OC}) and fill factor (FF) which arise from the formation of homogeneous crystal

domains and a subtle widening of the optical band gap. Remarkably, the ternary halide perovskite devices exhibited approximately 100% internal quantum efficiency (IQE) throughout their entire absorption range (400~800 nm).

Furthermore, high quality crystal growth of perovskite layer is critical point to enhance device performance. An easy and effective new process for high efficiency p-i-n planar heterojunction structure of PeSCs by handling the compact seed perovskite layer (CSPL). The CSPL assists vertical growth of perovskite crystal and obtains the high crystalline perovskite photoactive layer which leads to the reduction in the charge transfer resistance and longer photoluminescence lifetime. PeSC device with CSPL shows the remarkably improved PCEs from 15.07% to 19.25% with V_{OC} of 1.16 V in p-i-n structure with pure crystal perovskite and negligible current density-voltage hysteresis. And 20.37% was achieved with CSPL assisted n-i-p structure PeSCs

Finally, Lightweight and flexible photovoltaic devices have attracted great interest for specific potential applications, such as miniaturized drones, blimps, and aerospace electronics. This study aims to demonstrate ultralight and flexible perovskite solar cells (PSCs) with orthogonal silver nanowire (AgNW) transparent electrodes fabricated on 1.3- μm -thick polyethylene naphthalate foils. The smooth surface morphologies of the orthogonal AgNW transparent electrodes help prevent nonconducting silver halide formation generated by chemical reaction between the AgNWs and iodine in the active layer. The resultant PSCs with orthogonal AgNW transparent electrodes exhibit substantially improved device performance, achieving a power conversion efficiency (PCE) of 15.18%, over PSCs with random AgNW network electrodes (10.3% PCE). Moreover, ultralight and flexible PSCs with the orthogonal AgNW electrodes exhibit an excellent power-per-weight of $29.4 \text{ W}\cdot\text{g}^{-1}$, which is the highest value reported for a lightweight solar cell device. These lightweight energy harvesting platforms can be further expanded for various wearable optoelectronic devices.

Table of Contents

Abstract	i
List of Figures	iv
List of Tables	xi
Abbreviation	xiii
CHAPTER 1. Introduction	1
CHAPTER 2. Background theory and device physics for perovskite Solar Cells	5
2.1 Properties of perovskite materials	5
2.2 Working principle of perovskite solar cells.....	7
2.3 Crystallization process of perovskite films	10
2.4 Figures of merit of thin film solar cells	14
CHAPTER 3. Mixed solvents for the Optimization of Morphology in Solution-processed, Inverted-Type Perovskite/Fullerene Hybrid Solar Cells	19
3.1 Research background.....	19
3.2 Experimental details	21
3.3 Results and discussion	22
3.4 Conclusion.....	31
CHAPTER 4. Cesium-Doped Methylammonium lead Iodide Perovskite Light Absorber for Hybrid Solar cells	32
4.1 Research background.....	32
4.2 Experimental details	34
4.3 Results and discussion	35
4.4 Conclusion.....	46

CHAPTER 5. Ternary Halide Perovskites for Highly Efficient Solution-Processed Hybrid Solar Cells	47
5.1 Research background.....	47
5.2 Experimental details	49
5.3 Results and discussion.....	51
5.4 Conclusion.....	62
CHAPTER 6. The introduction of perovskite seed layer for high performance perovskite solar	63
6.1 Research background.....	63
6.2 Experimental details	65
6.3 Results and discussion.....	67
6.4 Conclusion.....	78
CHAPTER 7. Ultrathin, Lightweight and Flexible Perovskite Solar Cells with an Excellent Power-Per-Weight Performance.....	79
7.1 Research background.....	79
7.2 Experimental details	81
7.3 Results and discussion.....	83
7.4 Conclusion.....	95
CHAPTER 8. Summary.....	96
References	98
Acknowledgements	104

List of Figures

Figure 1. 1. Solar cells convert light energy into electrical energy by photovoltaic effect.	1
Figure 1. 2. 12% conversion efficiency arrived in land from the sun cover the demand of energy in 2050.....	2
Figure 1. 3. Research object.....	3
Figure 2. 1. Materials properties of perovskite	5
Figure 2. 2. Basic device structure of perovskite solar cells	7
Figure 2. 3. Working principle of p-i-n structure perovskite solar cells.....	8
Figure 2. 4. Various perovskite deposition method.....	10
Figure 2. 5. Morphology of perovskite films with various solvent.....	12
Figure 2. 6. Solar irradiance of AM1.5G and AM 1.0. Photon flux density of AM 1.5G and maximum photocurrent density of the device absorbing light up to corresponding wavelength are shown in the right of the figure.....	14
Figure 2. 7. Equivalent circuit of a solar cell	15
Figure 2. 8. J - V characteristics of solar cell under illumination.....	17
Figure 2. 9. An example of external quantum efficiency and integrated JSC of solar cell.	18
Figure 3. 1. (a) Device structure. (b) Energy band diagram of p-i-n structure PeSCs.	22
Figure 3. 2. (a-c) SEM top-view. (d-f) AFM topography images of CH ₃ NH ₃ PbI ₃ perovskite films from different solvents.....	23
Figure 3. 3. (a) UV-vis absorption spectra. (b) XRD patterns of CH ₃ NH ₃ PbI ₃ perovskite films from different solvents.....	24
Figure 3. 4. (a) UV-vis absorption spectra. (b) XRD patterns of CH ₃ NH ₃ PbI ₃ perovskite films from different solvents.....	25

Figure 3. 5. (a) J-V characteristics (b) EQE and IQE of p-i-n structure PeSCs prepared from different solvents. 27

Figure 3. 6. J-V curves of p-i-n structure PeSCs prepared from different solvents with various DMF:GBL ratio. 28

Figure 3. 7. Dependence of photovoltaic parameters (J_{SC} , V_{OC} , FF, and PCE) on the amount of GBL in mixed solvent of DMF and GBL. 29

Figure 3. 8. TEM cross-sectional images of p-i-n structure PeSCs prepared from a) GBL, b) DMF, and c) mixed solvent. 30

Figure 4. 1. (a) Crystal structure and (b) XRD patterns of MAPbI₃ and Cs doped MAPbI₃ perovskites. 35

Figure 4. 2. (a) UV-vis absorption and (b) transformed Kuberka-Munk spectra of CsXMA_{1-X}PbI₃ perovskite films with different Cs ratio. 36

Figure 4. 3. (a, b) SEM and (c, d) AFM topography images of MAPbI₃ and Cs_{0.1}MA_{0.9}PbI₃ perovskite films. Scale bar is 1 μm. 38

Figure 4. 4. (a, b) SEM top view images and (c, d) elemental mapping by energy dispersive spectroscopy (EDS) of MAPbI₃ and Cs_{0.1}MA_{0.9}PbI₃ perovskite films. Scale bar is 1 μm 38

Figure 4. 5. (a) *J-V* characteristics and (b) EQE of the devices with Cs_XMA_{1-X}PbI₃ perovskite with different Cs ratio. 40

Figure 4. 6. Secondary edge regions for MAPbI₃ and Cs_{0.1}MA_{0.9}PbI₃ perovskite fillms on PEDOT:PSS-coated ITO substrates. 42

Figure 4. 7. UV-vis absorption spectra of MAPbI₃ and Cs_{0.1}MA_{0.9}PbI₃ perovskite films with optimum device thicknesses. 42

Figure 4. 8. Comparison between the change in absorption (Δ absorption) and EQE enhancement (Δ EQE) for devices using MAPbI₃ and Cs_{0.1}MA_{0.9}PbI₃ perovskites. 43

Figure 4. 9. Long-term stability of devices with MAPbI₃ and Cs_{0.1}MA_{0.9}PbI₃ perovskites under ambient conditions (temperature: 20 °C and humidity: 11%). 43

Figure 4. 10. Cross-sectional TEM images of the devices with (a) MAPbI₃ and (b) CsMAPbI₃ perovskite films as light absorber. Scale bar is 100 nm. 44

Figure 4. 11. AFM topography images of PCBM films spin-coated on top of MAPbI₃ and Cs_{0.1}MA_{0.9}PbI₃ perovskite layers. The scale bar is 1 μm. 45

Figure 5. 1. (a) Absorption coefficient and (b) transformed Tauc-plot spectra of MAPbI_{3-y-x}Br_yCl_x perovskite films with variable Br content. (c) X-ray diffraction (XRD) patterns of perovskite films with (d) a magnified region corresponding to the tetragonal (220) and cubic (200) peaks of MAPbI_{3-y-x}Br_yCl_x (y = 0, 0.1, 0.3, 0.5, 1) system. 51

Figure 5. 2. (a) Normalized UV-vis absorption and (b) Transformed Extinction coefficient of ternary halide perovskite films with different Br ratios. 52

Figure 5. 3. XRD diffraction patterns for MAPbI_{2.9-x}Br_{0.1}Cl_x ternary halide perovskite films deposited on glass substrates. 53

Figure 5. 4. (a-e) SEM top-view images of MAPbI_{3-y-x}Br_yCl_x (y = 0, 0.1, 0.3, 0.5, 1) perovskite films prepared with different Br ratios. (f) SEM cross-sectional image of MAPbI_{2.9-x}Br_{0.1}Cl_x. 54

Figure 5. 5. (a) X-ray photoelectron spectra (XPS) of MAPbI_{3-y-x}Br_yCl_x (y = 0, 0.1, 0.3, 0.5, 1) films in the region of the Br 3d peak. Ultraviolet photoelectron spectra (UPS) of (b) the secondary edge region and (c) Fermi edge region of MAPbI_{3-y-x}Br_yCl_x (y = 0, 0.1, 0.3, 0.5, 1) films, plotted relative to an Au reference. (d) Band diagram of MAPbI_{3-y-x}Br_yCl_x perovskite films. 55

Figure 5. 6. Cl2p region of XPS spectrum of an optimized ternary halide perovskite film. 56

Figure 5. 7. (a) *J-V* characteristics and (b) EQE spectra of MAPbI_{3-y-x}Br_yCl_x (y = 0, 0.1, 0.3, 0.5, 1) perovskite films with different Br ratios and (c) IQE of MAPbI_{3-y-x}Br_yCl_x (y = 0, 0.1) (c) Full device absorption and (d) Internal quantum efficiency of MAPbI_{3-y-x}Br_yCl_x (y = 0, 0.1). 57

Figure 5. 8. Comparison of *J-V* characteristics of an optimized device in different scanning directions. 59

Figure 5. 9. Histogram of device statistics from a total of 333 solar cell devices comprising $\text{MAPbI}_{3-y-x}\text{Br}_y\text{Cl}_x$ ($y = 0, 0.1$) perovskite films with different Br ratios. (a) Short circuit current density, (b) open circuit voltage, (c) fill factor and (d) power conversion efficiency. 61

Figure 6. 1. Energy band diagram of perovskite solar cells. 67

Figure 6. 2. (a) Schematic process of perovskite fabrication, first compact seed perovskite layer (CSPL) deposition on PTAA substrate then perovskite photoactive layer coated on CSPL and cross-sectional SEM image of perovskite film (b) without CSPL, (c) with PbI_2 seed layer and (d) with CSPL. 67

Figure 6. 3. XPS result of PTAA control substrate, PbI_2 seed layer and CSPL films respectively in height direction, after washed by DMF solvent, in width direction, (a)~(c) $\text{Br}3d$, (d)~(f) $\text{Pb}4f$ and (g)~(i) $\text{I}3d$ peak position. 68

Figure 6. 4. XPS survey spectrum of PTAA control, PbI_2 seed layer and CSPL films after washing by DMF solvent. 69

Figure 6. 5. Atomic force microscope (AFM) surface image of PEDOT control substrate, PbI_2 , CSPL films respectively, after washed by DMF solvent. 69

Figure 6. 6. Two-dimensional grazing incidence wide angle X-ray scattering (2D-GIWAXS) images on the substrates after washed by DMF solvent (a) $\text{MAPbBr}_x\text{I}_{3-x}$, (b) PbI_2 and (c) CPSL film. 2D-GIWAXS patterns corresponding line-cuts in (d) in-plane and (e) out-of-plane directions of $\text{MAPbBr}_x\text{I}_{3-x}$, PbI_2 , and CPSL film respectively. 70

Figure 6. 7. Charge recombination and transport characteristics: light intensity dependence of (a) J_{sc} (b) V_{oc} of perovskite device and (c) impedance spectroscopy and (d) Time correlated single photon counting (TCSPC) of perovskite film without and with CSPL. 71

Figure 6. 8. J-V characteristics of perovskite solar cells without and with CSPL including forward and reverse scan direction of (a) p-i-n structure and (b) n-i-p structure. And PCE histogram of (c) p-i-n structure and (d) n-i-p structure devices statistics from a total of 30 solar cell devices respectively comprising without and with CSPL. 72

Figure 6. 9. EQE and calculated J_{sc} of p-i-n structure and n-i-p structure of CSPL perovskite solar cells.
 (p-i-n w/o CSPL: 17.25 $J_{sc}(\text{mAcm}^{-2})$, p-i-n w/ CSPL: 20.05 $J_{sc}(\text{mAcm}^{-2})$, n-i-p w/o CSPL:
 21.13 $J_{sc}(\text{mAcm}^{-2})$, n-i-p w/ CSPL: 22.90 $J_{sc}(\text{mAcm}^{-2})$)..... 73

Figure 6. 10. Characteristics of perovskite solar cells without and with CSPL based on PEDOT:PSS
 HTL..... 74

Figure 6. 11. Histogram of device statistics from a total of 30 p-i-n structure solar cell devices
 (ITO/PTAA/seed layer/MAPbBr_xI_{3-x}/PC61BM/Al) comprising without and with CSPL. (a)
 Short circuit current density, (b) open circuit voltage, (c) fill factor..... 75

Figure 6. 12. Histogram of n-i-p device statistics from a total of 30 solar cell devices (FTO/bl-
 TiO₂/Mesoporous TiO₂+Perovskite((FAPbI₃)_{0.85}(MAPbBr₃)_{0.15})/Spiro-MeOTAD/Au)
 comprising without and with CSPL. (a) Short circuit current density, (b) open circuit
 voltage, (c) fill factor..... 75

Figure 6. 13. Stability test was performed for non-encapsulated cells (with and without CSPL PeSCs)
 under an air about 40% humidity condition..... 76

Figure 7. 1. (a) Schematics of the fabrication procedure for ultrathin orthogonal AgNW transparent
 electrodes produced on 1.3- μm -thick PEN foil. (b) Dark-field optical microscopy image of
 the orthogonal AgNW arrays; the corresponding FFT pattern is shown in the inset. The
 scale bar indicates 40 μm . (c) The ultrathin orthogonal AgNW transparent electrode foil,
 crumpled by a person's finger. (d) An ultrathin and lightweight PSC device mounted onto
 the surface of a leaf. (e) Cross-sectional SEM image of the device structure for a PSC with
 the orthogonal AgNW array. The scale bar is 100 nm. (f-h) Mechanical properties of the
 orthogonal AgNW transparent electrode foils. Variation in resistance of orthogonal AgNW
 electrode foil as a function of (f) bending cycles at a bending radius of 2 mm, (g) crumpling
 cycles, and (h) twisting angles. The inset images show corresponding deformation (twisting,
 crumpling, bending) of the orthogonal AgNW electrode foil adhered to the PDMS thin film
 83

- Figure 7. 2.** Dark-field optical micrograph of a random AgNW network. The fast Fourier transform (FFT) image of the optical micrograph (inset) shows a blurred circular pattern, reflecting the randomness of the corresponding surface geometric structure. The scale bar indicates 40 μm 84
- Figure 7. 3.** The optical transmittance of orthogonal AgNW and random AgNW electrodes deposited onto glass substrates. Samples were scanned over the visible wavelength range (350–800 nm). The corresponding sheet resistances of the electrodes are given in the figure. The glass substrate was used as a reference 85
- Figure 7. 4.** The energy band diagram for the PSC with an orthogonal AgNW electrode. 85
- Figure 7. 5.** (a) Schematic of silver halide formation in PSCs fabricated on random and orthogonal AgNW electrodes. (b,c) AFM images of the surface of PEDOT:PSS coated onto (b) a PH1000/orthogonal AgNW electrode and (c) a PH1000/random AgNW electrode, respectively. (d) Variation in the resistance of both the random and orthogonal AgNW electrodes as a function of the SVA time. (e–h) Mapping images for the binding energy of Ag3d originating from XPS depth profiles of PSCs with orthogonal AgNW and random AgNW electrodes (e,f) before and (g,h) after aging for 10 day 86
- Figure 7. 6.** Tilted SEM images of the surface of PEDOT:PSS coated onto (a) a PH1000/orthogonal AgNW electrode and (b) a PH1000/random AgNW electrode. 87
- Figure 7. 7.** SEM images of the surface of perovskite active layers deposited onto PEDOT:PSS/PH1000/AgNW; the images correspond to different SVA times. 87
- Figure 7. 8.** (a) J–V characteristic and (b) IPCE of PSC devices with ITO, orthogonal AgNW, and random AgNW electrodes. (c) Long-term stability of PSCs under a controlled atmosphere (N₂-filled glove box). (d) The quantitative PCE values of PSCs with ITO, orthogonal AgNW, and random AgNW electrodes. 89
- Figure 7. 9.** J–V hysteresis characteristics of a PSC with ITO, orthogonal AgNW and random AgNW electrode measured with forward and reverse bias 90
- Figure 7. 10.** (a) J–V characteristics of a flexible PSC with an orthogonal AgNW electrode fabricated

on a 1.3- μm -thick PEN foil and a 120- μm -thick PEN film. (b) Photograph of a flexible PSC fabricated on an orthogonal AgNW electrode. (c) An ultralight PSC suspended in bubbles. (d) Comparison of the power-per-weight performances of the ultralight PSC and other types of light solar cells. 92

Figure 7. 11. Variation in normalized device efficiency of PSCs with ITO and orthogonal AgNW electrodes under repeated (1000 times) bending cycles..... 93

Figure 7. 12. Photograph of an ultralight PSC device on an electronic scale, demonstrating its extremely low weight. The device size is 13 mm x 13mm..... 94

List of Tables

Table 3. 1. Characteristics of p-i-n structure PeSCs prepared from different solvents.....	27
Table 3. 2. Characteristics of p-i-n structure PeSCs prepared from different solvents with various DMF: GBL ratio.	28
Table 5. 1. Optical band gaps of MAPbI _{3-y-x} Br _y Cl _x (y = 0, 0.1, 0.3, 0.5, 1) perovskite films with different Br ratios derived from Tauc plots.....	52
Table 5. 2. Valence band (E_V) of MAPbI _{3-y-x} Br _y Cl _x (y = 0, 0.1, 0.3, 0.5, 1) perovskite with different Br ratios from obtained UPS measurements.	56
Table 5. 3. Solar cell characteristics of MAPbI _{3-y-x} Br _y Cl _x (y = 0, 0.1, 0.3, 0.5, 1) perovskite devices with different Br ratios.....	58
Table 5. 4. MAPbI _{2.9-x} Br _{0.1} Cl _x device performance with various thermal annealing temperatures.	58
Table 5. 5. MAPbI _{2.9-x} Br _{0.1} Cl _x device performance with various PC ₆₁ BM thicknesses.....	58
Table 5. 6. Device parameters of optimized devices in different scanning directions.	59
Table 6. 1. Solar cell characteristics of p-i-n and n-i-p structure perovskite solar cells without and with CSPL in forward and reverse scan directions.	72
Table 6. 3. Solar cells characteristic of p-i-n structure perovskite devices without and with and without CSPL based on PEDOT:PSS HTL.....	74
Table 7. 1. J–V characteristics of PSC devices with ITO, orthogonal AgNW, and random AgNW electrodes fabricated on glass substrates.....	90
Table 7. 2. Summarized J–V hysteresis characteristics of a PSC with ITO, orthogonal AgNW and random AgNW electrode measured with forward and reverse bias.....	90
Table 7. 3. Comparison of the device performance of our PSC with orthogonal AgNW arrays and those	

of other AgNW-based PSC devices..... 93

Abbreviation

Abbreviation	Description
PV	photovoltaic
SC	solar cell
PeSC	perovskite solar cell
QD	quantum dot
PSC	polymer solar cell
J_{sc}	short circuit current density
V_{oc}	Open circuit voltage
FF	power conversion efficiency
PCE	power conversion efficiency
CB	conduction band
VB	valance band
HOMO	the highest occupied molecular orbital
LUMO	the lowest occupied molecular orbital
E_g	bandgap
EQE	external quantum efficiency
IPCE	incident photon to electron conversion efficiency
IQE	internal quantum efficiency
P3HT	poly(3-hexylthiophene)
PCBM	phenyl-c61-butyric acid methyl ester
ITO	indium tin oxide
FTO	fluorine-doped tin oxide
AFM	atomic force microscope
XRD	X-ray diffraction
SEM	scanning electron microscopy
XPS	X-ray photoelectron spectrum

BHJ	bulk heterojunction
DSSC	dye-sensitized solar cells
UPS	ultraviolet photoelectron spectrum
CIGS	copper indium gallium sulfide selenide
ETL	electron transport layer
HTL	Hole transport layer
PEDOT:PSS	poly(3,4-ethylenedioxythiophene) polystyrene sulfonate
HSC	hybrid solar cells
MAPbI ₃	CH ₃ NH ₃ PbX ₃ , methyl ammonium lead halides
Spiro-OMeTAD	2,2',7,7'-tetrakis-(N,N-di- <i>p</i> -methoxyphenylamine)-9,9'-spirobifluorenespiro
ICBA	indene-C ₆₀ -bisadduct
EA	ethylammonium
FA	formamidinium
MAPbI _{3-y-x} Br _y Cl _x	CH ₃ NH ₃ PbI _{3-y-x} Br _y Cl _x
E _v	valence band energy
E _{SE}	secondary edge region and
E _{onset}	Fermi edge
CSPL	compact seed perovskite layer
E _{gap}	band gap of the semiconductor
TCSPC	Time correlated single photon counting
V _{bi}	built in potential
AgNW	silver nanowire

CHAPTER 1. Introduction



Figure 1. 1. Solar cells convert light energy into electrical energy by photovoltaic effect.

Demand of renewable energy have been increased for last several decades, there are a lot of resource candidates are nominated for a source of energy. Among them, solar energy is one of the most promising resource due to permanently available and environmentally friendly. If land-based system covered only 2% of the available area and convert energy with 12% efficiency among the huge amount of energy reaching the Earth's surface from the Sun, that energy is more than twice than global energy demand of 30 TW in 2050. After the discovery of photovoltaic effect which occurs when light is absorbed in a material and creates electrical voltage by Edmond Becquerel in 1839, the first solar cells which convert light energy into electrical energy was created by coating selenium with a thin layer of gold with 1-2% energy conversion rate in 1883. The photoelectric effect, leading to Einstein's Nobel Prize, and other fundamental phenomena observed in the semiconductor propagated through modern technology and science such as sensor, photocopy machine, rectifiers and other technologies. From that time on, photovoltaic industry has begun with silicon(Si) which has high quality material with a band gap more suitable for single junction solar cells and PVs based inorganic semiconductors (Si, gallium arsenide(GaAs) and copper indium gallium selenide(CIGS)) have all achieved power conversion efficiencies (PCEs) of over 20%, which is able to commercialize of solar cell technologies. However, inorganic semiconductor based solar cells continue to approach the practical limits for single junction

even though improved material quality and device structure have enabled increased conversion efficiency. In addition, high production cost and module prices are constantly mentioned as a problem. This is the motivation for developing PV technologies with low cost.¹

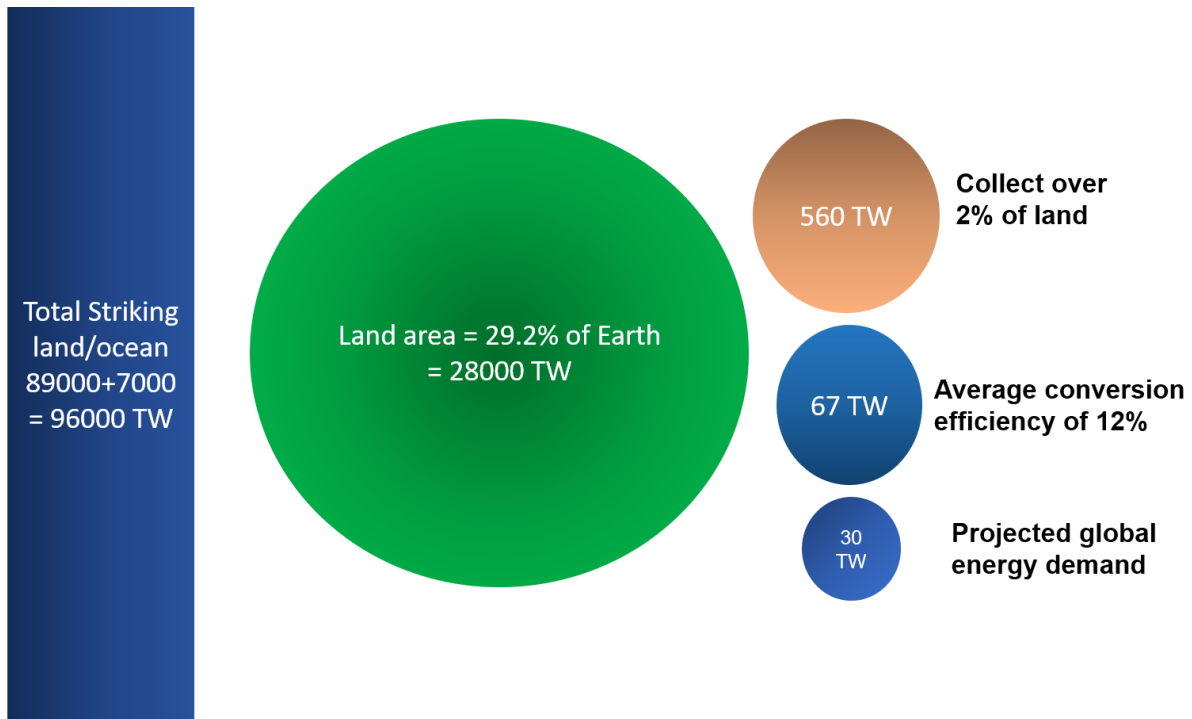


Figure 1. 2. 12% conversion efficiency arrived in land from the sun cover the demand of energy in 2050

In the early of 1990s, Dye sensitized solar cells (DSSCs) have been discovered to potentially meet the requirement of reduction production cost and easy-fabrication. After decade of the efforts, PCEs of DSSC have obtained 10%.² Another attempt is quantum dot solar cells (QDSC) which use quantum dots(QDs) as the light absorbing materials. QDs have band gaps which tunable across a wide range of energy level by changing of QD’s size and this material property is attractive for multi-junction solar cells. The other alternative is organic solar cells (OSC) which uses organic electronics with conductive organic polymer materials and small organic molecules. It has widely investigated owing to lightweight, potentially inexpensive to fabricate, flexible and customizable on the molecular level. However, these alternative PVs have inefficiency and stability problems compared to Si based solar cells.

The emerging class of hybrid organic-inorganic perovskite materials based on lead halides have attracted substantial attention due to their outstanding physical properties such as high absorption coefficients, excellent carrier transport with long electron-hole diffusion lengths, low exciton binding energies and easily tunable energy band gaps.³⁻⁵ These superb physical characteristics have led to high power conversion efficiencies (PCE) since the first research in the area of solution processing perovskite solar cells (PeSCs) was reported in 2009.⁶ To achieve highly efficient PeSCs, the perovskite layer must be deposited with a uniform, highly-crystalline and dense morphology, which completely covers the

underlying surface. Diverse methods such as vapor-assisted deposition, solvent engineering and intermolecular exchange have been introduced to produce uniform perovskite films with large crystal domains and complete surface coverage.⁷⁻⁹ Diverse approaches to improve device performance via control of the film morphology have been introduced, such as via interface engineering, induced crystallization with non-solvents, incorporation of processing additives, nuclei growth and so on. Although, these procedures are excellent guideline for improving film morphology, there have been some drawbacks for each other.

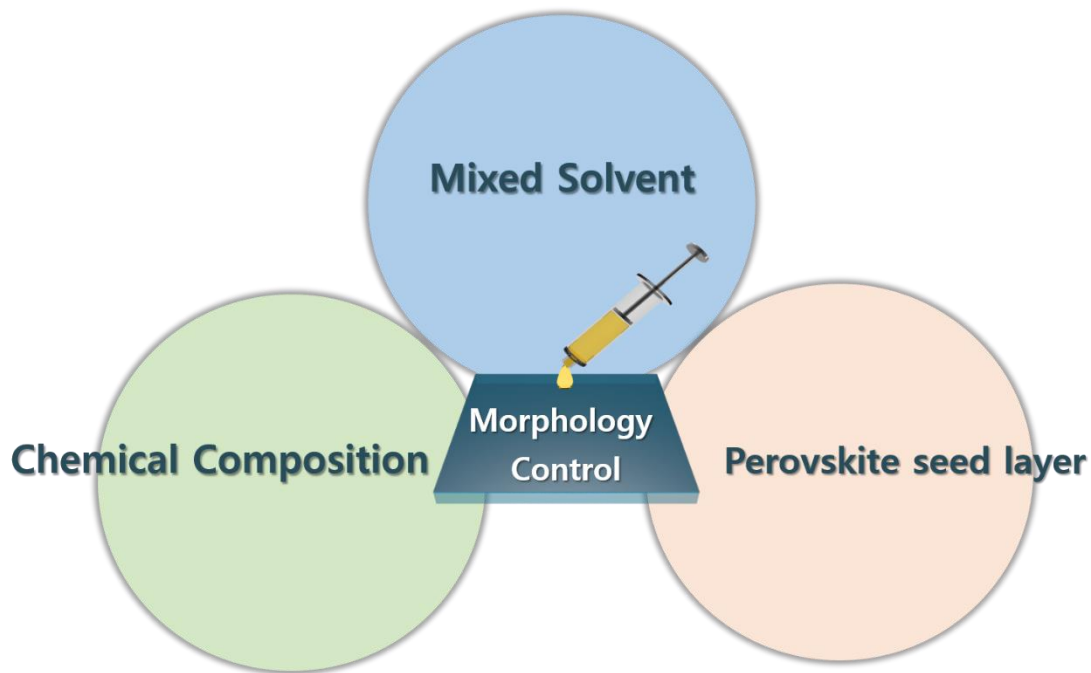


Figure 1. 3. Research object

In this perspective, this thesis is investigated about morphology control of photoactive layer for high efficiency perovskite solar cells. **Chapter 2** begins with introducing background theory to understand basic properties of perovskite materials, working principle of perovskite solar cells and recent efforts to increase perovskite morphology. And then following chapters demonstrate several attempts to control perovskite photoactive layer via newly studied procedures.

In chapter 3, mixed solvent effect is applied to change film morphology. The use of mixed solvents can either take advantage of the difference in solubility of the two solvents and more simply modify the drying kinetics of the system by using higher or lower boiling point solvents. These two main factors lead morphology changes in BHJ polymer solar cells and improved device performance as previously reported study.¹⁰ In this experiment, we used GBL as additive and DMF as main solvent which are widely used in perovskite precursor solvent.

Chapter 4 and 5 is about chemical deposition methods. Perovskites are a class of materials with the same type of crystal structure as ABX_3 . Perovskite materials properties can be easily tuned by exchange

the component composition. In order to modulate film morphology, we tried to exchange components and composition ratio of perovskite photoactive layer. In **chapter 4**, the A site cation MA is replaced with Cs cation, leading to enhancement in device efficiency via improvement in light absorption and morphology as well as an increased energy difference between the valence band of perovskite and LUMO level of PCBM. In **chapter 5**, we have investigated the influence of structural composition on the optoelectronic properties of the materials in order to achieve high-quality, dense perovskite films by fractional substitution of PbCl_2 with PbBr_2 in the precursor solution. Film compositions with Br content ranging from 0 to 1 in the $\text{MAPbI}_{3-x}\text{Cl}_x/\text{DMA}$ system were investigated in order to improve morphology and surface coverage of the perovskite layer.

In **chapter 6**, easy and effective new process for high efficiency p-i-n planar heterojunction structure of perovskite solar cells (PeSCs) by handling the compact seed perovskite layer (CSPL) in **chapter 6**. The CSPL assists vertical growth of perovskite crystal and obtains the high crystalline perovskite photoactive layer which leads to the reduction in the charge transfer resistance and longer photoluminescence lifetime.

Finally, I have demonstrated lightweight and flexible perovskite solar cells via compact seed perovskite layer which is mentioned above. This study aims to apply ultrathin and flexible photovoltaic devices with orthogonal silver nanowire (AgNW) transparent electrodes fabricated on 1.3 μm -thick polyethylene naphthalate foils. The well aligned orthogonal AgNW transparent electrodes help prevent nonconducting silver halide formation generated by chemical reaction between the AgNWs and iodine in the perovskite layer. The resultant PSCs with orthogonal AgNW transparent electrodes exhibit substantially improved device performance, achieving a power conversion efficiency.

The conclusion and outlook of the studies are summarized in the last chapter.

CHAPTER 2. Background theory and device physics for perovskite Solar Cells

This chapter provides theoretical background of device physics on which there is little discussion in each chapter. It covers from operating mechanism of thin film electronics (here, transistors and solar cells) and figures of merit of each thin film device to get a thorough understanding of device application.

2.1 Properties of perovskite materials

In this section, we are going to review the recent studies in understanding the structure property relationships in hybrid perovskite materials. Basically, perovskites are a type of compounds which share the same chemical formula ABX_3 . A as a monovalent cation, B as a divalent cation and a monovalent anion X.¹¹ The choice of component is tunes the optoelectronic properties of the resultant perovskites as well as determines the crystal unit structure. To form a stabilized three-dimensional structure, the choice of component ions can be predicted by the Gold-Schmidt tolerance factor, τ :

$$\tau = \frac{R_X + R_A}{\sqrt{2}(R_X + R_B)} \quad (\text{Eq. 2-1})$$

where R_A , R_B and R_X are the radius of A, B and X ions. It has been known that cubic perovskite is formed when $0.9 \leq \tau \leq 1$, while a rhombohedral and orthorhombic structure is formed with $0.71 \leq \tau \leq 0.9$ and a tetragonal and hexagonal structure is formed with $\tau > 1$.^{12, 13}

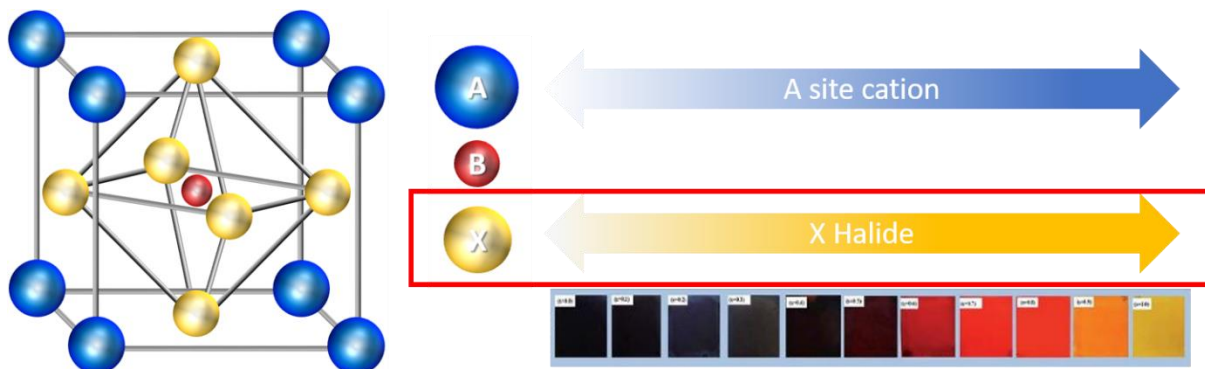


Figure 2. 1. Materials properties of perovskite

Perovskite materials can be easily tuned their optoelectronic properties by changing the composition of the each component. The use of this materials properties, composition modification for bandgap

tuning is a significantly critical component of the construction of performance perovskite devices. In the early of perovskite solar cells, for instance, most common A site organic cation perovskite materials were methylammonium(MA). However, a bandgap of 1.55 eV (MAPbI₃) is not enough because of relatively short absorption range limited to 800 nm. Therefore, the replacement of MA with formamidinium(FA) lead to reduce the bandgap by 0.07 eV, giving risen to an enhancement of the absorption range up to 850 nm.¹⁴

Strong optical absorption is the main factor to the outstanding performance of these perovskite solar cells The absorption coefficient value of CH₃NH₃PbI₃ was estimated to be $1.5 \times 10^4 \text{ cm}^{-1}$ at 550 nm, indication that most incoming light can be absorbed by the perovskite within a thin layer of about 2 mm, which is suitable as a high efficiency solar cells.¹⁵

In addition, perovskite materials exhibit impressive electronic characteristic considering their solution-processed fabrication. By recent reports, the diffusion length of perovskite increased from values below 1 μm to exceeding 10 μm , reflecting the progress that has been obtained with better structural order and morphology.^{4,5} In particular, the diffusion length has a dependence on the grain size of the perovskite film. The carrier mobility of perovskite has been improved over the years and tend to exhibits dependence on film morphology. In perovskite single crystals, the mobility is measured from exceeding $10 \text{ Cm}^2\text{V}^{-1}\text{s}^{-1}$ to above $100 \text{ Cm}^2\text{V}^{-1}\text{s}^{-1}$ with different measuring method.^{9, 16, 17} The mobility does not exhibits a dependence on the material composition.

2.2 Working principle of perovskite solar cells

p-i-n structure: In general, the planar structures can be classified with n-i-p structure and p-i-n structure. The n-i-p planar structure using TiO₂, ZnO and SnO₂ as electron transport layer(ETL) usually show high performance under reverse scan. However, the forward scan usually showed lower efficiency, making it difficult to achieve a reliable power conversion efficiency. In contrast, most studies have reported negligible hysteresis in the planar p-i-n perovskite solar cells with fullerene as ETL. Many groups have reported the reason as follows: first, fullerenes could passivate the trap states to form a fullerene halide radical, which may block the ion migration. Next, fullerenes could diffuse into the perovskite layer via pinhole and grain boundaries, expanding the contact region of perovskite/fullerene interface and reduced the hysteresis. Finally, fullerenes could extract the electrons more efficiently, leading to forestall charge accumulation at the interface removing the hysteresis. Additionally, n-i-p perovskite devices require over 400 °C temperatures to prepare the TiO₂ layer, which currently poses a barrier to economical processing and flexible devices. One more, the n-i-p structure needs a p-type hole conductor which is heavily doped by atmospheric oxygen via incorporation of *tert*-butyl pyridine(tBP) or Li-bis(trifluoromethanesulfonyl)imide (Li-TFSI), which leads to devices with poor chemical stability and sensitivity to moisture. To surmount these obstacle, in this study, the p-i-n architecture is mainly employed.

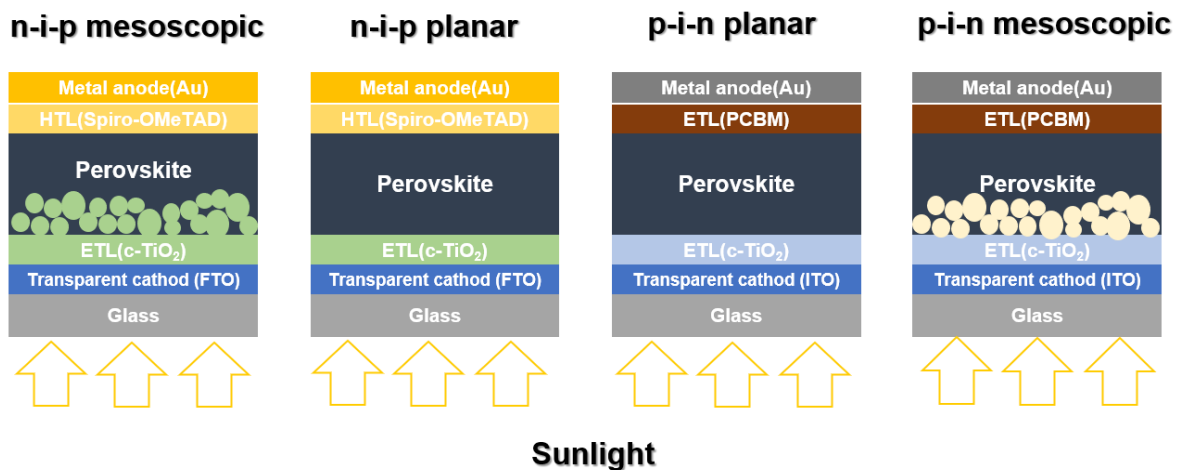


Figure 2. 2. Basic device structure of perovskite solar cells

Working principle of p-i-n structure perovskite solar cells: As mentioned in introduction chapter, solar cells are energy-harvesting devices that directly convert photons to electrons by photovoltaic effect. Photovoltaic is that electrons in ground state are excited to higher energy states when the device is

exposed to irradiation. These excited electrons make potential difference in a material, resulting in the device extracts electrons out of the device generating photocurrent. In this studies. I am concentrating on the p-i-n structure perovskite solar cells, simple working process as followed. Schematic device working mechanism is shown in **Figure 2. 3**. The charge dynamic of p-i-n structure perovskite is happened at the interface including charge extraction, charge transfer and charge recombination.

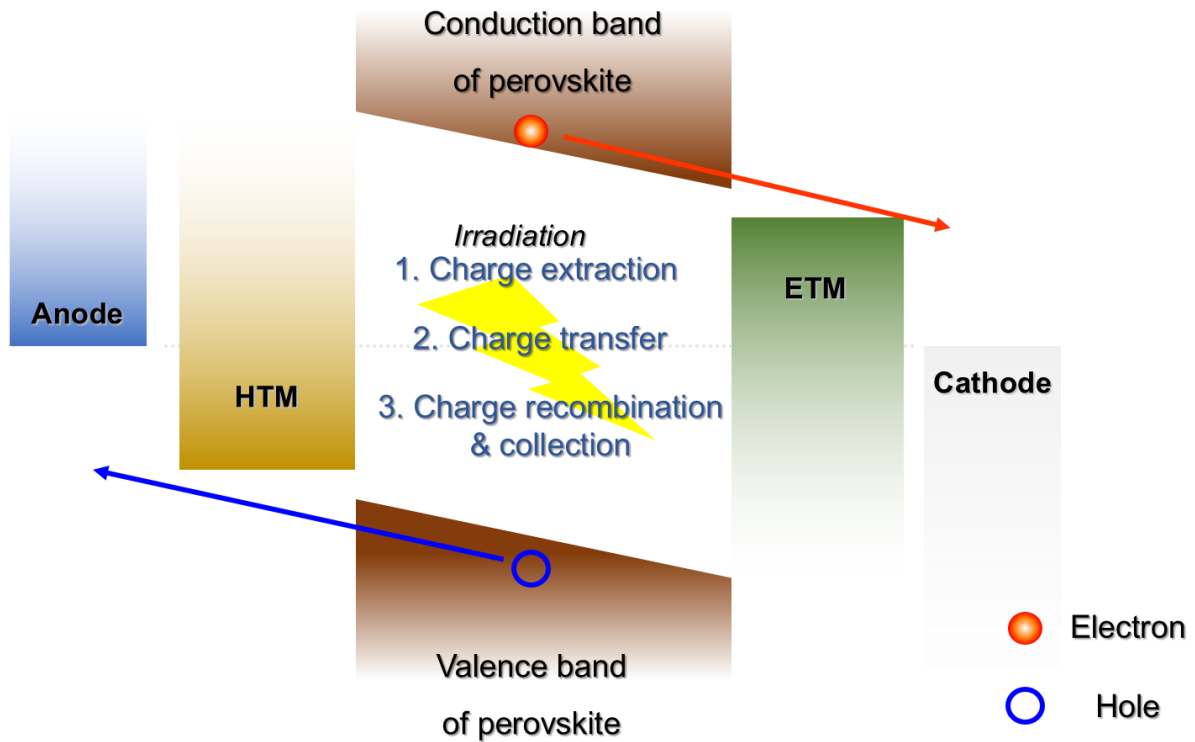


Figure 2. 3. Working principle of p-i-n structure perovskite solar cells

The charge extraction process is a very quick. It is known that within hundreds of ps, the generated electrons and holes could be extracted to the electron transport layer(ETL) and hole transport layer(HTL). Compared with free carrier lifetime that is at the timescale of nanoseconds, the extraction process is ultrafast. However, many literatures demonstrated that the remaining PbI_2 at interface can slow the charge extraction process. The surface modification was investigated to promote the ultrafast interfacial charge extraction. In some works, they used carbon quantum dots acted as superfast electron tunnel, to optimize the interface between ETL and perovskite layer, leading an accelerated charge extraction process which increased the extraction rate from ≈ 300 ps to around 100 ps.

Compared with the charge extraction process, charge transfer and recombination process at the interface have a much more intensive impact on the cell performance like V_{OC} and J_{SC} . Mismatches of interfacial structural and electronic mostly act as the energy barriers for charge transport and recombination, implying that interface engineering is required to eliminate this effect. In the study of

Ogomi et al., they employed HOCO-R-NH₃⁺I⁻ group between ETL and perovskite interface, which highly suppressed the charge recombination from ps to tens of microsecond.

2.3 Crystallization process of perovskite films

In order to modify the morphology of perovskite films and thus the resulting in high performance solar cells, understanding the crystallization is a key factor. Diverse studies showed that it is important to increase the crystalline domains in perovskite solar cells by introducing various crystallization strategies. In this chapter, I will elaborate the various strategies employed so far as summarized figure x. In general, there are a lot of different pathways for crystallization in solution process such as one step method with solvent engineering, two step method like sequential deposition and post processing.

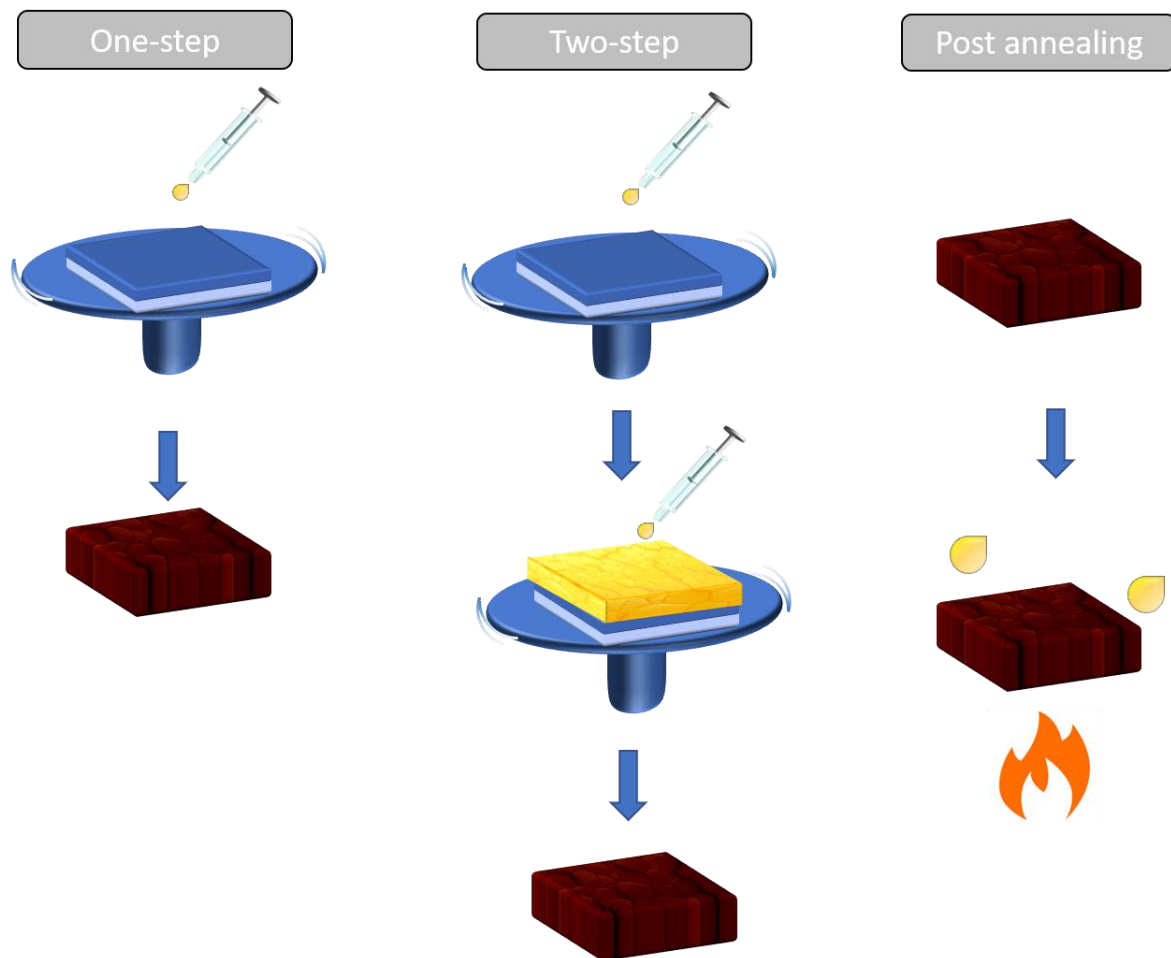


Figure 2. 4. Various perovskite deposition method

One step method: In one-step methods, the perovskite precursor solution consisting of metal halide and organohalide in proper solvent is deposited onto the substrate directly. Since the ionic interaction in the crystallization process is quite complicated, the morphology control for the perovskite film based on “one step” method is always a challenge. The final film often shows shiny-gray appearance, indicating a rough surface with lots of pinholes and the poor film quality. Several approaches have been

proposed to overcome the challenge of morphology control in the “one step” method.

Retarding the crystal growth has been proved to be effective to optimize the perovskite quality. By slowing down the crystal growth rate, the perovskite film morphology can be well controlled with higher film coverage and fewer pinholes, leading to the optimized film quality. Chlorine (Cl) additive can effectively retard the crystallization of MAPbI₃ by forming the intermediate species, PbCl₂. Ding et al. demonstrated that chloride based additives could help to improve the perovskite film surface uniformity and coverage in the inverted Perovskite solar cells. Similarly, using PbCl₂ as one of the perovskite precursors for “one step” method also gave a uniform perovskite film in the same way.

Solvent engineering is an approach to retard the crystallization, which involved the immediate phase during the film growing. For instance, dimethyl sulfoxide (DMSO) was used as both the solvent and the additive in the “one step” precursor solution. A complex immediate phase, MAI-PbI₂-DMSO, could form a compact and uniform film, which was the key point of this method. The extra DMSO gradually left the film during the followed thermal annealing, retarding the crystallization of the perovskite

Another example of accelerating the crystal growth was reported by Mohite et al. They have proposed the solution based hot-casting technique. The hot precursor solution was dropped onto a substrate maintained at 180°C and spin-coated. Driven by the high temperature of the substrate, the solvent evaporation was accelerated and the crystal growth could be finished during spinning.

Two-step method: Two step methods offer the possibility of controlling the growth of two precursor materials separately. It's easier to control the growth of a single precursor material than the mixture of two or more materials. The two step methods have been intensively studied in the regular Pero-SCs. In the traditional sequential deposition method developed by Gratzel et al., PbI₂ is firstly deposited onto a mesoporous TiO₂ scaffold. Then the PbI₂ covered substrate is dipped into the MAI solution. MAI penetrates through the channels in the porous TiO₂ scaffold to react with PbI₂ and produce CH₃NH₃PbI₃ within seconds. However, in the inverted Pero-SCs, the devices generally consist of planar films without mesoporous scaffolds. On the planar substrate, PbI₂ tends to form a compact film due to the lack of the mesoporous scaffold. When dipped into the MAI solution, only the PbI₂ on the surface could contact and react with MAI, resulting in the residue of PbI₂ in the final perovskite film. Although the unreacted PbI₂ may have positive effect of reducing interfacial charge recombination in regular Pero-SCs, the residual PbI₂ in inverted Pero-SCs can only result in the reduced light harvesting and larger charge transport resistance. Therefore, the main challenge of using “two-step” method in inverted Pero-SCs is achieving the full conversion of PbI₂ to the perovskite.

As a modified “two-step” method, Huang et al. have developed the inter diffusion method to prepare perovskite for inverted Pero-SCs. Basically, MAI was spin-coated on the top of PbI₂ layer to form stacked films. Driven by the thermal annealing, PbI₂ and MAI diffused into and reacted with each other to produce MAPbI₃. Full conversion of the two precursor materials could be achieved by controlling

the film thicknesses precisely. During the same period, Wu et al. developed a (2/1)-step spin-coating method which was similar to the inter diffusion method. Both the methods gave rise to high-quality perovskite films and high performance devices.

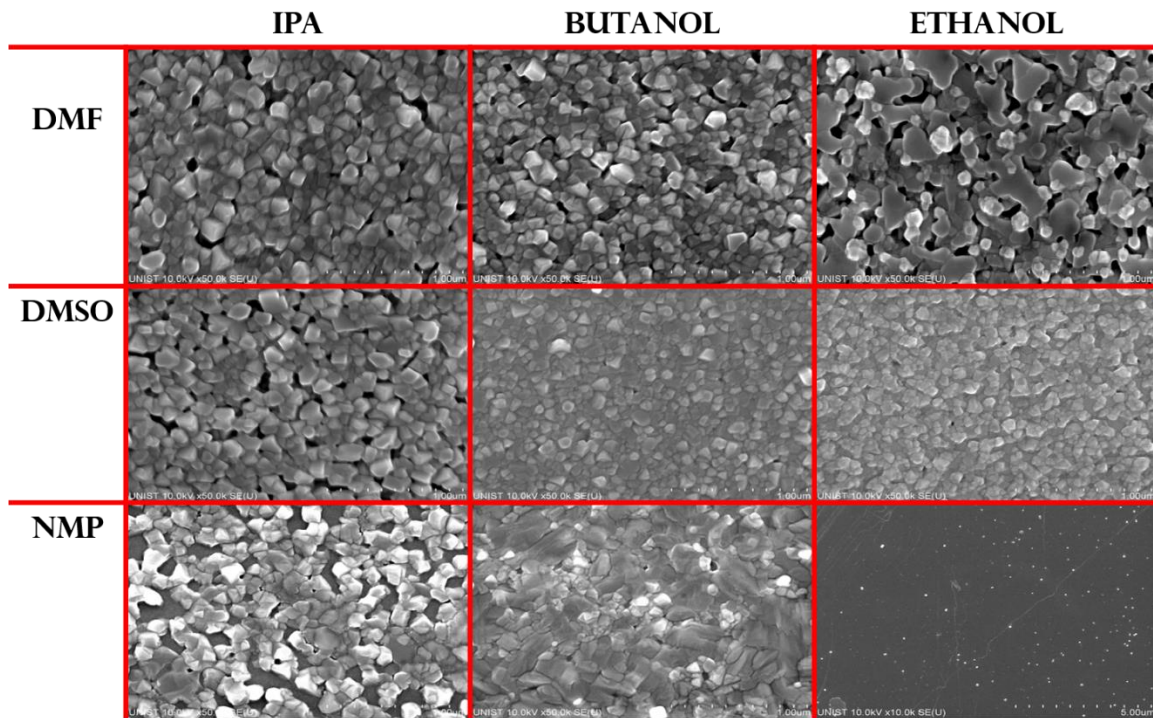


Figure 2. 5. Morphology of perovskite films with various solvent

Post annealing method: In most cases, post annealing process is necessary for the perovskite crystal growth. Annealing temperature and duration are the major parameters for the post annealing process and these parameters have been intensively studied and established in the regular Pero-SCs. In the development of inverted Pero-SCs, researchers also noted that the annealing atmosphere has great influence on the resultant perovskite film. Some researches were conducted to optimizing the film quality by controlling the annealing atmosphere.

Huang et al. proposed the solvent annealing, where DMF vapor was introduced into the thermal annealing atmosphere. Since both PbI_2 and MAI have high solubility in DMF, DMF vapor provided a wet environment so that the precursor ions and molecules could diffuse a longer distance than in the all-solidstate thermal annealing, yielding larger grain sizes. The average grain size of the solvent-annealed film was always slightly larger or comparable to the film thickness. This means that photogenerated charges could transport to the charge selective layers through a single grain without the charge recombination at the grain boundaries. In addition to the application in the interdiffusion method, the solvent environment is also helpful in other deposition methods. For example, in the vapor atmosphere of DMF/CB mixture, the as-casted $MAPbI_{3-x}Cl_x$ based on “one-step” coating method could

achieve good crystallization at room temperature without further treatment.

Environment humidity was also found to affect the film quality. It was noted that annealing the perovskite film in a humid environment dramatically increased the grain size, carrier mobility and carrier life time. This might be ascribed to the hygroscopic nature of MAI. Due to the hygroscopic nature of MAI, moisture in the environment accumulated at the grain boundaries, inducing grain boundary creep and subsequently merging adjacent grains together. In addition, moisture provided an aqueous environment similar to the DMF vapor atmosphere, where precursor ions and molecules diffuse a longer distance, further promoting the grain growth. Despite the exact mechanism has not been established, lots of researches have confirmed the positive effect of moisture or water molecules on the film quality.

2.4 Figures of merit of thin film solar cells

The enormous amount of solar energy is reached on earth's surface in every second continuously. When the sunlight passes through the atmosphere, a part of solar spectrum is absorbed by water vapor, ozone and scattered by dusts and aerosols in air. The standard solar spectrum, as defined under specific atmosphere conditions, is referred to Air Mass or simply AM. Generally, the AM is numbered by considering the zenith angle of light incidence on the ground. e.g. light incident at 45° above the ground corresponds to 1.5, which is the value of $\sec 45^\circ$. For universal characterization of the solar cells fabricated anywhere in the world, the standard airmass, AM1.5G, is widely applied to the solar simulator. Total power density of AM 1.5G solar spectrum is $\sim 1000 \text{ W/m}^2$. Left image of **Figure 2.6** compares the irradiance of AM 1.5G with AM 0 corresponding to solar power spectrum outside the earth atmosphere. Huge attenuation at $\sim 750 \text{ nm}$ in the AM 1.5G spectrum is due to O_2 absorption and several holes after 900 nm are mainly attributed to the absorption by H_2O molecules. Photon energy is plotted, not in terms of irradiance, but in terms of photon flux. The photon flux density of AM 1.5G can be calculated by dividing solar irradiance by the photon energy at each wavelength and is shown in the right image of **Figure 2.6**.

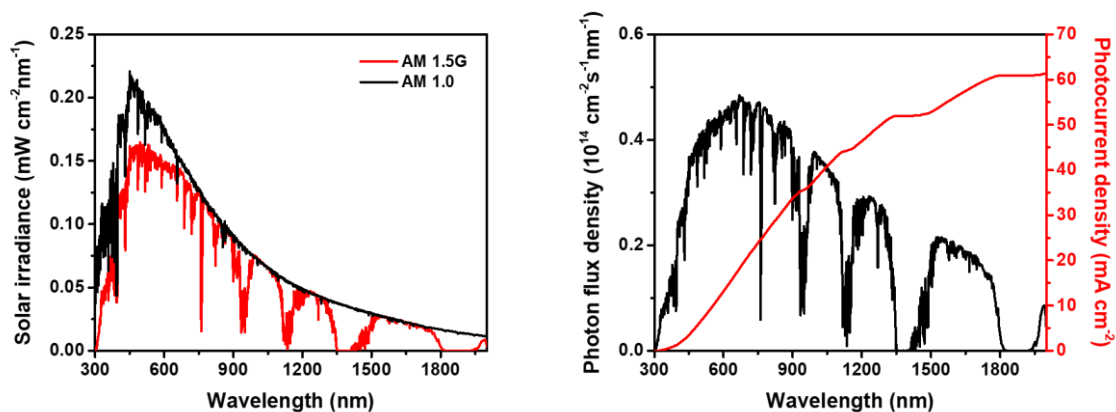


Figure 2. 6. Solar irradiance of AM1.5G and AM 1.0. Photon flux density of AM 1.5G and maximum photocurrent density of the device absorbing light up to corresponding wavelength are shown in the right of the figure.

Optical bandgap, E_g of the photoactive layer determines the absorption range of incident light to the solar cell. The longest wavelength the active layer can deal with can be calculated by using simple relation between photon energy and wavelength.

$$E_g = \frac{hc}{\lambda_{max}} \quad (\text{Eq. 2-2})$$

Then we can calculate the maximum photocurrent density of the ideal solar cell that absorbs all the photons with the wavelengths in E_g :

$$J_{ph} = q \int_0^{\lambda_{max}} \frac{d\phi}{d\lambda} d\lambda \quad (\text{Eq. 2-3})$$

where $d\phi/d\lambda$ is the photon flux density. The calculated photocurrent density is shown as red curve in the right image of **Figure 2. 6**.

J - V characteristics of the solar cell can be expressed using the modified diode equation:

$$J = J_s \left[\exp\left(\frac{q(V-JR_sA)}{nkT}\right) - 1 \right] + \frac{V-JR_sA}{R_{sh}A} - J_{ph} \quad (\text{Eq. 2-4})$$

where J_s is the saturation current of the diode, n is the ideality factor, k is the Boltzmann constant, A is the device area, R_s is series resistance, and R_{sh} is shunt resistance. Its equivalent electric circuit is shown in **Figure 2.7**. Two resistors in the circuit causes parasitic loss during the operation of the device.

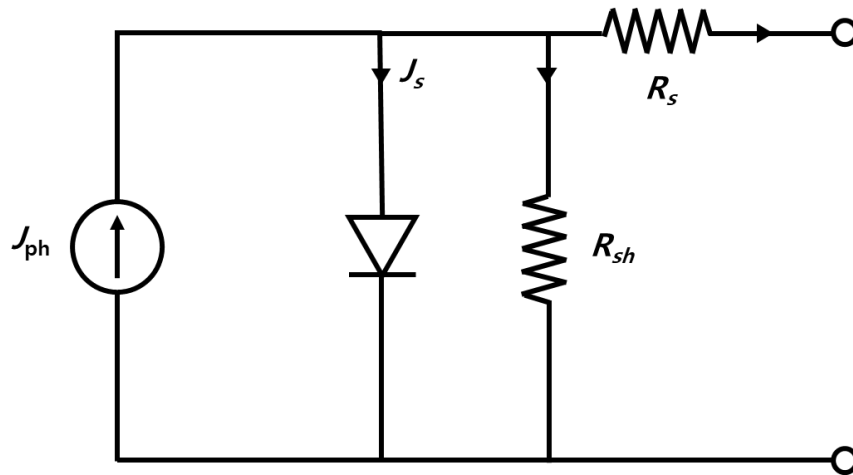


Figure 2. 7. Equivalent circuit of a solar cell

An ideal solar cell has n close to 1, 0 of R_s , and infinite R_{sh} . These conditions reduce Eq. (2-4) to be:

$$J = J_s \left[\exp\left(\frac{qV}{kT}\right) - 1 \right] - J_{ph} \quad (\text{Eq. 2-5})$$

which is a typical diode equation with an additional term, $-J_{ph}$. Ideal J_s exhibits exponential dependence on E_g : $J_s \sim \exp(-E_g)$. Short-circuit current density, J_{SC} ($V = 0$) is equal to J_{ph} in the ideal case and open circuit voltage, V_{OC} is obtained by putting $J = 0$ to Eq. (2-5).

$$V_{OC} = \frac{kT}{q} \ln\left(\frac{J_{ph}}{J_s} + 1\right) \quad (\text{Eq. 2-6})$$

Short-circuit current occurs when the solar cell's anode and cathode terminals are directly connected in a short circuit and the resulting current is termed the short-circuit current. Open-circuit voltage occurs when the solar cell's electrodes are isolated from each other and the resulting voltage is termed the open-circuit voltage.

Output power density of the device can be calculated by multiplying V to Eq. (2-5).

$$P_{\text{out}} = JV = J_s V \left[\exp\left(\frac{qV}{kT}\right) - 1 \right] - J_{ph} V \quad (\text{Eq. 2-7})$$

Maximum output power density, P_m is achieved when $dP_{\text{out}}/dV = 0$:

$$\frac{dP_{\text{out}}}{dV} = \frac{d(JV)}{dV} = \frac{dJ}{dV} V + J = 0 \quad (\text{Eq. 2-8})$$

Substituting Eq. (2-5) for J of dJ/dV in Eq. (2-8) gives the current density at maximum power point (mpp), J_m :

$$J_m = -J_s \beta V_m \exp(\beta V_m) \quad (\text{Eq. 2-9})$$

where β is kT/q . The voltage at mpp, V_m can be obtained by substituting Eq. (2-9) for J in Eq. (2-5):

$$\begin{aligned} -J_s \beta V_m \exp(\beta V_m) &= J_s \left[\exp\left(\frac{qV_m}{kT}\right) - 1 \right] - J_{ph} \\ V_m &= \frac{1}{\beta} \ln \left[\frac{(J_{ph}/J_s) + 1}{1 + \beta V_m} \right] = V_{\text{OC}} - \frac{1}{\beta} \ln(1 + \beta V_m) \end{aligned} \quad (\text{Eq. 2-10})$$

The power conversion efficiency (PCE) is the ratio of P_m to the incident power density, P_{in} .

$$\eta = \frac{|P_m|}{P_{in}} = \frac{|J_m V_m|}{P_{in}} = \frac{J_s \beta V_m^2 \exp(\beta V_m)}{P_{in}} \quad (\text{Eq. 2-11})$$

(-) sign of P_m from J_m was removed in Eq. (2-11) because the sign indicates the power is generated from the device. Positive sign of P_{in} in denominator means that the power is absorbed by the device. For the efficiency calculation, the sign of each power is physically meaningless.

J - V characteristics of solar cell under illumination is shown in **Figure 2. 8**.

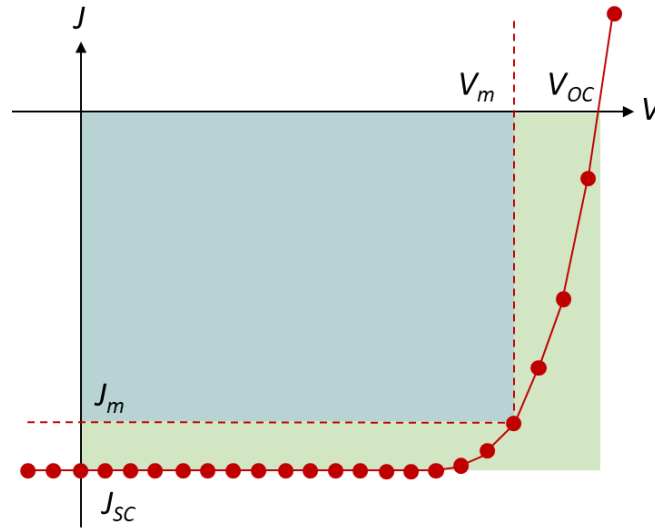


Figure 2. 8. J - V characteristics of solar cell under illumination.

Fill Factor(FF) is defined as a value which relates the total amount of power that a solar cell is able to theoretically produce to the maximum power that the device can produce when it is actually tested. FF is a geometrical parameter measuring the degree of areal occupation of blue square ($V_m \times J_m$) in green square ($V_{oc} \times J_{sc}$). Efficient solar cells have a FF close to 1 but it is not able to reach to 100% even in ideal solar cell because of the exponential dependence of J - V characteristics. PCE, then can be expressed using V_{oc} , J_{sc} , and FF :

$$\eta = \frac{|P_m|}{P_{in}} = \frac{|V_m I_m|}{P_{in}} = \frac{V_{oc} J_{sc} FF}{P_{in}} \quad (\text{Eq. 2-12})$$

Eq. (2-12) addresses the consideration on theoretical maximum efficiency of solar cell. V_{oc} decreases with smaller E_g because of increased J_s , but J_{sc} increases as we discussed in **Figure 2. 6** and Eq. (2-2, 3). Because of this trade-off, it is known that theoretical maximum efficiency of 30.6% can be achieved at 1.32 eV of E_g . The values can exhibit some discrepancy depending on the studies. The theoretical efficiency limit is called Schokley-Queisser limit.

In non-ideal solar cell, FF is hugely affected by two parasitic resistances, R_s and R_{sh} :

$$FF(R_s, R_{sh}) = FF(0, \infty) \left[\left(1 - \frac{J_{sc} R_s}{V_{oc}} \right) - \left(\frac{V_{oc}}{J_{sc} R_{sh}} \right) \right] \quad (\text{Eq. 2-13})$$

Another useful figure of merit for solar cell characterization is quantum efficiency. The simplest quantum efficiency of solar cell is photon to electron conversion efficiency. It is called the external quantum efficiency (EQE) or incident photon to electron conversion efficiency (IPCE). An example of EQE spectrum is shown in **Figure 2. 9**.

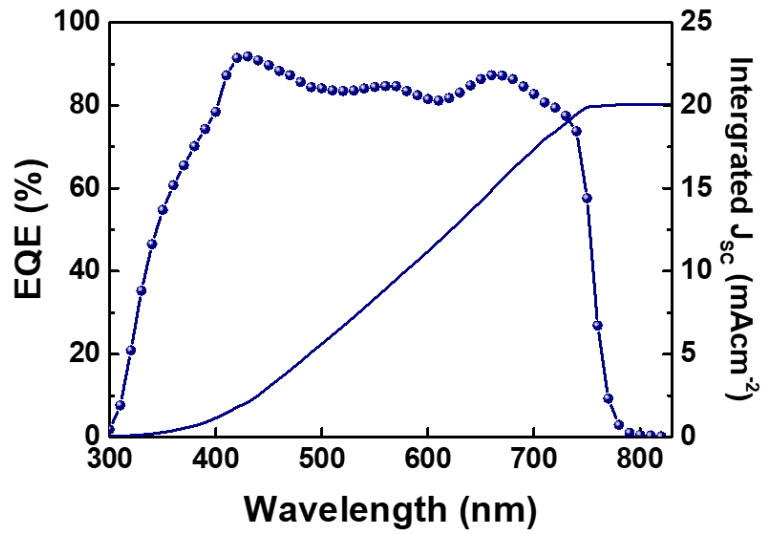


Figure 2. 9. An example of external quantum efficiency and integrated J_{SC} of solar cell.

J_{SC} of the device can be estimated from EQE spectrum using the following equation:

$$J_{SC} = \frac{e\lambda}{hc} \int EQE(\lambda)F(\lambda)d\lambda \quad (\text{Eq. 2-14})$$

where $F(\lambda)$ is solar irradiance. As J_{SC} measured in J - V characteristics is significantly altered by the small deviation of the distance between light source (solar simulator) and the device, EQE is useful to cross-check the measured J_{SC} . It should be noticed, however, that the estimated J_{SC} from EQE is only valid when the device exhibits linear dependence of J_{SC} on light intensity.

Internal quantum efficiency, IQE is the ratio of the number of absorbed photons by active layer to the number of incident photons. Because IQE excludes photons absorbed by the other layers in solar cell, it can be useful when you want to demonstrate the quality of the device; how efficiently photoexcited electrons are extracted out of the device. Despite its usefulness, however, the practical difficulty of measuring light absorption by active layer makes researchers hard to estimate the exact IQE of the device.

CHAPTER 3. Mixed solvents for the Optimization of Morphology in Solution-processed, Inverted-Type Perovskite/Fullerene Hybrid Solar Cells

The content of this chapter is published in *Nanoscale* **6**, 6679 (2014)

3.1 Research background

Hybrid solar cells (HSCs) using organometal halide perovskites as light absorbers have received much attention recently due to their advantages including broad light absorption from visible to the near-infrared region, high extinction coefficients, long charge-carrier diffusion lengths and bandgaps which can easily be tuned via compositional changes.^{3, 4, 6, 18-24} Significant efforts have been expended to investigate new perovskite materials such as methyl ammonium lead halides, (CH₃NH₃PbX₃) and cesium tin iodide, (CsSnI₃),^{3, 25-29} to explore new architectures such as meso-structured metal oxide layers (titanium dioxide, TiO₂ and aluminum oxide, Al₂O₃),^{3, 30-32} to investigate novel deposition methods such as sequential and vapor deposition, and explore polymeric hole conductors such as poly-3-hexylthiophene, P3HT and poly-triarylamines, PTAA, etc.^{20, 33} These efforts have led to dramatically improved power conversion efficiencies (PCE) in n-i-p perovskite solar cells (PeSCs) of up to 15%. In conventional PeSCs, mesoporous TiO₂ and Al₂O₃ play an important role as the electron accepting/transport or scaffold layer, respectively. In addition, 2,2',7,7'-tetrakis-(N,N-di-*p*-methoxyphenylamine)-9,9'-spirobifluorenespiro (spiro-OMeTAD) or semiconducting polymers deposited on top of perovskite layers play a critical role as hole transport layers (HTL). Liu *et al.* reported a PCE of 15.4% without a meso-structured TiO₂ layer by developing a vapor-deposition route to obtain high-quality CH₃NH₃PbI_{3-x}Cl_x perovskite films as light absorbing layers.¹⁹ In spite of high device efficiencies obtained with these n-i-p structure PeSCs, high temperatures of over 500 °C are required for calcination of the compact TiO₂ layer.^{19, 30} Since thermal treatment at such high temperatures is not suitable for flexible substrates, new device architectures are urgently needed. Jeng *et al.* has reported inverted-type perovskite/fullerene planar heterojunction PeSCs by depositing various fullerene derivatives, such as fullerene (C₆₀), [6,6]-phenyl-C₆₀ butyric acid methyl ester (PCBM) and indene-C₆₀-bisadduct (ICBA), on top of methyl ammonium lead iodide (CH₃NH₃PbI₃) perovskite layers via thermal evaporation.³⁴ Although new p-i-n structures have been introduced for PeSCs, there remain significant problems in terms of low device efficiency and the need for high-vacuum processing to deposit the fullerene derivatives as electron acceptors. Recently, Lam and Snaith groups have developed

highly efficient p-i-n structure PeSCs by depositing perovskite ($\text{CH}_3\text{NH}_3\text{PbI}_3$ or $\text{CH}_3\text{NH}_3\text{PbI}_{3-x}\text{Cl}_x$) and PCBM films via low-temperature and solution-processing.^{35,36} However, there is still considerable room for further enhancement in device efficiency through careful optimization of perovskite film morphologies and device architectures.

Here, we demonstrate high performance $\text{CH}_3\text{NH}_3\text{PbI}_3/\text{PCBM}$ p-i-n structure PeSCs by optimizing the morphology of perovskite films using solvent mixtures in which all layers are deposited via solution processing at low temperature. In the inverted structure, we employ a simple device configuration of indium tin oxide (ITO)/poly(3,4-ethylenedioxythiophene):polystyrene sulfonic acid (PEDOT:PSS)/ $\text{CH}_3\text{NH}_3\text{PbI}_3$ perovskite/PCBM/aluminum (Al). Improved morphology is observed in the perovskite film deposited from mixed solvents, leading to improved exciton dissociation efficiency and reduced recombination losses at the interface between perovskite and PCBM and improvements in device efficiency to over 6%.

3.2 Experimental details

Materials and Preparation of Perovskite

lead iodide (PbI₂), anhydrous *N,N*-dimethylformamide (DMF), and γ -butyrolactone (GBL) were purchased from Sigma-Aldrich and used without further purification. Methyl ammonium iodide (CH₃NH₃I) and the precursor solution of ammonium lead iodide (CH₃NH₃PbI₃) were prepared as previously reported.³⁴ An equimolar ratio of CH₃NH₃I and PbI₂ were dissolved in GBL with a concentration of 20 wt.% and dissolved in DMF and the DMF:GBL mixed solve (97:3 [vol.%]) with a concentration of 12 wt.%. These solutions were stirred at 60 °C for 12 h inside a glovebox filled with nitrogen gas.

Device fabrication

Poly(3,4-ethylenedioxythiophene):polystyrene sulfonic acid (PEDOT:PSS) was spin-cast at 5000 rpm on cleaned ITO after UV-ozone treatment for 20 min and dried at 140 °C for 10 min. On top of PEDOT:PSS layer, three types of CH₃NH₃PbI₃ perovskite precursor solution (12 wt.%) were spin-cast at 8000 rpm for 60 s and dried on hot-plate at 100 °C for 15 min. The PCBM solution (0.7 wt.% in chloroform) was spin-cast at 3000 rpm on top of the perovskite layer. Subsequently, Al (100 nm) electrodes were deposited on the PCBM layer under vacuum (<10⁻⁶ Torr) by thermal evaporation.

Measurement

The current density-voltage (*J-V*) characteristics of PSCs were measured using a Keithley 2635A Source Measure Unit. Solar cell performance was characterized under illumination by an Air Mass 1.5 Global (AM 1.5 G) solar simulator with an irradiation intensity of 100 mW cm⁻². External quantum efficiency (EQE) measurements were obtained under ambient conditions using a PV measurements QE system, with monochromatic light from a xenon lamp. The monochromatic light intensity was calibrated with a Si photodiode and chopped at 100 Hz. Masks (13.0 mm²) made of thin metal were attached to each cell before measurement for *J-V* characteristics and EQE.

3.3 Results and discussion

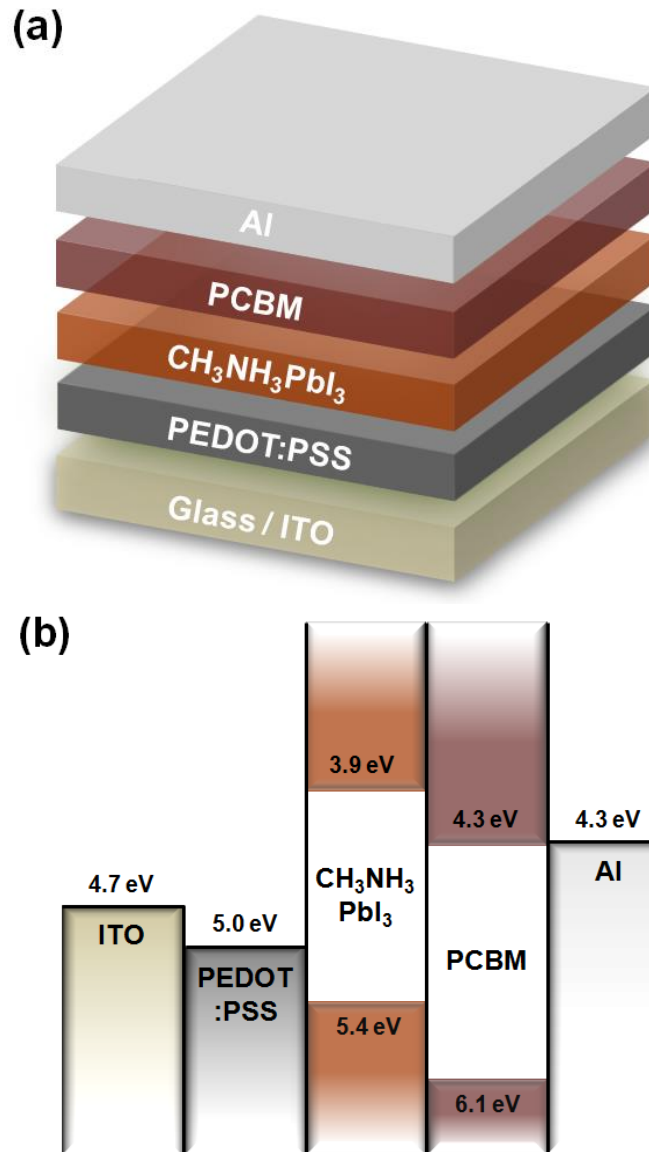


Figure 3. 1. (a) Device structure. (b) Energy band diagram of p-i-n structure PeSCs.

To form CH₃NH₃PbI₃ perovskite layers with interconnected crystalline structure and appropriate film morphology on top of PEDOT:PSS layer, we used γ -butyrolactone (GBL), N,N-dimethylformamide (DMF) and mixtures of GBL and DMF as processing solvents for precursors comprised of equimolar amounts of CH₃NH₃I and PbI₂.

Figure 3.1a and 1b show the device structure and energy band diagram of p-i-n structure PeSCs, respectively. Contrary to conventional PeSCs which rely on n-type electron transport layers as substrates, we employed a PEDOT:PSS layer, which is extensively used as a hole transport material in polymer solar cells,³⁷⁻³⁹ spin-coated on top of glass/ITO anodes (**Figure 3.1a**) as the substrate. The active layer of p-i-n structure PeSCs is a heterojunction consisting of CH₃NH₃PbI₃ (electron donor) and

PCBM (electron acceptor). Most exciton generation occurs in $\text{CH}_3\text{NH}_3\text{PbI}_3$ perovskite layer via absorption of light and these excitons are effectively dissociated at the electron donor/acceptor interface because of the long-range charge-carrier diffusion length (~ 100 nm) and low exciton binding energy (37-50 meV) inherent to $\text{CH}_3\text{NH}_3\text{PbI}_3$ perovskite.^{4, 21, 40} The highest occupied molecular orbital (HOMO) (5.4 eV) and lowest unoccupied molecular orbital (LUMO) (3.9 eV) levels of $\text{CH}_3\text{NH}_3\text{PbI}_3$ perovskite are well-matched with those of PCBM (HOMO: 6.1 eV, LUMO: 4.3 eV), leading to a cascading energy alignment for efficient exciton dissociation and charge extraction (**Figure 3.1b**). Specifically, photo-dissociated electrons can transfer to the LUMO band of PCBM within 0.40 ns and be collected at the Al cathode, while dissociated holes can transfer to the PEDOT:PSS in less than a nanosecond to be collected at ITO anode.²¹

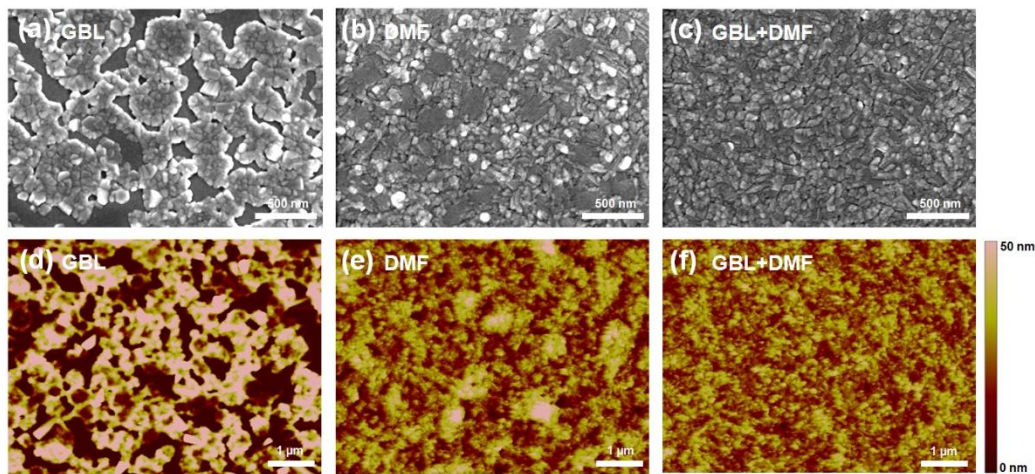


Figure 3. 2. (a-c) SEM top-view. (d-f) AFM topography images of $\text{CH}_3\text{NH}_3\text{PbI}_3$ perovskite films from different solvents.

One of the key factors in the design of highly efficient PeSCs is complete coverage and uniformity of perovskite films on substrates. Solution-processed perovskite films tend to have voids between crystals, which are detrimental to device performance.^{19, 34} We collected scanning electron microscopy (SEM) and atomic force microscopy (AFM) images to investigate the coverage and morphology of perovskite films prepared from different solvents. The $\text{CH}_3\text{NH}_3\text{PbI}_3$ perovskite films were prepared by spin-coating a perovskite precursor solution on top of PEDOT:PSS-coated ITO substrates and drying at 100 °C for 15 min. **Figure 3.2a-c** present SEM top-view images of perovskite films prepared from different solvents. All films exhibited unique crystalline features of perovskite with length scales on the order of several hundred nanometers.^{18, 19, 34} In the film prepared from GBL, there were large voids between crystal boundaries, indicating that the perovskite film did not completely cover the PEDOT:PSS layer (**Figure 3.2a**). Although the film from DMF had relatively smaller voids and almost completely covered the PEDOT:PSS layer, there were uneven crystal domains with small (~ 100 nm) and large (200-300 nm) grain sizes (**Figure 3.2b**). To optimize the crystalline structure and improve the

morphology of perovskite films, we used a solvent mixture of GBL and DMF (DMF:GBL = 97:3 [vol%]) to make the perovskite precursor solution. In contrast, the film from the solvent mixture had uniform crystal domains with smaller grain sizes (~100 nm) (**Figure 3. 2c**). These results are consistent with AFM topography images. As shown in **Figure 3.2d-f**, the film from GBL exhibited large domains with the highest root-mean-square (RMS) roughness of 24.53 nm among three films (**Figure 3. 2d**). The film from DMF had a reduced RMS roughness of 8.88 nm and a great number of large clusters (**Figure 3. 2e**), whereas the film from the solvent mixture of DMF and GBL had the lowest RMS roughness of 6.60 nm with small and uniform crystal domains (**Figure 3. 2f**). Uniform and smooth perovskite films with interconnected crystalline networks were obtained from the mixed solvent system, allowing enhanced interfacial contact and reduced voids between perovskite and PCBM. Additional AFM topography images were collected for films after a PCBM layer had been coated on top of the perovskite films (**Figure 3.3**). The surface roughness of the films after PCBM coating atop the perovskite layers became much smoother (GBL: 8.36 nm, DMF: 1.95 nm, mixed solvent: 2.07 nm). However, the perovskite film from GBL still exhibited a fairly high surface roughness even after PCBM coating, which may lead to a rough contact between PCBM and the Al electrode and adversely affect the performance of the device.

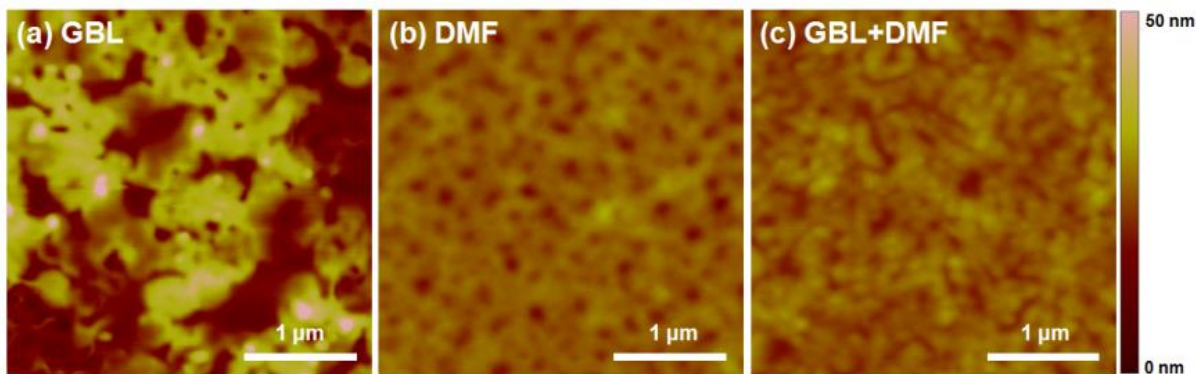


Figure 3. 3. (a) UV-vis absorption spectra. (b) XRD patterns of CH₃NH₃PbI₃ perovskite films from different solvents.

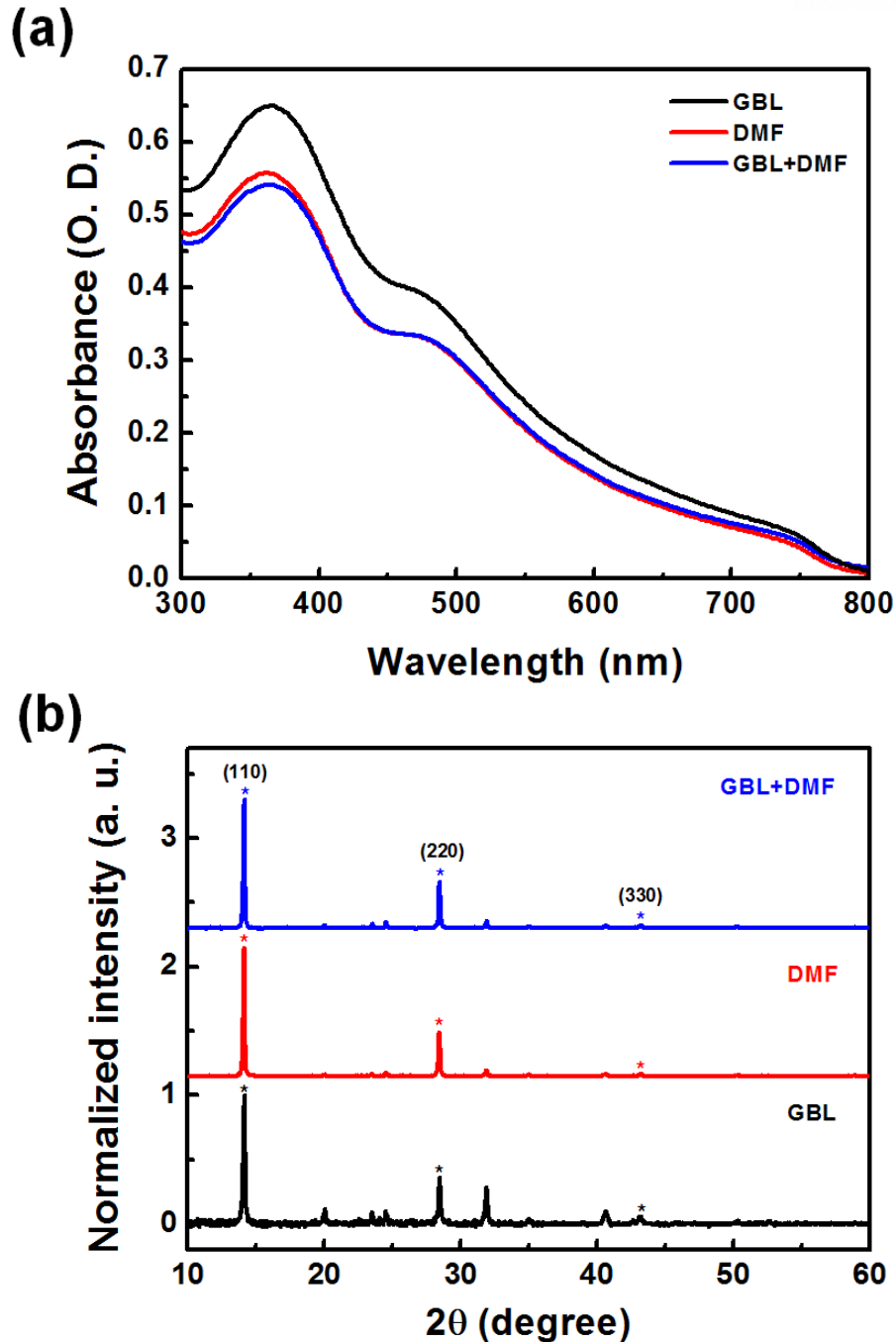


Figure 3. 4. (a) UV-vis absorption spectra. (b) XRD patterns of CH₃NH₃PbI₃ perovskite films from different solvents.

To investigate the effect of mixed solvents on the light absorption and crystal structure of the perovskite films, we measured UV-vis absorption and X-ray diffraction (XRD) of CH₃NH₃PbI₃ perovskite films prepared from different solvents. The same, optimized film processing conditions used for devices were used to prepare the UV-vis samples, resulting in films with a thickness of 30 – 40 nm (GBL: 37 nm, DMF: 32 nm, mixed: 30 nm). As shown in **Figure 3. 4a**, all films showed absorption onsets at 800 nm with broad absorption ranging from visible to near-IR region. The film from GBL had

higher optical density than other films due to being slightly thicker than the other samples. The X-ray diffractograms of perovskite films on PEDOT:PSS-coated glass substrates (**Figure 3. 4b**) all exhibited diffraction peaks from the tetragonal perovskite phase with diffraction peaks at 14.13°, 28.43° and 43.20°, assigned to the (110), (220), and (330) planes, respectively. There were no differences in position of XRD peaks of the three films. The higher intensity in film from GBL may be attributed to a slightly thicker film, or more complete crystallization, compared to the films from DMF and mixed solvents. The negligible differences in UV-vis absorption and XRD measurements for films prepared from different solvents imply that the mixed solvent system only influences film coverage and morphology without causing significant changes to the optical properties or crystalline structure of the material.

To investigate the effect of different solvents on device performance, we fabricated p-i-n structure PeSCs using $\text{CH}_3\text{NH}_3\text{PbI}_3$ processed with different ratios of DMF to GBL. We found that the devices prepared from DMF:GBL mixtures resulted in the best solar cell performance, as shown by the current density-voltage (J-V) characteristics and external quantum efficiency (EQE) as displayed in **Figures 3. 5a and 3. 5b**, respectively. Devices with a perovskite layer prepared from GBL exhibited a short-circuit current density (J_{SC}) of 7.19 mAcm^{-2} , open-circuit voltage (V_{OC}) of 0.95 V, fill factor (FF) of 0.60, and power conversion efficiency (PCE) of 4.14%. The devices from DMF showed a J_{SC} of 7.35 mAcm^{-2} , V_{OC} of 0.93 V, FF of 0.73 and PCE of 5.02%. These devices, in which the PCBM layer was deposited by spin-coating, had higher efficiencies than previously reported devices with PCBM deposited by thermal evaporation. To find the optimum mixed solvent ratio, we fabricated devices with controlled DMF:GBL ratios. We found a DMF:GBL volume ratio of 97:3 to be the best condition for perovskite film processing (**Figure 3. 6 and Table 3. 2**). The optimized mixed solvent resulted in remarkable enhancement in J_{SC} (8.74 mA cm^{-2}) and FF (0.76) (**Figure 3. 7**). The resulting PCE of 6.16%, represents a ~49% and ~23% PCE enhancement compared to those of the devices prepared from GBL and DMF, respectively. Since the V_{OC} value of heterojunction solar cells is determined by energy difference between the HOMO level of electron donor and the LUMO level of electron acceptor, V_{OC} values of the devices were similar while some devices with different ratios of mixed solvents show up to 1.05V (**Table 3. 2**). Detailed device characteristics are summarized in **Table 3. 1**. The improvement in J_{SC} is in good agreement with EQE measurements, which have an error range of ~2% (**Figure 3. 5b**). All devices exhibited broad EQE curves throughout the visible spectrum to the near IR wavelength region (300-800 nm), consistent with the UV-vis absorption spectra. The device from GBL exhibited an EQE below 40%, whereas the device from DMF reached a maximum EQE of 46.5% at 470 nm. Mixed solvents led to high EQE over 50% ranging from 400 nm to 500 nm. Partially high EQE of the device from GBL in the range of 650-800 nm may be attributed to increased light absorption due to greater film thickness and large perovskite crystal domains.

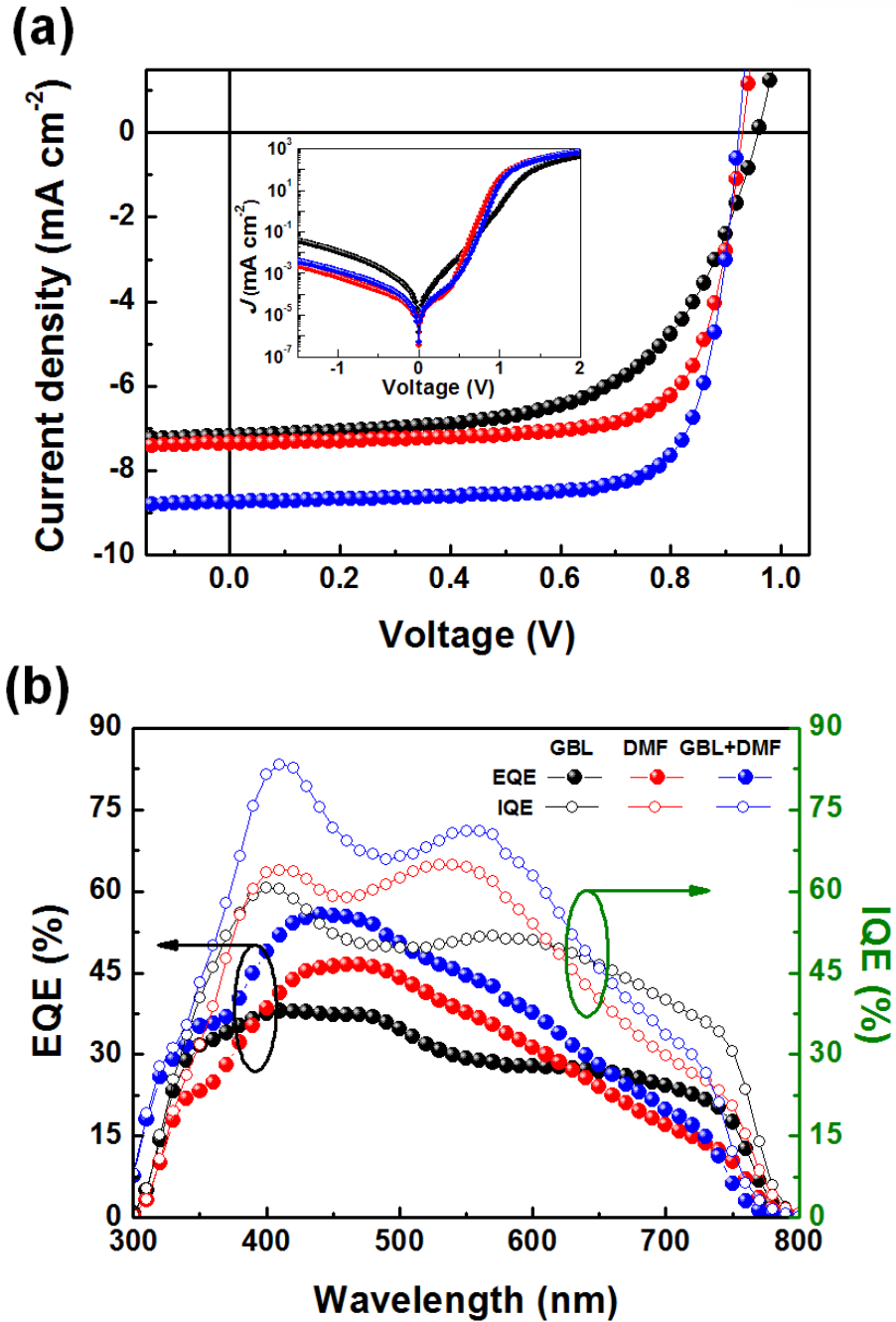


Figure 3. 5. (a) J-V characteristics (b) EQE and IQE of p-i-n structure PeSCs prepared from different solvents.

Table 3. 1. Characteristics of p-i-n structure PeSCs prepared from different solvents.

Solvent	J_{sc} (mA cm^{-2})	V_{oc} (V)	FF	PCE (%)	$Cal. J_{sc}$ [mA cm^{-2}]
GBL	7.19	0.95	0.60	4.14	7.21
DMF	7.35	0.93	0.73	5.02	7.55
GBL+DMF	8.74	0.92	0.76	6.16	8.84

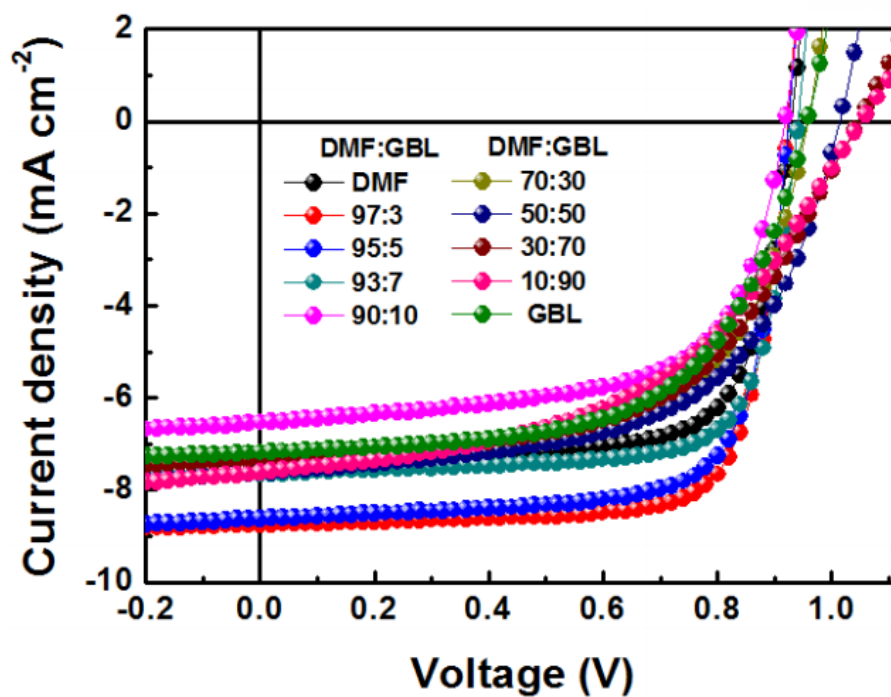


Figure 3. 6. J-V curves of p-i-n structure PeSCs prepared from different solvents with various DMF:GBL ratio.

Table 3. 2. Characteristics of p-i-n structure PeSCs prepared from different solvents with various DMF:GBL ratio.

Solvent	J_{sc} (mA cm^{-2})	V_{oc} (V)	FF	PCE (%)
Only DMF	7.35	0.93	0.73	5.02
97:3	8.74	0.92	0.76	6.16
95:5	8.62	0.93	0.73	5.86
93:7	7.64	0.94	0.75	5.37
90:10	6.53	0.92	0.64	3.83
70:30	7.29	0.96	0.62	4.31
50:50	7.62	1.01	0.59	4.52
30:70	7.31	1.05	0.55	4.23
10:90	7.62	1.05	0.49	3.93
Only GBL	7.19	0.95	0.60	4.14

^a Volume ratio of DMF and GBL

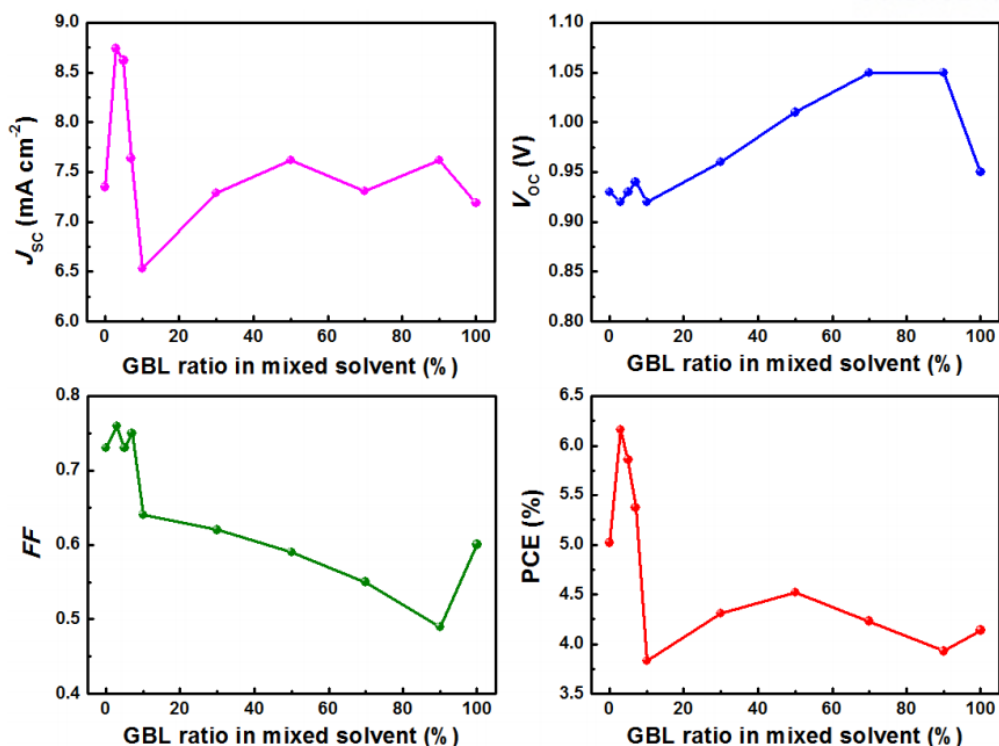


Figure 3. 7. Dependence of photovoltaic parameters (J_{sc} , V_{oc} , FF, and PCE) on the amount of GBL in mixed solvent of DMF and GBL.

We calculated the internal quantum efficiency (IQE) of the devices from the EQE and measured reflectance (**Figure 3.5b**). The IQE is the ratio of the number of electrons collected at the cathode to the number of absorbed photons, which provides information regarding recombination losses which occur during exciton diffusion, exciton dissociation, and charge transport. The device from the mixed solvent system exhibited a higher IQE over the whole spectrum with a maximum IQE of 83.4% at 410 nm, compared to those of the devices from GBL and DMF (GBL: 60.7% at 400 nm and DMF: 64.8% at 540 nm). High IQE over 80% implies that absorbed photons are efficiently converted to dissociated pairs of charge-carriers and those photogenerated carriers are collected at the electrodes with few losses, which can offer the possibility for further enhancing the device efficiency by increasing the thickness of perovskite/PCBM layer.

The inset of **Figure 3. 5a** shows dark J - V characteristics of the devices from different solvents. The devices from DMF and mixed solvents show lower leakage currents and better diode characteristics with rectification ratios over 10^5 compared to the device from GBL ($\sim 10^4$), consistent with the high FF observed in the devices from DMF (0.73) and mixed solvents (0.76). Because the optical density and film thickness do not change significantly with each solvent used, enhancements in J_{sc} and FF with solvents appear to originate from improved morphology, supported by the uniform crystal domains and minimized voids between perovskite crystals observed in films prepared from mixed solvents.^{24, 34, 41} The improved morphology of perovskite films using mixed solvents results in a remarkable PCE

enhancement by improving exciton dissociation efficiency and reducing recombination loss at the interface between the perovskite and PCBM layers.

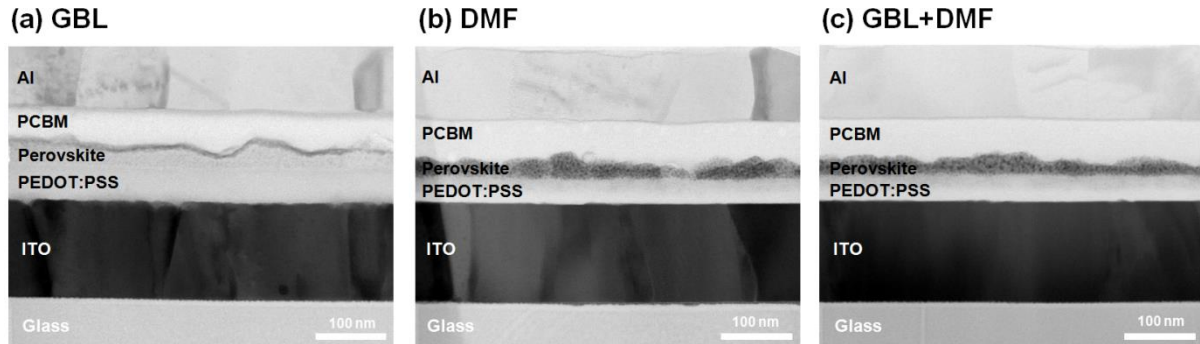


Figure 3. 8. TEM cross-sectional images of p-i-n structure PeSCs prepared from a) GBL, b) DMF, and c) mixed solvent.

Figure 3. 8 shows high-resolution transmission electron microscopy (HR-TEM) cross-sectional images of the devices prepared from different solvents. Each layer can clearly be seen in the images. All perovskite films exhibited bumpy surfaces on the PEDOT:PSS layer, typical of solution-processed perovskite films.[4] The device from GBL exhibited the thickest perovskite film with a large variation in film thickness (37 ± 18 nm) (**Figure 3. 8a**), whereas the devices from DMF and mixed solvents exhibited relatively thin and flat perovskite films (DMF: 32 ± 13 nm and mixed solvent: 30 ± 11 nm) (**Figure 3. 8b and 3. 8c**). These results are consistent with AFM images and also confirm poor FF in the device from GBL along with dark J-V characteristics.

3.4 Conclusion

In conclusion, we have successfully fabricated high performance p-i-n structure PeSCs using a DMF:GBL solvent mixture to improve the surface coverage and morphology of the perovskite layer. The $\text{CH}_3\text{NH}_3\text{PbI}_3$ perovskite and PCBM films were completely and sequentially deposited on PEDOT:PSS-coated ITO substrate via low-temperature solution processing. Use of a mixture of DMF and GBL to process the perovskite precursor solution improves interfacial contacts and reduces the voids between perovskite and PCBM layer by producing smooth perovskite film and uniform crystal domains with small grain size. This ideal film morphology improves exciton dissociation efficiency and reduces recombination losses at the perovskite/PCBM interface, leading to remarkable enhancements in device efficiency. Furthermore, this is the first report to introduce a mixed solvent system for the optimization perovskite film morphology in high-performance inverted-type perovskite/fullerene planar heterojunction solar cells. Our strategy offers a simple and effective route to develop high-performance organic-inorganic hybrid solar cells on flexible substrates or via roll-to-roll mass production techniques.

CHAPTER 4. Cesium-Doped Methylammonium lead Iodide Perovskite Light Absorber for Hybrid Solar cells

The content of this chapter is published in *Nano Energy* 7, 80 (2014)

4.1 Research background

Organolead halide perovskites (ABX_3 where A is organic or inorganic cation, B is metal cation, and X is halogen anion) have been extensively investigated as light absorbers for high efficiency organic-inorganic hybrid solar cells (HSCs) over the last few years.^{3, 4, 6, 18, 19, 21, 25, 29} In particular, methylammonium lead halide perovskites ($MAPbX_3$) are regarded as particularly promising light absorbers due to their many advantages including optimal band gaps, high absorption coefficients, and long-range exciton diffusion lengths.^{3, 4, 21} These perovskites have led to solar cells with power conversion efficiencies (PCEs) up to 15% in conjunction with the development of new device architectures (meso-structure metal oxides),^{3, 20, 30} and deposition methods (such as sequential and vapor deposition).^{18, 19} Although a few attempts to synthesize new perovskites have been made by changing halide anions (X) in the $MAPbX_3$ structure, these materials have not led to improvements in device efficiency.^{22, 27, 42} Optical and electronic properties of organolead halide perovskites have been studied by replacing MA cation with other organic cations such as ethylammonium (EA) and formamidinium (FA).^{43, 14, 44, 45} However, there has been no investigation of the effects that changing organic cation with inorganic cation in the $MAPbX_3$ structure has on properties of perovskite light absorbers. Thus, there is still considerable opportunity to improve device performance by optimizing optical and electronic properties of perovskite materials through study of the components and composition ratio.

Conventional perovskite solar cells (PeSCs) have employed meso-structured n-type metal oxide layer and organic hole conductors.^{3, 20, 31, 33} However, these devices require high temperature calcination (typically over 500 °C) of the compact titanium oxide layer or thermal evaporation under high vacuum for deposition of the perovskite layer.^{30, 32} High temperature thermal treatment and vacuum processing pose challenges for flexible device applications and roll-to-roll mass production. Although functioning inverted structures have been successfully realized using perovskite/fullerene planar heterojunctions,³⁴⁻³⁶ their performance can be further enhanced by improving the morphology of the perovskite films and developing new device architectures. Therefore, we seek to investigate simple and effective device processing procedures along with novel perovskite light absorbers for efficient PeSCs. Here, we report the synthesis of cesium (Cs)-doped methylammonium lead iodide ($Cs_xMA_{1-x}PbI_3$) perovskites as light absorbers and develop high-performance inverted-type planar heterojunction PeSCs utilizing Cs_xMA_{1-x}

$x\text{PbI}_3$ as an electron donor and [6,6]-phenyl- C_{60} butyric acid methyl ester (PCBM) as an electron acceptor.

The cation (A) in ABX_3 perovskites commonly comprises alkylammonium or alkali metal cations (e.g. methylammonium, formamidinium, cesium, etc). The identity of the A cation strongly influences the band gap and electronic properties of perovskites through its influence on the crystal structure.^{28, 41} Since MAPbI_3 perovskite is a well-known light absorber with a low band gap of 1.5 eV and high extinction coefficient in PeSCs,^{3, 20, 26} we replace a fraction of the MA ions with Cs in order to optimize the optical and electrical properties of the material while maintaining the fundamental characteristics of MAPbI_3 (**Figure 4. 1a**). For the preparation of MAPbI_3 absorbing films, a precursor solution consisting of equimolar amounts of methylammonium iodide (MAI) and lead iodide (PbI_2) was first dissolved in a mixed solvent of dimethylformamide (DMF) and γ -butyrolactone (GBL) (DMF:GBL = 97:3 vol.%), and stirred at 60 °C for 24h in a nitrogen-filled glovebox. The $\text{Cs}_x\text{MA}_{1-x}\text{PbI}_3$ precursor solutions were prepared using same procedure with a fraction of the MAI being replaced by CsI.

4.2 Experimental details

Preparation and characterization of perovskite

Cesium iodide (CsI), lead iodide (PbI₂), anhydrous *N,N*-dimethylformamide (DMF), and γ -butyrolactone (GBL) were purchased from Sigma-Aldrich and used without further purification. [6,6]-phenyl-C₆₀ butyric acid methyl ester (PC₇₀BM) was purchased from Rieke Metal Incorporation. Methyl ammonium iodide (CH₃NH₃I) was synthesized using a previously reported method.³⁴ Precursor solutions of Cs_xMA_{1-x}PbI₃ were prepared by dissolving equimolar amounts of CsI:CH₃NH₃I and PbI₂ in a mixed solvent consisting of DMF:GBL (97:3 [vol.%]) at a concentration of 120 mg/ml. Solutions were stirred at 60 °C for 12 h inside glovebox filled with nitrogen gas prior to use.

For scanning electron microscope measurements (SEM, NanoSEM 230, FEI), perovskite precursor solutions were coated onto Si substrates by spin-coating at various spinrates and followed by drying at 110 °C for 10 min on a digital hotplate. For cross-sectional images of solar cells, 1.8 μ m of carbon was deposited on top of the device to prevent sample damage and a focused ion beam was used to cut thin slices (300 nm thickness) of each sample with lengths and heights of 5 μ m * 5 μ m. High-resolution transmission electron microscopy (TEM, JEM-1400) was used to obtain cross-sectional images of the samples. For X-ray diffraction (XRD) measurements, perovskite films were coated on PEDOT:PSS-coated glass substrates and diffractograms were collected using a Bruker, D8 ADVANCE at a scan rate of 2.4° min⁻¹. UV-vis absorption was measured using a Varian Cary 5000 spectrophotometer. AFM images were obtained using a Veeco Multimode AFM microscope in a tapping mode.

Device fabrication and characterization

ITO-coated glass substrates were cleaned using sequential ultrasonication in deionized water, acetone, and isopropanol for 10 min each. A solution of poly(3,4-ethylenedioxythiophene):polystyrene sulfonic acid (PEDOT:PSS) was spin-cast at 5000 rpm on UV ozone-treated ITO and dried at 140 °C for 10 min. On top of PEDOT:PSS layer, precursor solutions of Cs_xMA_{1-x}PbI₃ perovskites (120 mg/ml) were spin-cast at 5000 rpm for 90 s and dried on hot-plate at 110 °C for 10 min. A PCBM solution (7 mg/ml) in chloroform was spin-cast at 3000 rpm on top of perovskite layer. Subsequently, an Al (100 nm) electrode was deposited layer under vacuum (<10⁻⁶ Torr) on top of the PCBM by thermal evaporation. The current density-voltage (*J-V*) characteristics of PSCs were measured using a Keithley 2635A Source Measure Unit. Solar cell performance was carried out using an Air Mass 1.5 Global (AM 1.5 G) solar simulator with an irradiation intensity of 100 mW cm⁻². External quantum efficiency (EQE) measurements were obtained using a PV measurements QE system using monochromated light from a xenon lamp under ambient conditions. The monochromatic light intensity was calibrated with a Si photodiode and chopped at 100 Hz. Masks (13.0 mm²) made of thin metal were attached to each cell before measurement for *J-V* characteristics and EQE.

4.3 Results and discussion

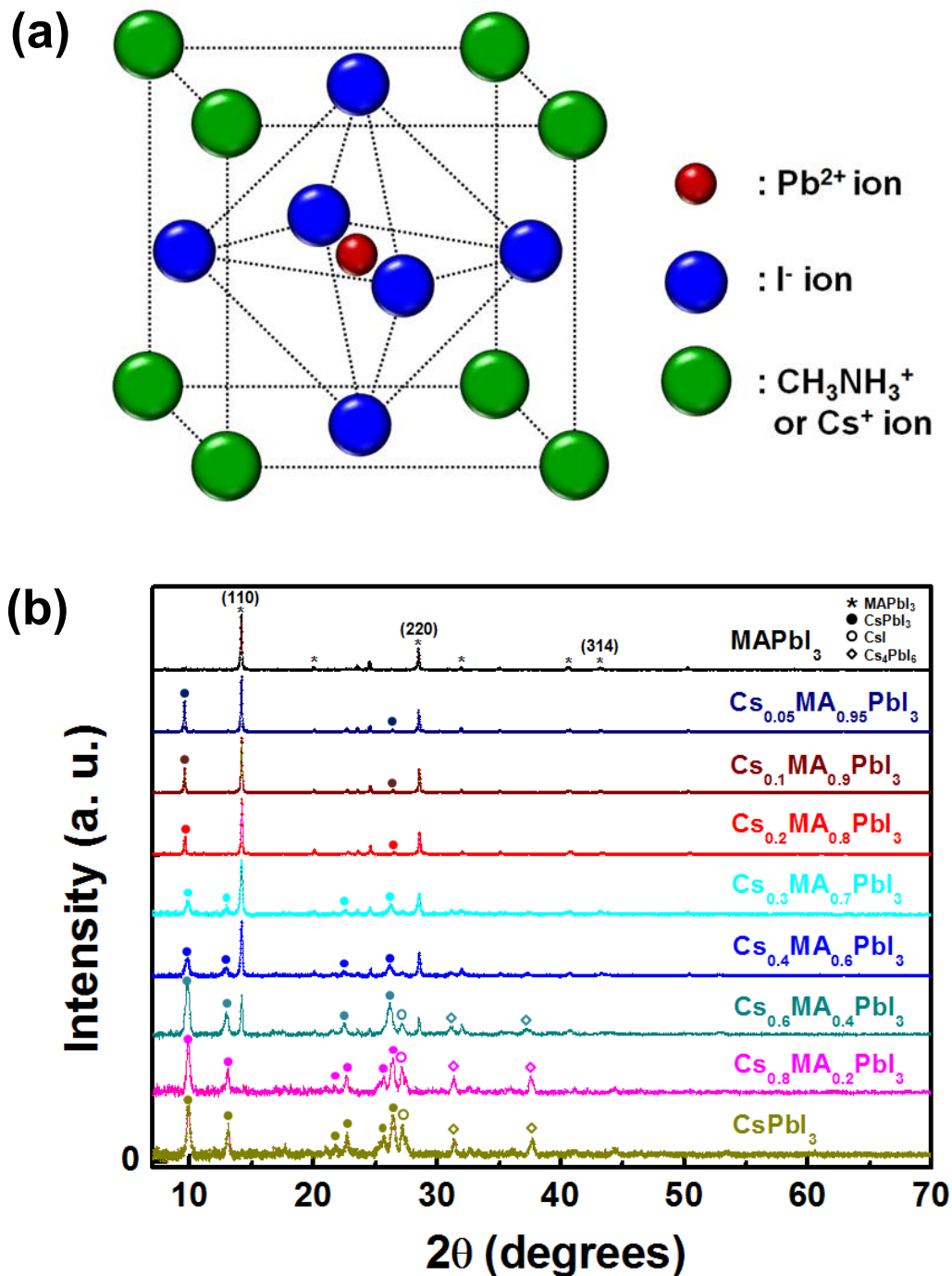


Figure 4. 1. (a) Crystal structure and (b) XRD patterns of MAPbI₃ and Cs doped MAPbI₃ perovskites.

As shown in **Figure 4. 1a**, the similar size of Cs and MA cations allows the Cs ions to substitute and coexist with MA ions in the cubo-octahedral ‘A’ sites of the octahedral unit cell without fundamentally changing the crystal structure. In order to quantify the effect of Cs incorporation on crystal structure, we collected X-ray diffractograms (XRD) of Cs_xMA_{1-x}PbI₃ perovskite films with different Cs ratio deposited on poly(3,4-ethylenedioxythio-phen):polystyrene sulfonic acid (PEDOT:PSS)-coated glass

substrates (**Figure 4. 1b**). The pure MAPbI₃ film exhibited XRD peaks at 14.15°, 20.05°, 28.47°, 31.94°, 40.66°, and 43.12°, indicating (110), (112), (220), (310), (224), and (314) crystal planes of tetragonal perovskite structure, respectively.⁴⁶ However, there was absence of several diffraction peaks including the peak corresponding to (310) crystal plane, which may be attributed to prefer growth orientation during the formation of perovskite films.^{27, 43, 46, 47} For pure CsPbI₃ film, we observed strong diffraction peaks at 9.82°, 13.07°, 22.72°, 25.70°, and 26.39°, indicating orthorhombic crystal structure.^{48, 49} There were negligible differences in diffraction peaks of films between pure CsPbI₃ and Cs_xMA_{1-x}PbI₃ perovskite with 80% Cs, whereas XRD peaks corresponding to the MAPbI₃ phase are clearly seen for $0 \leq x \leq 0.6$. The intensities of XRD peaks gradually increased for CsPbI₃ crystal and decreased for MAPbI₃ crystal upon increasing Cs ratio in Cs_xMA_{1-x}PbI₃ perovskite films. It is worth noticing that the XRD patterns clearly showed both MAPbI₃ and CsPbI₃ crystal phases for Cs_xMA_{1-x}PbI₃ perovskite from $x = 0.05$ to 0.6, which imply that Cs coexist in A site of ABX₃ perovskite crystal with MA ions and successful substitution of MA with Cs.

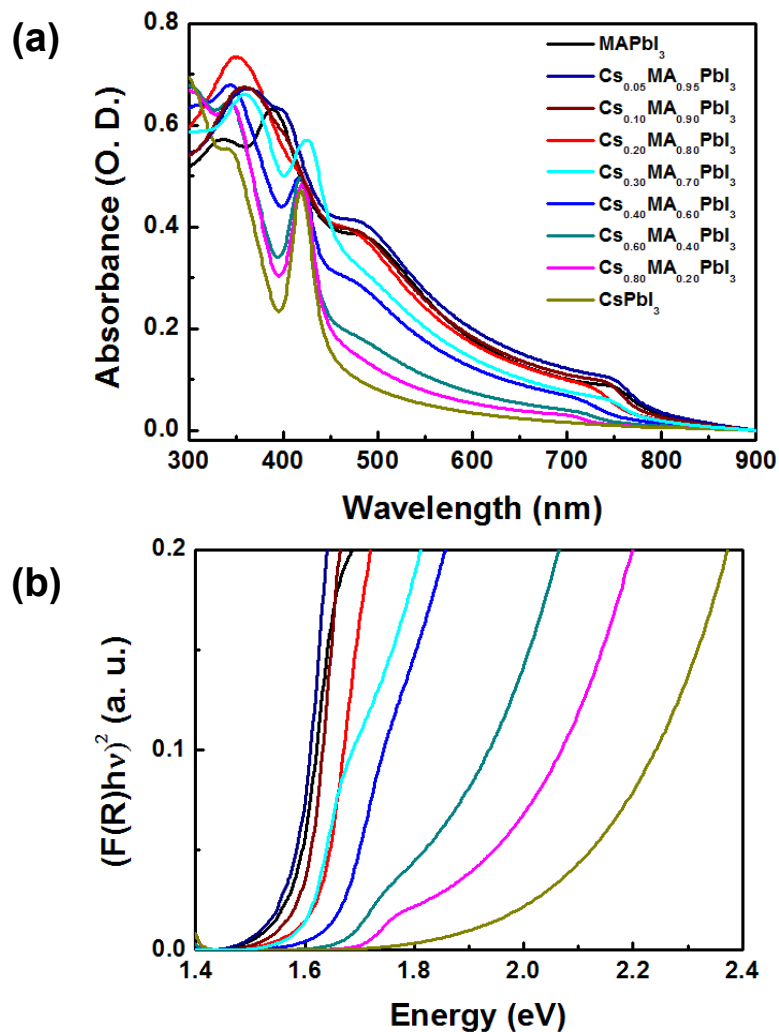


Figure 4. 2. (a) UV-vis absorption and (b) transformed Kuberka-Munk spectra of CsXMA_{1-x}PbI₃ perovskite films with different Cs ratio.

Table 4. 1. Optical band gap of $\text{Cs}_x\text{MA}_{1-x}\text{PbI}_3$ perovskite with different Cs ratio obtained from transformed Kubelka-Munk spectra.

Materials	E_g (eV)
MAPbI₃	1.52
Cs_{0.05}MA_{0.95}PbI₃	1.51
Cs_{0.10}MA_{0.90}PbI₃	1.54
Cs_{0.20}MA_{0.80}PbI₃	1.57
Cs_{0.30}MA_{0.70}PbI₃	1.58
Cs_{0.40}MA_{0.60}PbI₃	1.62
Cs_{0.60}MA_{0.40}PbI₃	1.68
Cs_{0.80}MA_{0.20}PbI₃	1.72
CsPbI₃	2.05

To investigate the change in optical properties of perovskite as a function of Cs content, UV-vis absorption and XRD patterns were collected for films with compositions of the formula $\text{Cs}_x\text{MA}_{1-x}\text{PbI}_3$ in which x was varied from 0 to 1 (**Figure 4. 2a**). Pure MAPbI₃ ($x = 0$) and CsPbI₃ ($x = 1$) absorb light in the visible and UV wavelength regions, respectively, due to their different optical band gaps.^{14, 26, 48, 50} Increasing the amount of Cs increases absorption in the range of 300–400 nm and decreases absorption in the range of 450–800 nm. Perovskite films with more than 30% Cs substitution exhibit a unique absorption peak at 420 nm characteristic of CsPbI₃, indicating that optical properties begin to reflect the CsPbI₃ phase for $x > 0.3$. Transformed Kubelka-Munk spectra from UV-vis absorption results clearly showed the changes in optical band gap of $\text{Cs}_x\text{MA}_{1-x}\text{PbI}_3$ perovskite with different Cs ratio (**Figure 4. 2b**). Optical band gap of $\text{Cs}_x\text{MA}_{1-x}\text{PbI}_3$ perovskite gradually increased from 1.52 eV for pure MAPbI₃ to 2.05 eV for pure CsPbI₃ by increasing Cs content (**Table 4. 1**), which imply that optical band gap can be easily tuned by controlling the Cs amount in $\text{Cs}_x\text{MA}_{1-x}\text{PbI}_3$ perovskite films.

To clarify the differences between the morphologies of MAPbI₃ and Cs_{0.1}MA_{0.9}PbI₃ perovskite films, we collected scanning electron microscopy (SEM) and atomic force microscopy (AFM) images of the films. In the SEM top-view images (**Figure 4. 3a** and **4. 3b**), both perovskite films exhibit typical patterns of perovskite crystals, comprising uniform crystal domains with grain sizes of less than 100 nm. In both cases, the perovskite layer completely covers the underlying PEDOT:PSS layer. These uniform morphologies are consistent with AFM topography images (**Figure 4. 3c** and **4. 3d**). Both films

exhibit smooth surfaces with root-mean-square (rms) roughnesses of 6.60 nm for MAPbI₃ and 8.08 nm for Cs_xMA_{1-x}PbI₃. In order to confirm the incorporation of Cs in the Cs_{0.1}MA_{0.9}PbI₃ films, we also performed elemental mapping using energy dispersive spectroscopy (EDS). **Figure 4. 4a and 4. 4b** show the components of MAPbI₃ and Cs_{0.1}MA_{0.9}PbI₃ such as carbon (C), nitrogen (N), lead (Pb), iodine (I), and cesium (Cs). The EDS measurement for Cs_{0.1}MA_{0.9}PbI₃ perovskite films detected Cs element along with the same elements observed in MAPbI₃ perovskite (**Figure 4. 4b**). The detailed weight and atomic percentages of chemical elements in MAPbI₃ and Cs_{0.1}MA_{0.9}PbI₃ perovskite were summarized in **Table 4. 2**.

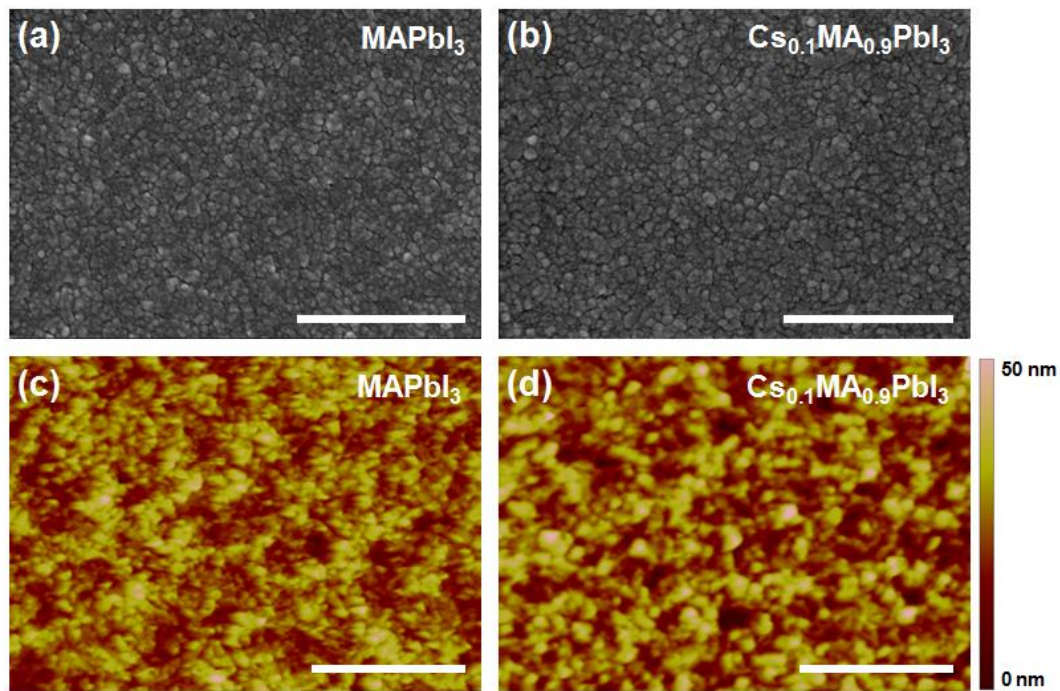


Figure 4. 3. (a, b) SEM and (c, d) AFM topography images of MAPbI₃ and Cs_{0.1}MA_{0.9}PbI₃ perovskite films. Scale bar is 1 μm.

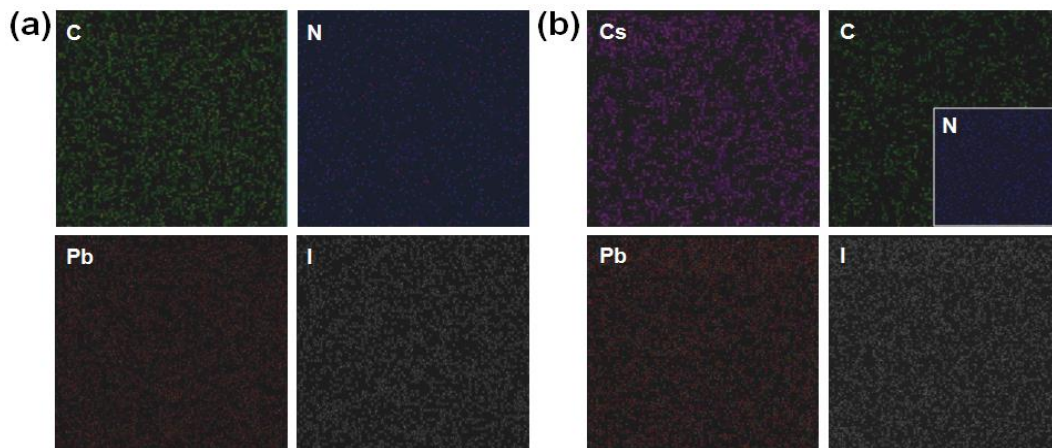


Figure 4. 4. (a, b) SEM top view images and (c, d) elemental mapping by energy dispersive spectroscopy (EDS) of MAPbI₃ and Cs_{0.1}MA_{0.9}PbI₃ perovskite films. Scale bar is 1 μm

Table 4. 2. Weight and atomic percent content of chemical elements in MAPbI₃ and Cs_{0.1}MA_{0.9}PbI₃ perovskite films.

Element	MAPbI ₃		Cs _{0.1} MA _{0.9} PbI ₃	
	Weight %	Atomic %	Weight %	Atomic %
C K	20.71	63.94	6.94	45.46
N K	6.93	18.35	0.79	4.45
I L	42.01	12.28	60.61	37.55
Pb M	30.34	5.43	2.45	1.45
Cs L	0.00	0.00	29.21	11.08

To evaluate the effect of Cs doping on device performance, we fabricated devices in the configuration of indium tin oxide (ITO)/PEDOT:PSS/perovskite/PCBM/Al. We employed perovskite films with different amounts of Cs in order to optimize Cs content for solar cell performance. **Figure 4. 5a** and **4. 5b** show the current density versus voltage (J-V) curves and external quantum efficiency (EQE) of devices utilizing Cs_xMA_{1-x}PbI₃ perovskite films as both light absorbers and electron donors. The device with pure MAPbI₃ perovskite exhibits a short-circuit current density (J_{SC}) of 8.89 mAcm⁻², an open-circuit voltage (V_{OC}) of 0.89 V, and a fill factor (FF) of 0.70, resulting in a power conversion efficiency (PCE) of 5.51%. In contrast, we obtained poor device performance in the device with pure CsPbI₃ (J_{SC} : 0.26 mAcm⁻², V_{OC} : 0.79 V, FF: 0.45, and PCE: 0.09%). Efficiencies of devices with Cs_xMA_{1-x}PbI₃ films started to decrease for $x > 0.1$, which can be attributed to relatively wider band gap of CsPbI₃ and the presence of extraneous crystal phases (CsI, PbI₂, and Cs₄PbI₆). It is worth noticing that the devices with Cs_xMA_{1-x}PbI₃ had high V_{OC} values over 1.0 V for $0.05 \leq x \leq 0.6$. The small amount of Cs doping process below 10% leads to remarkable improvement in device performance. The composition with 10 % Cs leads to the best performance. The optimized device with Cs_{0.1}MA_{0.9}PbI₃ produced a J_{SC} of 10.10 mAcm⁻², a V_{OC} of 1.05 V, and FF of 0.73, yielding a PCE of 7.68%. The increase in device efficiency is largely due to ~14% and ~18% enhancements in J_{SC} and V_{OC} , respectively, compared to those of the device with MAPbI₃. Detailed device characteristics are summarized in **Table 4. 3**. The V_{OC} value is determined by the energy difference between highest occupied molecular orbital (HOMO) or valence band (VB) of electron donor and lowest unoccupied molecular orbital (LUMO) or conduction band (CB) of electron acceptor (ED(HOMO or VB)-EA(LUMO or CB)) in heterojunction solar cells. The $E_{D(VB)}-E_{A(LUMO)}$ of perovskite/PCBM HSCs is about 1.1 eV, indicating that V_{OC} values can be improved by Cs doping.

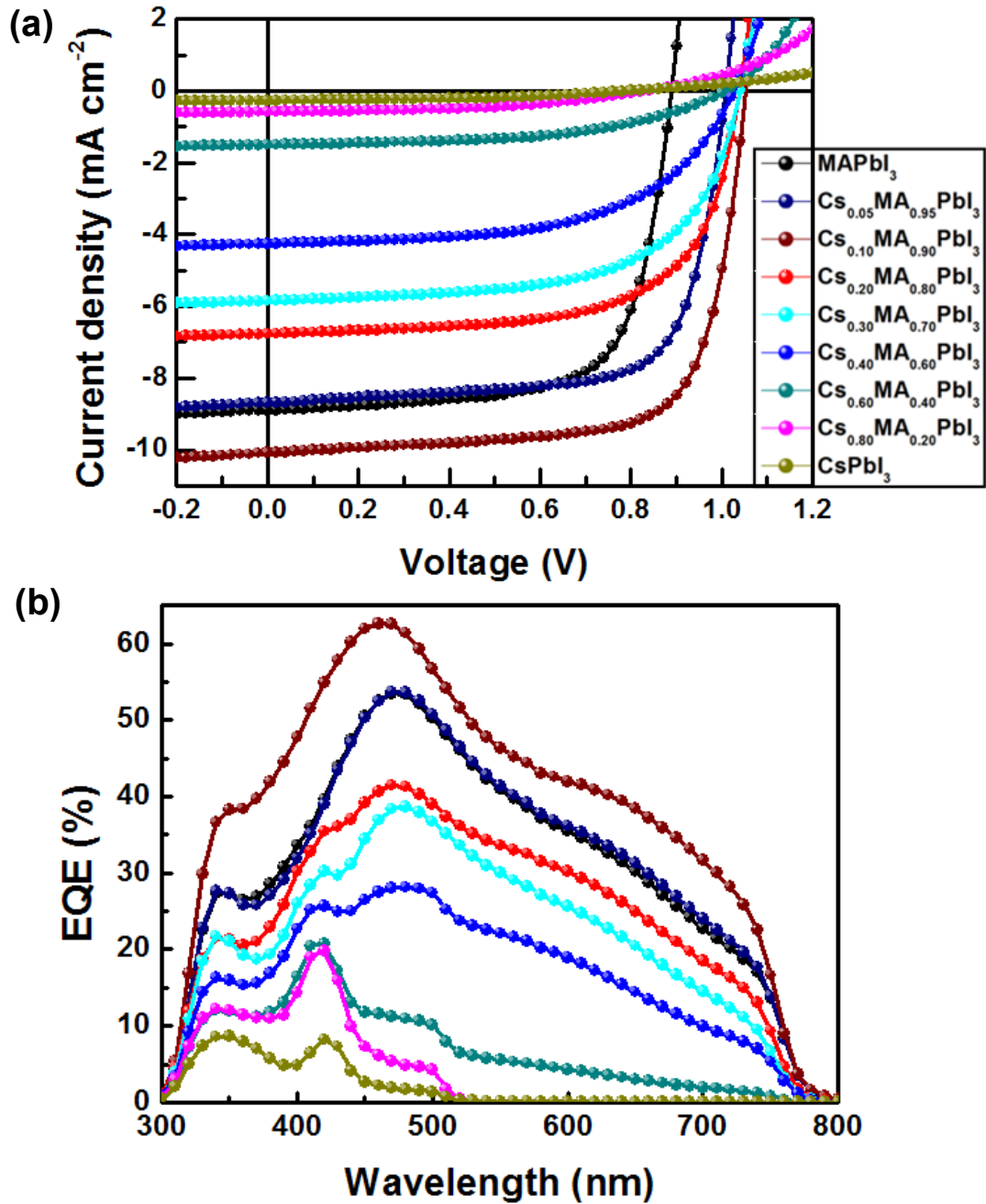


Figure 4. 5. (a) J - V characteristics and (b) EQE of the devices with Cs_xMA_{1-x}PbI₃ perovskite with different Cs ratio.

The high V_{OC} over 1 V may be attributed to an increased energy difference between the VB of the perovskite and LUMO of PCBM due to Cs doping of the perovskite (change in quasi-Fermi level: 0.10 eV) (**Figure 4. 6** and **Table 4. 4**). The VB value of MAPbI₃ obtained from ultraviolet photoelectron spectroscopy (UPS) was in good agreement with previous report. In **Figure 4. 5b**, we compared the EQE curves of the devices using Cs_xMA_{1-x}PbI₃ perovskite with different Cs ratio. The device with pure MAPbI₃ exhibits broad EQE in the range of 300-800 nm with a peak of 53.5% at 470 nm. The devices

with $\text{Cs}_x\text{MA}_{1-x}\text{PbI}_3$ perovskite films for $x \leq 0.4$ had specific EQE peak around 470 nm, whereas the EQE peak at 420 nm gradually increased for $x > 0.2$. In particular, the EQE values were significantly decreased in longer wavelength region above 430 nm upon increasing Cs ratio in the devices with $\text{Cs}_x\text{MA}_{1-x}\text{PbI}_3$. These tendencies were consistent with UV-vis absorption spectra of perovskite films (**Figure 4. 2a**). The best device with $\text{Cs}_{0.1}\text{MA}_{0.9}\text{PbI}_3$ shows the highest EQE values over the entire visible spectrum with a maximum EQE of 62.6 % at 470 nm. This J_{SC} enhancement results from improved light absorption at optimum device thickness (**Figure 4. 7**) and absorption difference between two perovskite films was in good agreement with EQE enhancement by 10% Cs doping (**Figure 4. 8**). Although we tested long-term stability of the devices with MAPbI_3 and $\text{Cs}_{0.1}\text{MA}_{0.9}\text{PbI}_3$ perovskite in ambient condition (temperature: 20 °C, humidity: 11%), there were poor device stabilities for both devices due to acidic nature of PEDOT:PSS and easily-oxidized Al electrode which were used in inverted device architecture (**Figure 4. 9**).

Table 4. 3. Characteristics of iPH-HSCs with $\text{Cs}_x\text{MA}_{1-x}\text{PbI}_3$ perovskite with different Cs ratio.

Perovskite	J_{sc} (mA cm ⁻²)	V_{oc} (V)	FF	PCE (%)	J_{sc} [Cal.] (mA/cm ²)
MAPbI₃	8.89	0.89	0.70	5.51	8.55
Cs_{0.05}MA_{0.95}PbI₃	8.69	1.01	0.72	6.29	8.68
Cs_{0.10}MA_{0.90}PbI₃	10.10	1.05	0.73	7.68	10.22
Cs_{0.20}MA_{0.80}PbI₃	6.76	1.04	0.65	4.58	6.92
Cs_{0.30}MA_{0.70}PbI₃	5.85	1.04	0.62	3.78	5.97
Cs_{0.40}MA_{0.60}PbI₃	4.26	1.03	0.57	2.50	4.44
Cs_{0.60}MA_{0.40}PbI₃	1.50	1.01	0.52	0.79	1.51
Cs_{0.80}MA_{0.20}PbI₃	0.58	0.84	0.46	0.22	0.65
CsPbI₃	0.26	0.79	0.45	0.09	0.28

Table 4. 4. Work functions of MAPbI_3 and $\text{Cs}_{0.1}\text{MA}_{0.9}\text{PbI}_3$ perovskites obtained from UPS measurements.

	MAPbI ₃	CsMAPbI ₃
Work function (eV)	5.39	5.49

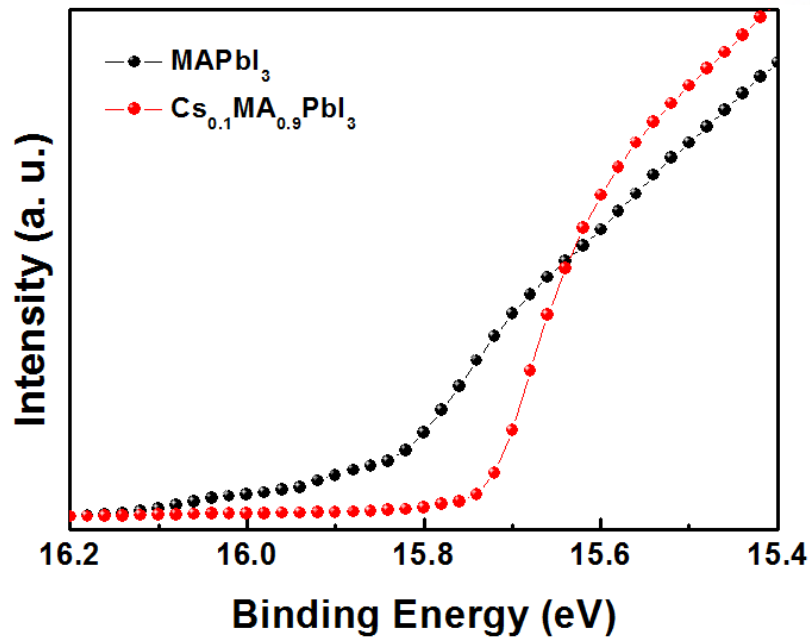


Figure 4. 6. Secondary edge regions for MAPbI₃ and Cs_{0.1}MA_{0.9}PbI₃ perovskite films on PEDOT:PSS-coated ITO substrates.

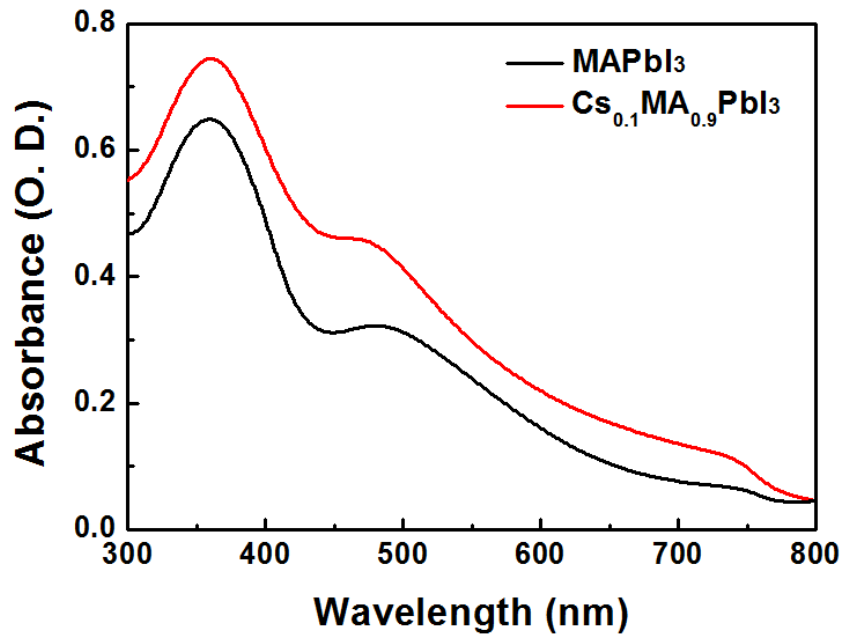


Figure 4. 7. UV-vis absorption spectra of MAPbI₃ and Cs_{0.1}MA_{0.9}PbI₃ perovskite films with optimum device thicknesses.

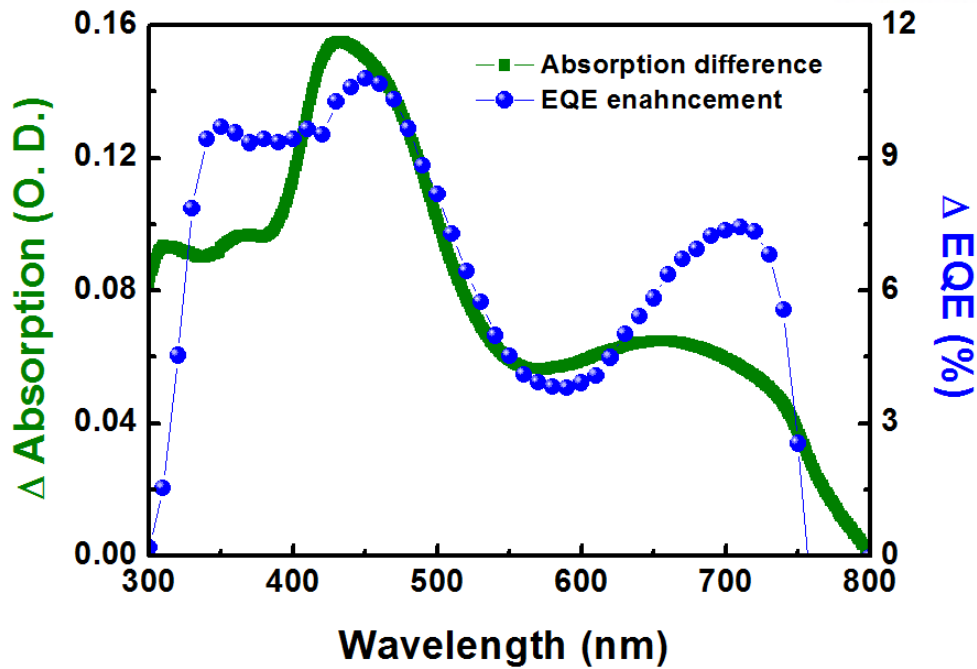


Figure 4. 8. Comparison between the change in absorption (Δ absorption) and EQE enhancement (Δ EQE) for devices using MAPbI₃ and Cs_{0.1}MA_{0.9}PbI₃ perovskites.

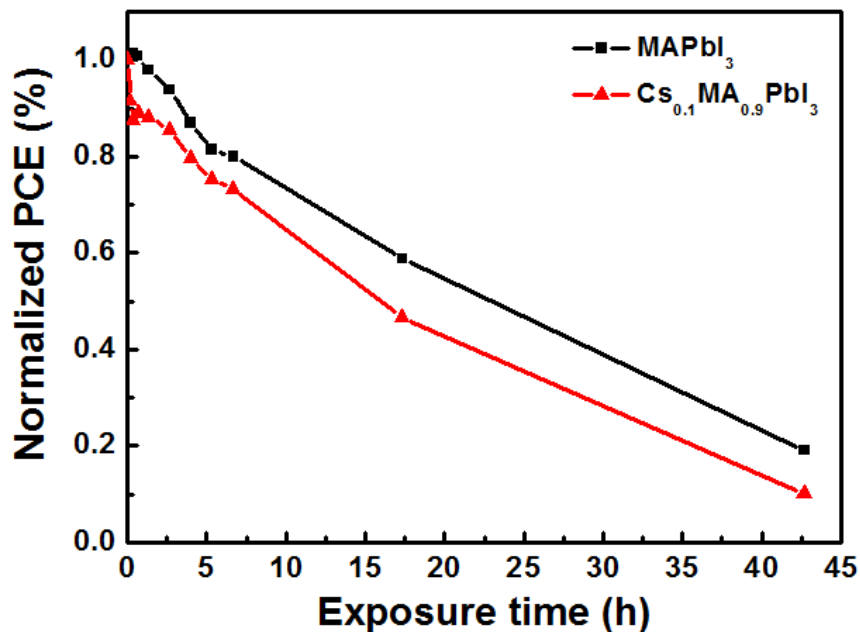


Figure 4. 9. Long-term stability of devices with MAPbI₃ and Cs_{0.1}MA_{0.9}PbI₃ perovskites under ambient conditions (temperature: 20 °C and humidity: 11%).

Figure 4. 10 shows cross-sectional transmission electron microscopy (TEM) images of optimized devices with MAPbI₃ and Cs_xMA_{1-x}PbI₃ perovskites. Each layer and corresponding thickness can clearly be seen in these images (average thickness of ITO: 140 nm, PEDOT:PSS: 35 nm, PCBM: 50 nm, and Al: 100 nm). We find that the optimal device thickness of MAPbI₃ perovskite (30 ± 11 nm)

(Figure 4. 10a) is thinner than $\text{Cs}_x\text{MA}_{1-x}\text{PbI}_3$ (38 ± 9 nm) (Figure 4. 10b), indicating that the improved J_{SC} in the $\text{Cs}_x\text{MA}_{1-x}\text{PbI}_3$ film is partially due to a thicker film. Compared to the device with MAPbI_3 , the higher FF of the device using $\text{Cs}_x\text{MA}_{1-x}\text{PbI}_3$ can be attributed to a better contact at the perovskite/PCBM and PCBM/Al interfaces due to the more even surface of the $\text{Cs}_x\text{MA}_{1-x}\text{PbI}_3$ film and smoother surface after PCBM coating (Figure 4. 11).

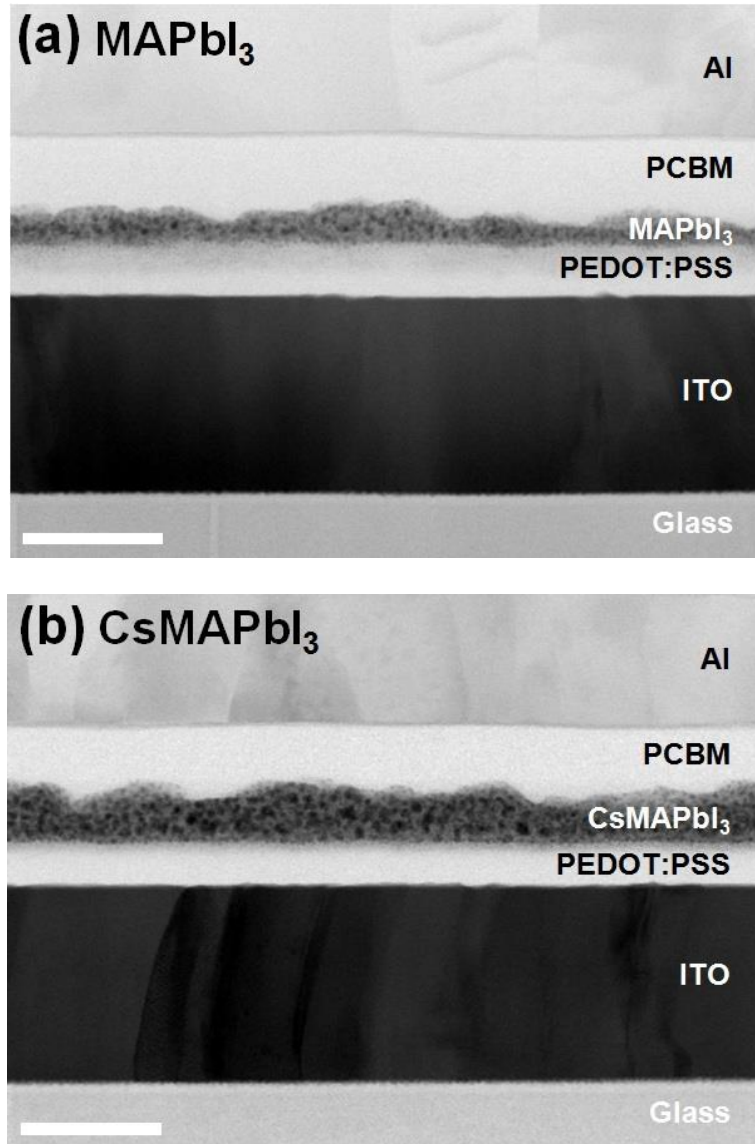


Figure 4. 10. Cross-sectional TEM images of the devices with (a) MAPbI_3 and (b) CsMAPbI_3 perovskite films as light absorber. Scale bar is 100 nm.

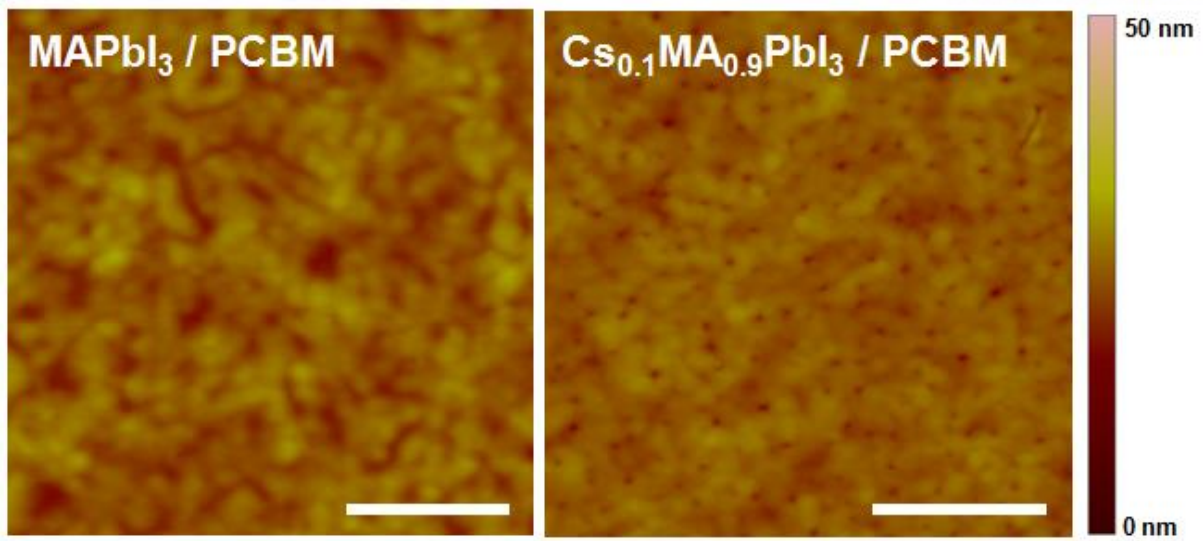


Figure 4. 11. AFM topography images of PCBM films spin-coated on top of MAPbI₃ and Cs_{0.1}MA_{0.9}PbI₃ perovskite layers. The scale bar is 1 μm.

4.4 Conclusion

In conclusion, we synthesized a series of perovskite light absorbers with composition $\text{CsXMA}_{1-x}\text{PbI}_3$ and evaluated their performance in p-i-n type perovskite/PCBM hybrid solar cells. High performance was achieved via 10% Cs doping in the MAPbI_3 perovskite structure, resulting in a ~40% enhancement in device efficiency via improvement in light absorption and morphology as well as an increased energy difference between the valence band of perovskite and LUMO level of PCBM. Our approach to perovskite design offers the possibility to enhance the performance of conventional perovskite solar cells with n-type titania or alumina layers and to achieve even higher open-circuit voltages by employing tandem device structures.

CHAPTER 5. Ternary Halide Perovskites for Highly Efficient Solution-Processed Hybrid Solar Cells

The content of this chapter is published in *ACS. Energy Lett.* **1**, 712 (2016)

5.1 Research background

Organometallic lead halide perovskites with the structure ABX_3 (where A is an organic or inorganic cation, B is a metal cation and X is halogen anion) have emerged as low-cost, solution-processible, light absorbing materials for next-generation solar cells. Their easily tunable structures can yield a wide range of band gaps and absorption characteristics, while their long charge carrier diffusion lengths and outstanding electronic properties have made them the focus of an immense, global research effort over the past several years.^{3, 4, 21} Since Kojima *et al.* first reported a solution processable $CH_3NH_3PbI_3$ (MAPbI₃) perovskite solar cells (PeSCs) with a power conversion efficiency (PCE) of 3.8%,⁶ there have been many studies which have focused on enhancing the efficiency of hybrid PeSCs.^{8, 18, 19, 29, 51} Recent studies have reported that PCE of n-i-p (n-type, intrinsic, p-type) PeSCs have achieved over 20% in a metal oxide-based mesoporous architecture.^{10, 11}

In contrast to the perovskite layers which can be deposited at near ambient temperatures, n-i-p hybrid perovskite devices require over 400 °C annealing temperatures to prepare the n-type TiO₂ layer, which currently poses an obstacle to economical processing and flexible devices. Additionally, the n-i-p structure requires a p-type hole conductor which is heavily doped by atmospheric oxygen via incorporation of *tert*-butyl pyridine (tBP) or Li-bis(trifluoromethanesulfonyl)imide (Li-TFSI), which leads to devices with poor chemical stability and sensitivity to moisture.^{3, 30, 32, 52} To surmount these limitations, the p-i-n (p-type, intrinsic, n-type) device layout is an attractive alternative to the n-i-p perovskite solar cell architecture. First, the p-i-n structure uses a stable p-type (PEDOT:PSS) layer to extract holes instead of materials which are doped with reactive liquids, air and so on.^{34, 53-56} Second, the p-i-n structure can be fabricated at low temperatures using solution processed PEDOT:PSS and (PC₆₁BM) layers which serve as effective hole and electron extraction layers, respectively, without requiring any high temperature sintering steps.⁵⁷

Relationships between chemical composition, opto-electronic properties and device characteristics remain incompletely understood in lead halide perovskite materials and constitute another critical area of research.^{14, 27, 58-61} Several studies have identified improved performance in Perovskite devices by replacement of the A cation and X halide anions with other organic cations and halogen anions, respectively. For example, Pang *et al.* Synthesized the formamidinium containing perovskite,

$\text{NH}_2\text{CH}=\text{NH}_2\text{PbI}_3$ (FAPbI₃), which possesses a broadened absorption range of up to 870 nm and narrower (1.43 eV) band gap compared to MAPbI₃ (with absorption onset and bandgap of 820 nm and 1.51, respectively), allowing 6% more light to be absorbed.⁴⁵ Strank *et al.* discovered that the charge carrier diffusion length of $\text{CH}_3\text{NH}_3\text{PbI}_{3-x}\text{Cl}_x$ (MAPbI_{3-x}Cl_x) absorber can be extended to over 1 μm by incorporating Cl into the perovskite structure, whereas the pristine MAPbI₃ absorber possesses a much shorter diffusion length of 100 nm.⁴ Recently, Liang *et al.* reported the use of ternary halide perovskite materials incorporating I, Cl and Br components by mixing two binary precursors.⁶² Although the PCE of the 3 components system was less than binary system in Liang's study, there remains considerable opportunity to investigate and improve the material properties of ternary halide perovskites through tuning the material composition.

Here, we demonstrate ternary halide p-i-n planar heterojunction PeSCs prepared via a low temperature solution-processing route. Previous literature has shown that high efficiency devices prepared from precursor solutions containing binary mixtures of Cl⁻ and I⁻ ions yield films with negligible Cl⁻ content after the film has been dried and annealed, as most of the Cl⁻ volatilizes as $\text{CH}_3\text{NH}_3\text{Cl}$ (MACl) during the annealing step. Despite the low concentration of Cl⁻ in the finished film, this halide is closely involved in formation of the perovskite film. In this work, likewise, Cl⁻ atoms play the role of a 'bridge' which assist the formation of high quality semiconducting films as I⁻ is substituted with Br⁻, but volatilizes before the films have been completed. The processing used in this study conveniently involves incorporation of PbBr_2 into binary MAPbI_{3-x}Cl_x precursor solutions and similar device processing as used in binary perovskite materials while allowing the proportions of the three halides to be easily controlled in order to modulate and optimize film properties. Since the final Cl⁻ content in the film remains small, we refer to ternary halide perovskite as $\text{CH}_3\text{NH}_3\text{PbI}_{3-y-x}\text{Br}_y\text{Cl}_x$ (MAPbI_{3-y-x}Br_yCl_x) (where x and y are the relative molar quantities of PbCl_2 and PbBr_2 used in the precursor solution, respectively). The solar cell architecture comprises sequentially deposited PEDOT:PSS/MAPbI_{3-y-x}Br_yCl_x/PC₆₁BM/Al layers on fluorine tin oxide (FTO) substrates. These devices exhibit enhanced performance from 12% to 16%, with negligible hysteresis, while retaining the desirable optical and electrical properties of binary MAPbI_{3-x}Cl_x mixtures

5.2 Experimental details

Materials and preparation of perovskite

lead chloride (PbCl_2), lead bromide (PbBr_2), anhydrous dimethylacetamide (DMA) and anhydrous *N,N*-dimethylformamide (DMF) were purchased from Sigma-Aldrich and were used without purification. Methylammonium iodide (MAI) was prepared by mixing 30 ml CH_3NH_2 (40 wt% in water, Sigma Aldrich) and 30 ml HI (57 wt% in water, Sigma Aldrich) in a 250 ml, three-neck flask at 0 °C for 2 hr with stirring. The precipitate was recovered by evaporation under vacuum at 60 °C for 1h. To purify, the MAI precursor was re-dissolved in ethanol and recrystallized from diethyl ether. Finally, the MAI product was dried at 60 °C under vacuum oven for 24 hr. To prepare $\text{MAPbI}_{3-x}\text{Cl}_x$ precursor solutions, MAI and PbCl_2 were dissolved at a 3:1 molar ratio in a mixture of DMA and DMF solution (9:1 [v/v]) with a concentration of 40 wt%. For the ternary halide $\text{MAPbI}_{3-x-y}\text{Br}_y\text{Cl}_x$ precursor solution, MAI, PbCl_2 and PbBr_2 were dissolved at a 3 : 1-y : y molar ratio in same mixed solution at 40 wt% concentration. The obtained solution was stirred at room temperature for 2 hr in air.

Device fabrication and characterization

FTO-coated glass substrates were cleaned by ultra-sonication in deionized water, acetone and isopropyl alcohol for 10 min each. A poly(3,4-ethylenedioxythiophene):polystyrene sulfonic acid (PEDOT:PSS) layer was deposited on cleaned FTO substrates by spin-casting at 3000 rpm for 40s, followed by annealing at 150 °C for 15 min. On top of PEDOT:PSS (AI4083) layer, binary and ternary halide perovskite precursor solutions were spin-cast at 5000 rpm for 30 s and dried on a hot-plate at 90 °C for 90 min in air atmosphere. On top of the perovskite layer, a 25 mg/ml solution of PC61BM in 1:1 mixture of chlorobenzene and chloroform was spin-cast at 900 rpm. Subsequently, an Al electrode with a thickness of 100 nm was deposited on the PC61BM layer under vacuum ($<10^{-6}$ Torr) by thermal evaporation. The current density-voltage (J-V) characteristics of the solar cells were measured using a Keithley 2635A Source Measure Unit. Solar cell performance was carried out under illumination by an Air Mass 1.5 Global (AM 1.5 G) solar simulator with an irradiation intensity of 100 mW cm^{-2} . Apertures (13.0 mm²) made of thin metal were attached to each cell before measurement for J-V characteristics. External quantum efficiency (EQE) measurements were obtained with a PV measurements QE system under ambient conditions, with monochromated light from a xenon arc lamp. The monochromatic light intensity was calibrated with a Si photodiode and chopped at 100 Hz. Scanning electron microscope measurements (SEM) were performed using an S-4800 Hitachi high-Technology microscope. SEM samples were prepared by coating perovskite precursor solutions onto glass substrates by spin-coating at 5000 rpm, followed by post annealing at 90 °C for 90 min on a hotplate. For X-ray diffraction (XRD) measurements, perovskite films were coated on PEDOT:PSS-coated glass substrates and diffractograms were collected using a Bruker, D8 ADVANCE diffractometer

at a scan rate of $2.4^\circ \text{ min}^{-1}$. UV-vis absorption was measured using a Varian Cary 5000 spectrophotometer. AFM images were obtained using a Veeco Multimode AFM microscope in a tapping mode.

IQE calculation

IQE of the devices were determined following a previously reported procedure. Briefly, the optical absorption of each layer inside the device was calculated using the transfer matrix method.^[38] Then parasitic absorption, that is the absorption absorbed by buffer layers and electrodes, was subtracted from the experimentally measured absorption of the fully structured device to determine the absorption of the active layer only. Finally, the ratio of the EQE and the active layer absorption spectrum were used to calculate the IQE spectrum of the devices.

5.3 Results and discussion

To gain an understanding of the optical properties and structure of ternary halide and binary perovskites, UV-vis absorption spectra and X-ray diffraction (XRD) patterns were collected for perovskite films with variable Br content. We controlled compositions of formula $\text{MAPbI}_{3-y-x}\text{Br}_y\text{Cl}_x$ in which y was varied from 0 to 1 in the precursor solution. **Figure 5. 1a** shows that calculated absorption coefficient (α) from UV-vis absorption measurement (**Figure 5. 2a**). The absorption onset of the $\text{MAPbI}_{3-y-x}\text{Br}_y\text{Cl}_x$ is slightly blue-shifted from 800 nm to 750 nm as the Br proportion increases from 0 to 1, indicating that the optical properties of the ternary materials begin to trend towards the MAPbBr_3 phase (which possesses an absorption onset of 550 nm phase) for $y > 0$ and confirm the incorporation of Br into the film. In **Figure 5. 1b**, transformed Tauc plots clearly show an increase in optical band gap with increasing Br incorporation. The optical band gap of $\text{MAPbI}_{3-y-x}\text{Br}_y\text{Cl}_x$ gradually shifts from 1.58 eV to 1.66 eV which shows that the optical band gap can be accurately tuned by adjusting the Br proportion in $\text{MAPbI}_{3-y-x}\text{Br}_y\text{Cl}_x$ perovskite films (**Table 5. 1**).

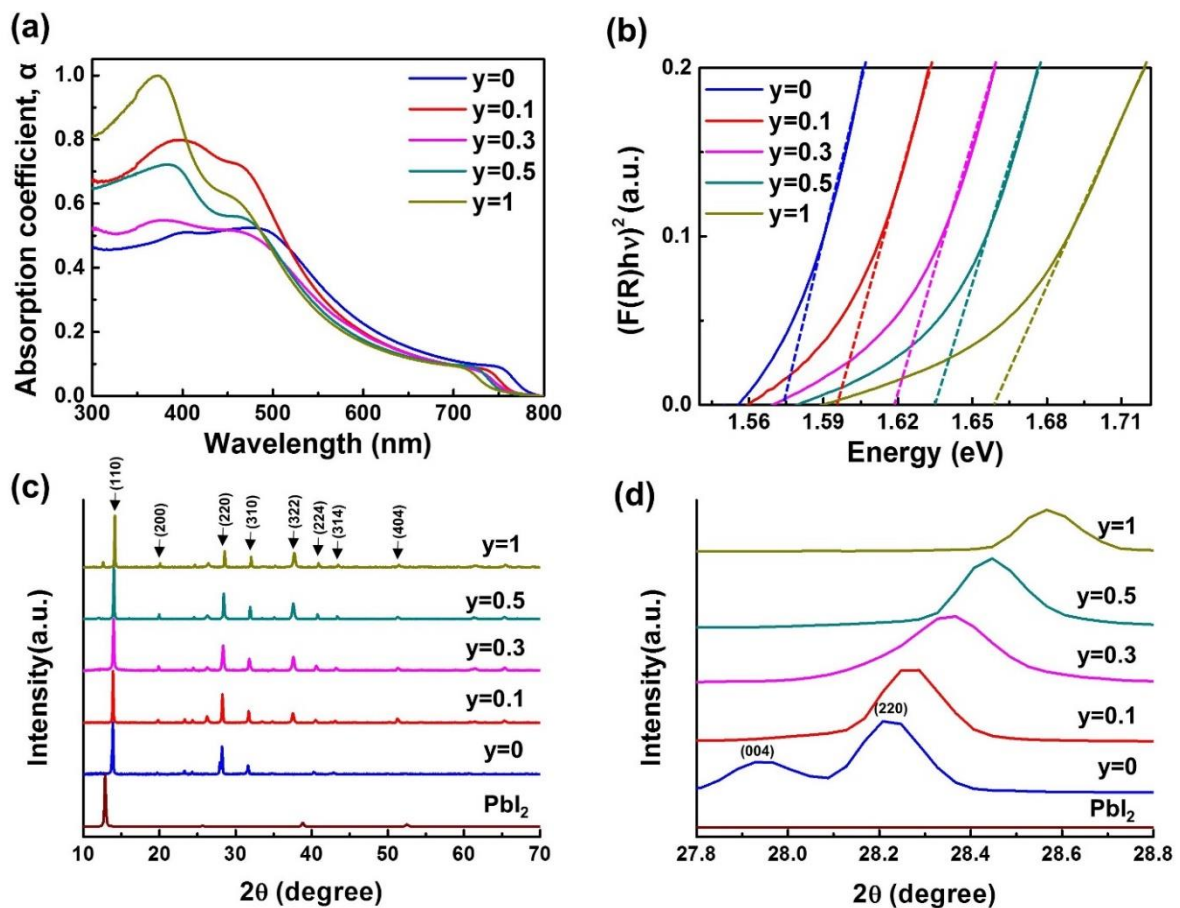


Figure 5. 1. (a) Absorption coefficient and (b) transformed Tauc-plot spectra of $\text{MAPbI}_{3-y-x}\text{Br}_y\text{Cl}_x$ perovskite films with variable Br content. (c) X-ray diffraction (XRD) patterns of perovskite films with (d) a magnified region corresponding to the tetragonal (220) and cubic (200) peaks of $\text{MAPbI}_{3-y-x}\text{Br}_y\text{Cl}_x$ ($y = 0, 0.1, 0.3, 0.5, 1$) system.

Table 5. 1. Optical band gaps of MAPbI_{3-y-x}Br_yCl_x (y = 0, 0.1, 0.3, 0.5, 1) perovskite films with different Br ratios derived from Tauc plots.

Perovskite Layer	E_g (eV)
y = 0	1.58
y = 0.1	1.60
y = 0.3	1.62
y = 0.5	1.64
y = 1	1.66

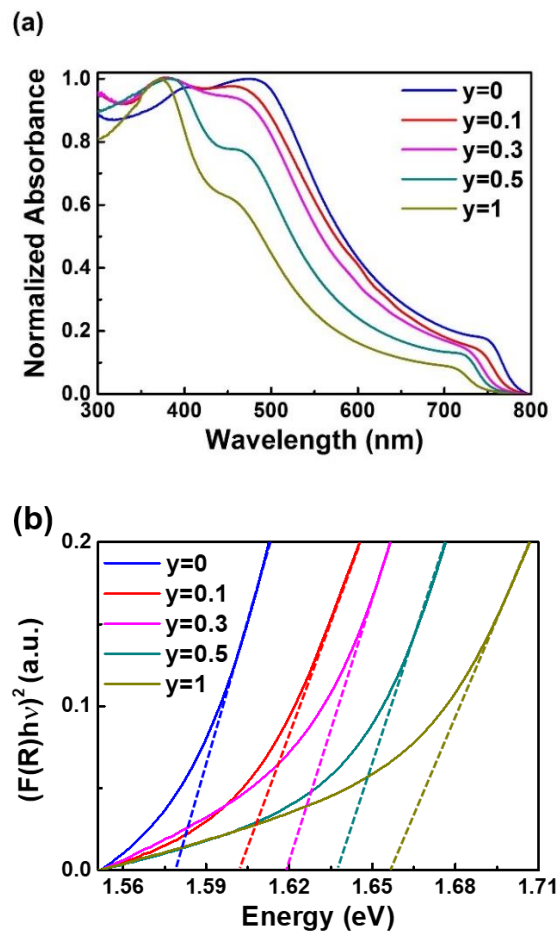


Figure 5. 2. (a) Normalized UV-vis absorption and (b) Transformed Extinction coefficient of ternary halide perovskite films with different Br ratios.

We calculate absorption coefficient using follow equation:

$$\alpha = \frac{4\pi\kappa}{\lambda} \tag{Eq. 5-1}$$

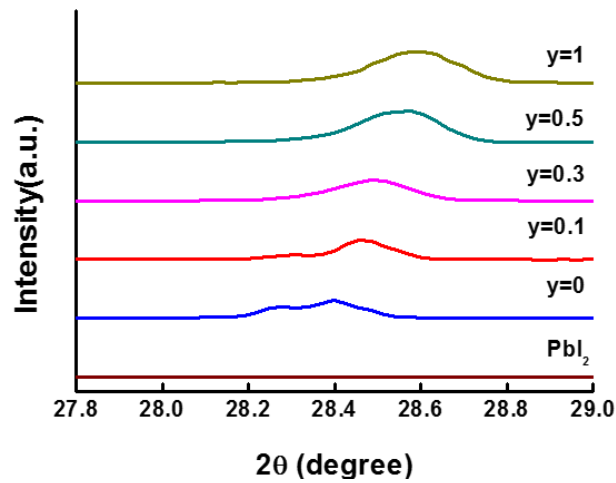


Figure 5. 3. XRD diffraction patterns for $\text{MAPbI}_{2.9-x}\text{Br}_{0.1}\text{Cl}_x$ ternary halide perovskite films deposited on glass substrates.

XRD patterns were obtained for films with different Br content deposited on glass / PEDOT:PSS coated substrates in order to examine the influence of Br incorporation on crystal structure, as shown in **figure 4. 1c**. (glass / perovskite layer is in **figure 4. 2**) Diffraction patterns of binary $\text{MAPbI}_{3-x}\text{Cl}_x$ film exhibited peaks at 14.06° , 28.21° , 31.67° and 42.83° , corresponding to (110), (220), (310), and (314) planes of the tetragonal perovskite lattice.^{46, 63, 64} For $\text{MAPbI}_{3-x}\text{Br}_x$ films, we observed strong peaks at 14.14° , 20.08° , 28.57° and 43.46° , corresponding to (100), (110), (200) and (220) planes of the cubic structure of perovskite.⁶⁵ We observed that the (220) plane for the $I4/mcm$ phase gradually disappeared and the (200) plane corresponding to the $Pm3m$ phase appeared upon increasing Br portion, as shown in **Figure 1d**.⁶ These changes that replacing I^- with Br^- can be attributed to increase tolerance factor (t) from 0.834 of MAPbI_3 to 0.844 of MAPbBr_3 , along with a shift in the 220 diffraction peak from 28.21° to 28.57° , indicating a phase transformation from tetragonal perovskite structure with $I4cm$ symmetry to cubic perovskite structure with $pm-3m$ symmetry.²² This phase transformation indicate The intensities of diffraction peaks gradually increased for $\text{MAPbI}_{3-x}\text{Br}_x$ lattice and decreased for $\text{MAPbI}_{3-x}\text{Cl}_x$ lattice upon increasing Br ratio in $\text{MAPbI}_{3-y-x}\text{Br}_y\text{Cl}_x$ films. XRD patterns were obtained for films with different Br content deposited on glass as well PEDOT:PSS coated substrates in order to examine the influence of the substrate on crystal structure, as shown in **Figure 4. 3** and **Figure 4. 1c**, respectively. Similar patterns were observed on both types of substrate, suggesting that the PEDOT:PSS did not have a dramatic texturing effect on the perovskite layer.

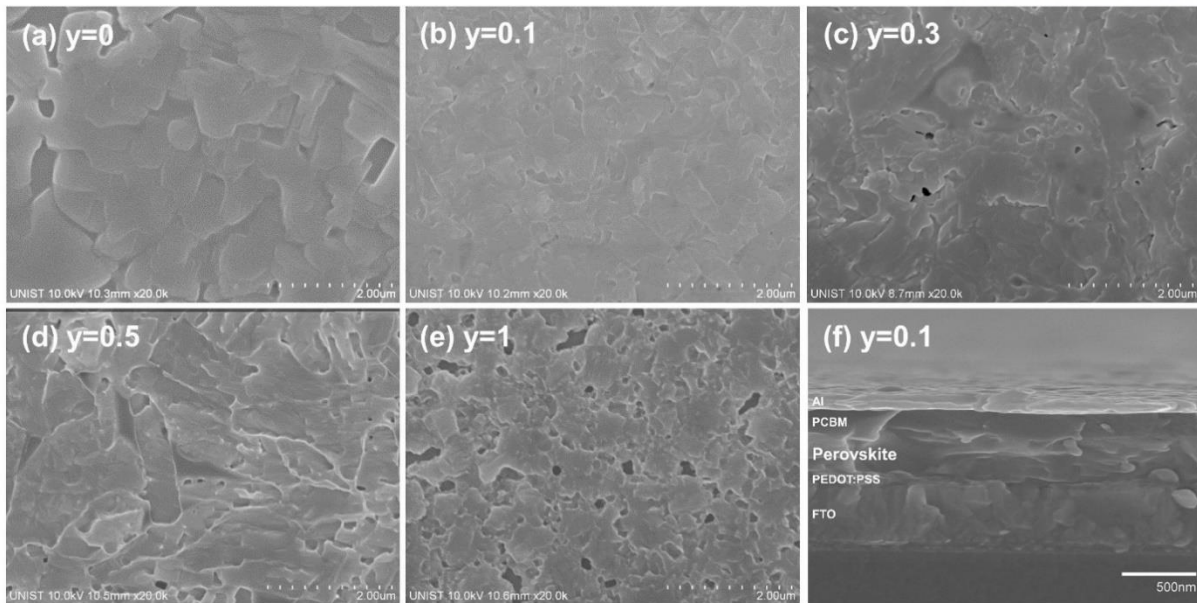


Figure 5. 4. (a-e) SEM top-view images of $\text{MAPbI}_{3-y-x}\text{Br}_y\text{Cl}_x$ ($y = 0, 0.1, 0.3, 0.5, 1$) perovskite films prepared with different Br ratios. (f) SEM cross-sectional image of $\text{MAPbI}_{2.9-x}\text{Br}_{0.1}\text{Cl}_x$.

Scanning electron microscopy (SEM) images of perovskite layers were collected to examine the influence Br proportion on film morphology. $\text{MAPbI}_{3-y-x}\text{Br}_y\text{Cl}_x$ perovskite films with variable Br content were deposited on PEDOT:PSS by spin-coating, these film morphologies are shown in **Figure 5. 4a~e**. A cross-sectional SEM image shows the completed device stack (using a ternary perovskite layer with $y = 0.1$) in **Figure 5. 4f**. Notably, films with high Br content ($y > 0.5$) did not convert to the black phase at 90°C , therefore, the annealing temperature was increased for high Br content and each film composition exhibited a different optimal annealing temperature ($y = 0$ to 0.3 : 90°C , $y = 0.5$: 110°C , $y = 1$: 120°C). As can be seen from **Figure 5. 4a**, the $\text{MAPbI}_{3-x}\text{Cl}_x$ perovskite film without Br incorporation exhibited uniform crystal domains with large grain size, however, the films tended to form large voids and depressions between grains. Upon incorporating Br into the material, the film morphology changed. The $\text{MAPbI}_{2.9-x}\text{Br}_{0.1}\text{Cl}_x$ condition yielded a homogeneous and pinhole-free morphology, which covered the hole transport layer the most completely compared to other ratios ($y = 0.3, 0.5, 1$) in the $\text{MAPbI}_{3-y-x}\text{Br}_y\text{Cl}_x$ system. Over 30% Br incorporation led to a rough, fiber-like crystalline surface. The morphological control of $\text{MAPbI}_{3-y-x}\text{Br}_y\text{Cl}_x$ perovskite layers is a key factor for achieving high performance PeSCs since homogenous crystal domains are known to increase charge carrier diffusion lengths and reduce charge recombination.^{4, 14} Moreover, pinhole-free morphologies have been attributed to reduced contact between top and bottom electrodes.^{57, 66}

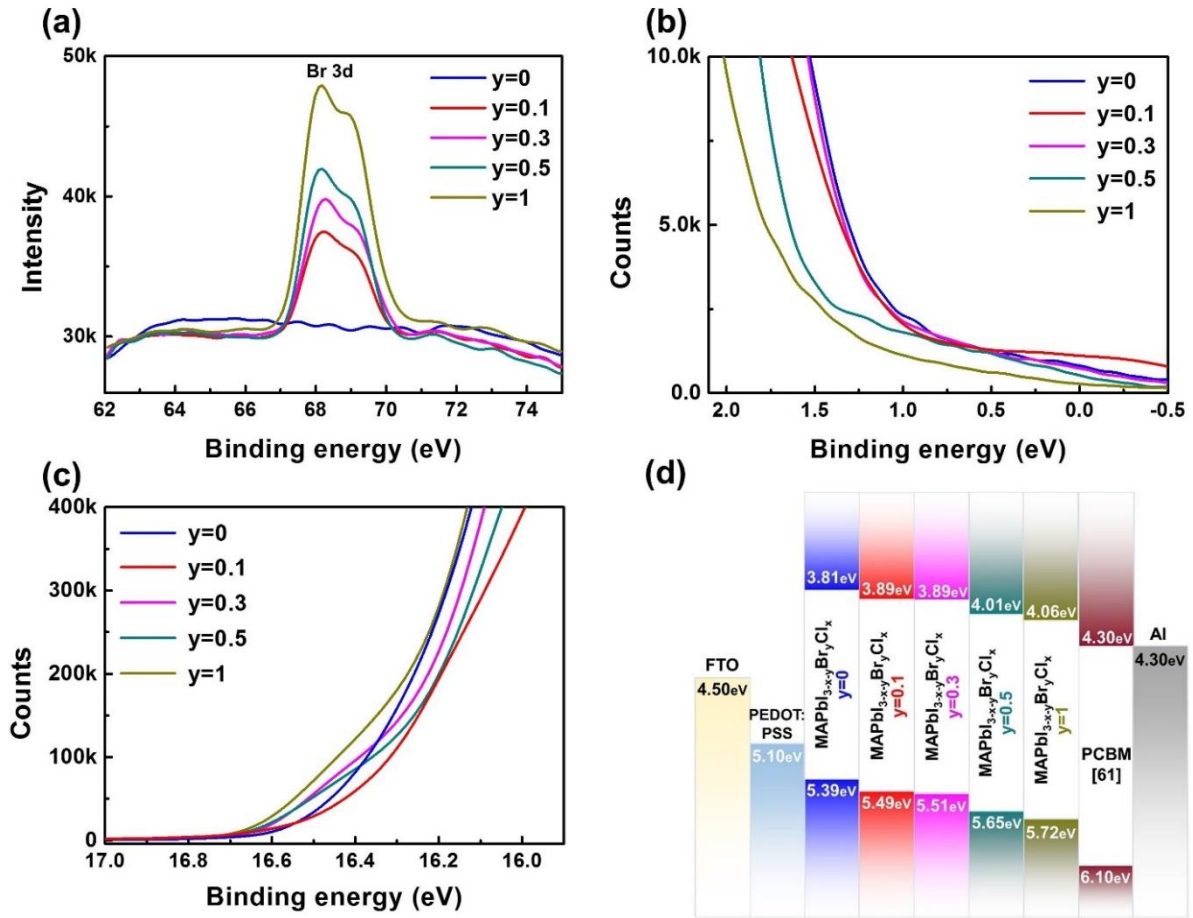


Figure 5. 5. (a) X-ray photoelectron spectra (XPS) of MAPbI_{3-y-x}Br_yCl_x (y = 0, 0.1, 0.3, 0.5, 1) films in the region of the Br 3d peak. Ultraviolet photoelectron spectra (UPS) of (b) the secondary edge region and (c) Fermi edge region of MAPbI_{3-y-x}Br_yCl_x (y = 0, 0.1, 0.3, 0.5, 1) films, plotted relative to an Au reference. (d) Band diagram of MAPbI_{3-y-x}Br_yCl_x perovskite films.

In order to develop a deeper understanding of the variation in the electrical properties of ternary perovskite as a function of Br⁻ incorporation, we performed ultraviolet photoelectron spectroscopy (UPS) and x-ray photoelectron spectroscopy (XPS) of the perovskite films. XPS analysis (**Figure 5. 5a**) clearly showed a peak corresponding to Br 3d photoemission, which gradually increased in intensity as the quantity of Br increased. A Cl 2p peak was not observed in any of the ternary halide perovskite films (**Figure 5. 6**), confirming that the Cl⁻ content evaporated during device processing. Changes in the electronic band structure of the films were characterized by UPS measurements. Valence band energies (E_v) were determined from the Fermi edge region of the photoelectron spectra (**Figure 5. 5b**) relative to an Au reference sample, while work functions were determined from the secondary edge (**Figure 5. 5c**). These results are summarized in **Table 5. 2**. As the amount of Br increased, the E_v increased from 5.39 eV to 5.72 eV. Notably, the E_v of MAPbI_{2.9-x}Br_{0.1}Cl_x was found to be 0.1 eV larger than the binary

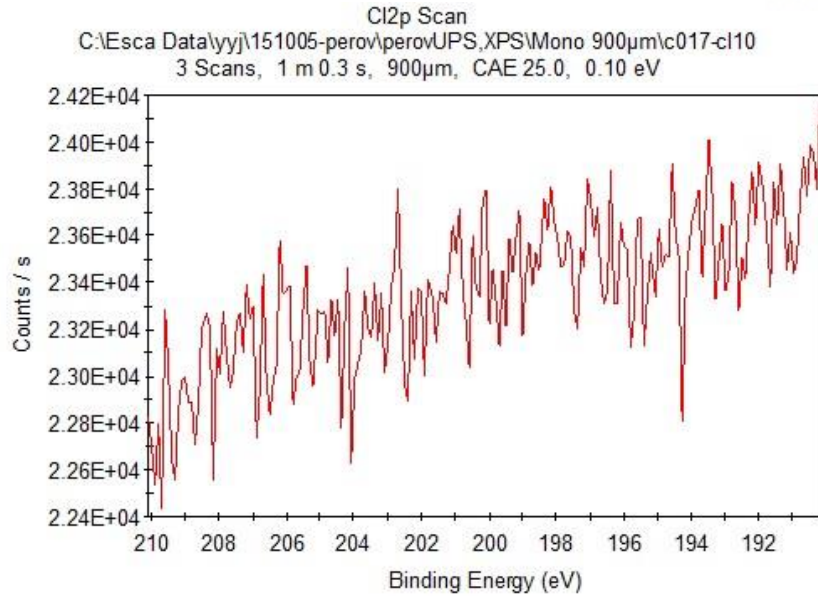


Figure 5. 6. Cl2p region of XPS spectrum of an optimized ternary halide perovskite film.

Table 5. 2. Valence band (E_V) of MAPbI_{3-y-x}Br_yCl_x ($y = 0, 0.1, 0.3, 0.5, 1$) perovskite with different Br ratios from obtained UPS measurements.

Perovskite Layer	Valence Band (E_V)
$y = 0$	5.39
$y = 0.1$	5.49
$y = 0.3$	5.51
$y = 0.5$	5.65
$y = 1$	5.72

The valence band energy (E_V) can be determined from the UPS spectra using the following equation:

$$E_V = h\nu - (E_{SE} - E_{onset}) \quad (\text{Eq. 5-2})$$

Where, $h\nu$ is photon energy from ultraviolet light source (21.2 eV He I emission), E_{SE} is secondary edge region and E_{onset} is the Fermi edge.

system MAPbI_{3-x}Cl_x, which indicates the potential for increased open-circuit voltage (V_{OC}) with Br

incorporation. Conduction band energies were estimated by adding the optical bandgap of each material to E_V . **Figure 3d** shows an energy band diagram for the $\text{MAPbI}_{2.9-x}\text{Br}_{0.1}\text{Cl}_x$ system, based on UV-vis spectra and UPS results.

To investigate the influence of different Br^- ratios on device performance, we fabricated p-i-n planar PeSCs in the configuration of FTO/PEDOT:PSS(50 nm)/perovskite active layer(300 ± 30 nm)/ PC_{61}BM (50~100 nm)/Al(100 nm). Note that the thickness of PC_{61}BM was varied to accommodate changes in the roughness of the perovskite layer, in order to prevent direct contact between the perovskite alyer and the top electrode. We employed ternary perovskite films with different amounts of Br^- incorporation in order to optimize Br^- content for photovoltaic performance. The current density-voltage (J-V) characteristics of the devices, external quantum efficiency (EQE) and summarized device characteristics are reported in **Figure 5. 7a, b**, **Table 5. 3**, **Table 5. 4** and **Table 5. 5**, respectively. The binary $\text{MAPbI}_{3-x}\text{Cl}_x$ perovskite devices exhibited a short-circuit current density (J_{SC}) of 19.8 mA cm^{-2} , V_{OC} of 0.87 V, fill factor (FF) of 0.70%, and overall PCE of 12.1%, while pure $\text{MAPbI}_{3-x}\text{Br}_x$ perovskite devices yielded poor PCEs including a J_{SC} of 12.9 mA cm^{-2} , V_{OC} of 0.87 V, FF of 61% and PCE of only 6.85% which can be attributed to poor coverage of the FTO/PEDOT electrode

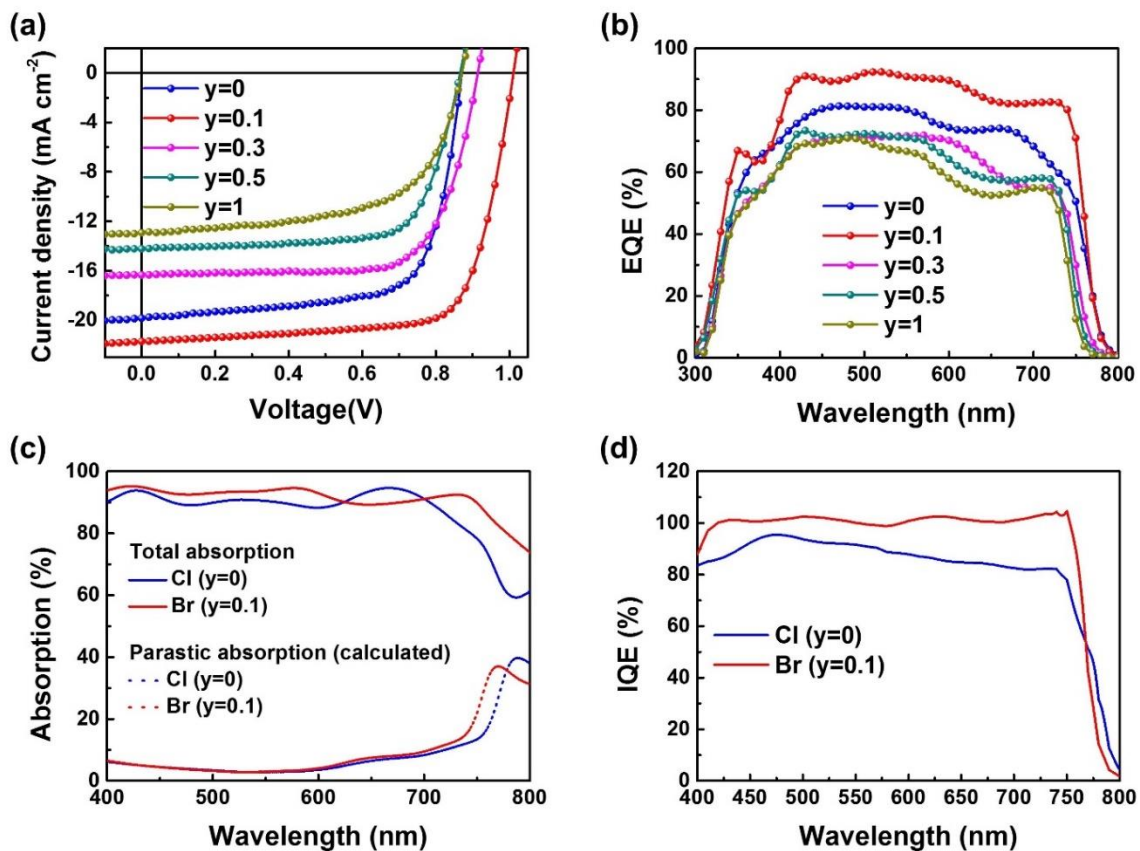


Figure 5. 7. (a) J - V characteristics and (b) EQE spectra of $\text{MAPbI}_{3-y-x}\text{Br}_y\text{Cl}_x$ ($y = 0, 0.1, 0.3, 0.5, 1$) perovskite films with different Br ratios and (c) IQE of $\text{MAPbI}_{3-y-x}\text{Br}_y\text{Cl}_x$ ($y = 0, 0.1$) (c) Full device absorption and (d) Internal quantum efficiency of $\text{MAPbI}_{3-y-x}\text{Br}_y\text{Cl}_x$ ($y = 0, 0.1$).

Table 5. 3. Solar cell characteristics of MAPbI_{3-y-x}Br_yCl_x (y = 0, 0.1, 0.3, 0.5, 1) perovskite devices with different Br ratios

Perovskite Layer	J_{sc} (mA cm ⁻²)	V_{oc} (V)	FF	PCE (%)	J_{sc} [Cal.] (mA cm ⁻²)
y = 0	19.84	0.87	0.70	12.11	18.05
y = 0.05	20.38	0.96	0.70	13.7	---
y = 0.1	21.72	1.01	0.73	16.04	21.07
y = 0.15	19.77	0.98	0.71	13.8	---
y = 0.3	16.34	0.91	0.72	10.75	15.39
y = 0.5	14.23	0.87	0.71	8.80	15.10
y = 1	12.93	0.87	0.61	6.85	14.04

Table 5. 4. MAPbI_{2.9-x}Br_{0.1}Cl_x device performance with various thermal annealing temperatures.

PC ₆₁ BM conc (mg/ml)	Thermal annealing (°C, min)	J_{sc} (mA/cm ²)	V_{oc} (V)	FF	PCE (%)
25	(70, 90)	0.13 ± 0.01	0.54 ± 0.11	0.38 ± 0.09	0.03 ± 0.01
	(90, 90)	19.72 ± 0.21	0.99 ± 0.01	0.75 ± 0.01	14.68 ± 0.12
	(110, 90)	18.50 ± 1.00	0.81 ± 0.03	0.69 ± 0.007	10.4 ± 0.37

Table 5. 5. MAPbI_{2.9-x}Br_{0.1}Cl_x device performance with various PC₆₁BM thicknesses.

PC ₆₁ BM Conc. (mg/ml)	J_{sc} (mA/cm ²)	V_{oc} (V)	FF	PCE (%)
15	18.40 ± 0.72	0.90 ± 0.06	0.65 ± 0.02	10.90 ± 1.36
201	18.30 ± 0.72	1.01 ± 0.002	0.68 ± 0.007	12.60 ± 0.39
25	19.72 ± 0.21	0.99 ± 0.01	0.75 ± 0.01	14.68 ± 0.12
30	18.10 ± 0.72	1.01 ± 0.006	0.66 ± 0.02	12.2 ± 0.45

A small amount ($y = 0.1$) of Br^- content in the perovskite precursor solution led to significantly improved J_{SC} , V_{OC} , and FF with a 30% improvement in PCE. As shown in **Figure 5. 8** and **Table 5. 6**, in particular, $\text{MAPbI}_{2.9-x}\text{Br}_{0.1}\text{Cl}_x$ ternary halide perovskite films exhibited hysteresis-free J-V characteristics, including a J_{SC} of 21.7 mA cm^{-2} , V_{OC} of 1.01 V, FF of 73%, and PCE of 16.0% in the reverse scan direction, and J_{SC} of 20.4 mA cm^{-2} , V_{OC} of 1.00 V, FF of 73%, and PCE of 15.6% in the forward scan direction under 1 sun illumination (100 mWcm^{-2} AM 1.5G). The reduced hysteresis upon incorporation Br^- may be attributed to the balance between electron and hole transport within the perovskite layer.⁶⁷⁻⁶⁹

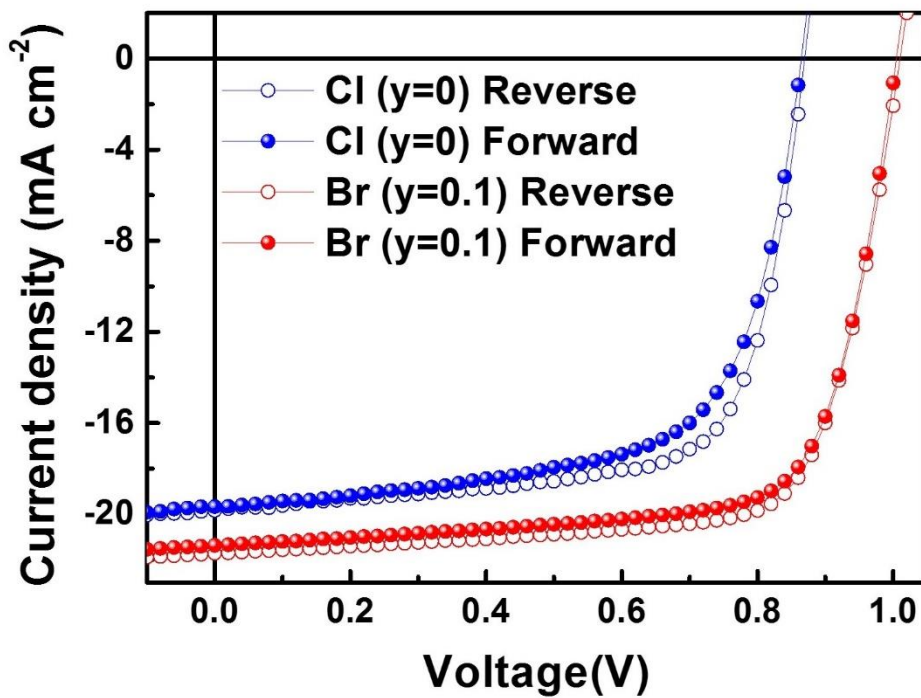


Figure 5. 8. Comparison of J - V characteristics of an optimized device in different scanning directions.

Table 5. 6. Device parameters of optimized devices in different scanning directions.

Scan Direction	J_{SC} (mA cm^{-2})	V_{OC} (V)	FF	PCE (%)
Cl ($y = 0$) Reverse	19.84	0.87	0.70	12.11
Cl ($y = 0$) Forward	19.67	0.86	0.66	11.19
Br ($y = 0.1$) Reverse	21.72	1.01	0.73	16.04
Br ($y = 0.1$) Forward	21.37	1.00	0.73	15.58

An EQE spectrum taken from a best $\text{MAPbI}_{2.9-x}\text{Br}_{0.1}\text{Cl}_x$ device shows broad spectral response in the range of 300-800 nm with a peak of 92% at a wavelength of 520 nm. This result (92%) is close to the maximum EQE value which can be attained considering reflective losses at the air/glass and glass/FTO interfaces. The difference between calculated current density (21.1 mA cm^{-2}) from EQE data and J_{SC} (21.72 mA cm^{-2}) obtained from J-V curve shows only 3% mismatch which indicates good agreement and substantiates the observed J_{SC} . Given that the EQE is close to the theoretical maximum, we calculated the internal quantum efficiency (IQE) of control devices and the best $\text{MAPbI}_{2.9-x}\text{Br}_{0.1}\text{Cl}_x$ based on the measured reflectance and EQE (**Figure 5. 7c and d**).⁷⁰ Remarkably, the ternary halide perovskite devices exhibited approximately 100% IQE throughout the whole absorption spectrum (400~800 nm), implying that photons are converted to dissociated electron – hole pairs and extracted from the device without any recombinative losses. Not only highly crystalline domains but also a pinhole-free perovskite layer led to these outstanding IQE values by eliminating recombination sites from the devices. As we expected from UPS results, the V_{OC} of $\text{MAPbI}_{2.9-x}\text{Br}_{0.1}\text{Cl}_x$ devices increased by 0.14 V compared to control devices without Br incorporation due to a deepening of the valence band energy.

Upon further increasing the quantity of Br additive in perovskite mixture precursor, the efficiency of the corresponding devices gradually decreased. This decrease in performance of the $\text{MAPbI}_{3-y-x}\text{Br}_y\text{Cl}_x$ ($0.3 \leq y < 1$) perovskites might be attributed to a degradation of the active layer morphology and increase in band gap. J_{SC} is proportional to the product of the charge-collection efficiency and the light-harvesting efficiency; excessive Br content may decrease the J_{SC} by both of these mechanisms. The increase in bandgap with Br content results in reduced light absorption, while the increase in roughness and film defects with excessive Br content lead to poor charge collection efficiency. Also, poor coverage on the PEDOT:PSS layer allow direct contact between the HTL and ETL, which may cause V_{OC} loss. As shown in **Figure 5. 4a-d**, perovskite films with excess Br content ($0.3 \leq y$) showed poor coverage on PEDOT:PSS layers and led to direct contact with ETL which decreased device performance despite similar optical and electrical properties compared to the optimal $\text{MAPbI}_{2.9-x}\text{Br}_{0.1}\text{Cl}_x$ perovskite composition. As previously reported in the literature, methyl ammonium lead bromide (MAPbBr_3) has a relatively large band gap of 2.3 eV compared to MAPbI_3 ; thus the amount of light that is absorbed in the active layer decreases as the Br content increases with a concomitant reduction in J_{SC} . These observations are consistent with previous reports which describe a widening the band gap with increasing Br content in binary I / Br PeSCs. Although our optimized ternary halide perovskite devices ($0.3 \leq y$) did not yield a V_{OC} greater than other reports of $\text{MAPbI}_{3-x}\text{Br}_x$, absorption spectra indicate that the absorption edge is only slightly blue-shifted, allowing high J_{SC} values to be maintained in the ternary system.

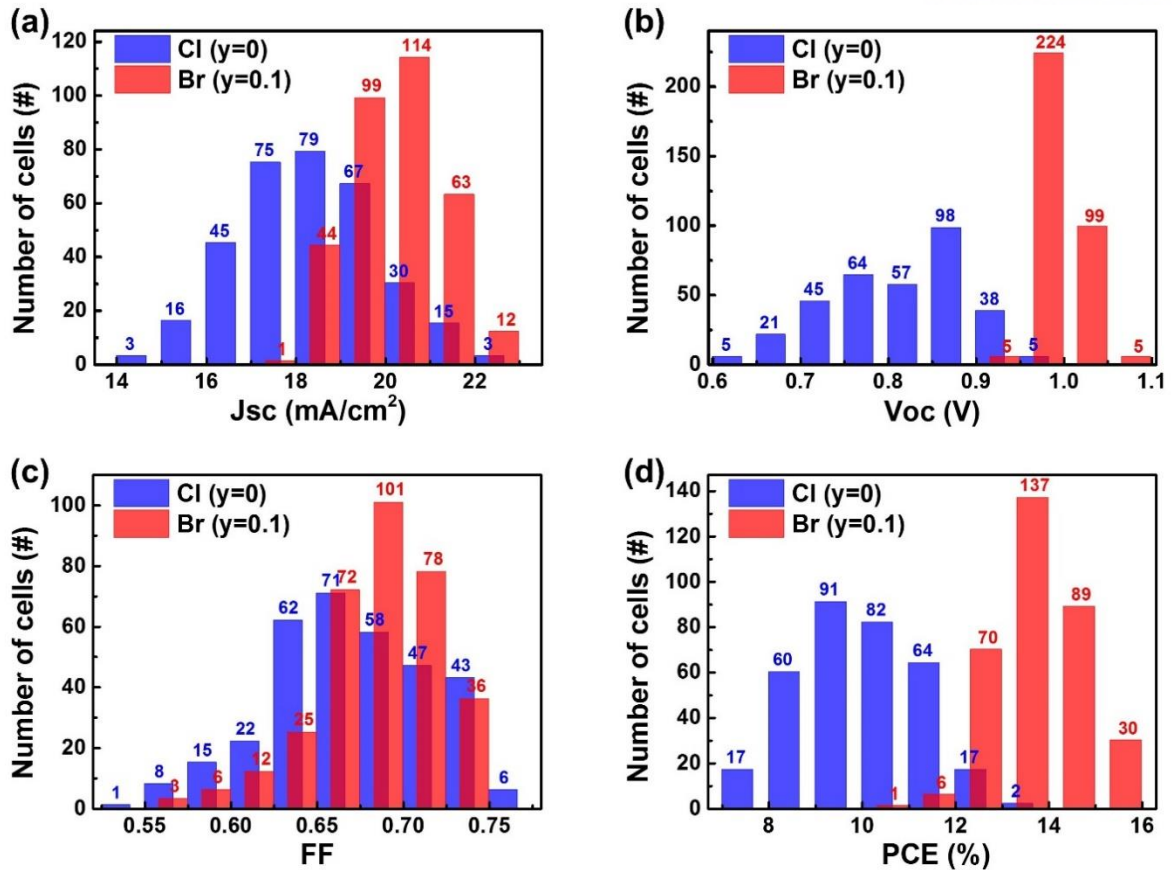


Figure 5. 9. Histogram of device statistics from a total of 333 solar cell devices comprising $\text{MAPbI}_{3-y-x}\text{Br}_y\text{Cl}_x$ ($y = 0, 0.1$) perovskite films with different Br ratios. (a) Short circuit current density, (b) open circuit voltage, (c) fill factor and (d) power conversion efficiency.

It is well-known that perovskite solar cells are subject to large variations in device performance and often poor reproducibility, therefore, a large number of devices were statistically analyzed. **Figure 5. 9a ~ d** show histograms of J_{sc} , V_{oc} , FF and PCE for 333 individual devices that were fabricated using $\text{MAPbI}_{3-x}\text{Cl}_x$ and $\text{MAPbI}_{2.9-x}\text{Br}_{0.1}\text{Cl}_x$ active layers. The average J_{sc} , V_{oc} and FF of $\text{MAPbI}_{2.9-x}\text{Br}_{0.1}\text{Cl}_x$ devices were not only higher in value but also showed a narrower distribution of values than the $\text{MAPbI}_{3-x}\text{Cl}_x$ devices. Although $\text{MAPbI}_{3-x}\text{Cl}_x$ appears to have a slightly higher extinction coefficient in **Figure 5. 2b**, the homogeneous and defect-free crystal domains of $\text{MAPbI}_{2.9-x}\text{Br}_{0.1}\text{Cl}_x$ led to higher overall J_{sc} values. In particular, the average V_{oc} of the $\text{MAPbI}_{2.9-x}\text{Br}_{0.1}\text{Cl}_x$ devices prepared using the method reported in this work exhibited an outstanding increase from 0.87 V to 1.01 V, clearly reflecting the influence of Br incorporation. Notably, the V_{oc} of $\text{MAPbI}_{2.9-x}\text{Br}_{0.1}\text{Cl}_x$ devices is very reproducible with a deviation of less than 10% compared to the $\text{MAPbI}_{3-x}\text{Cl}_x$.

5.4 Conclusion

In summary, we have successfully demonstrated a ternary halide perovskite system as a light harvester and fabricated high performance p-i-n planar heterojunction perovskite/PC₆₁BM hybrid solar cells using convenient, low-temperature solution processing techniques. We have investigated the influence of structural composition on the opto-electronic properties of the materials in order to achieve high-quality, dense perovskite films by fractional substitution of PbCl₂ with PbBr₂ in the precursor solution. Film compositions with Br content ranging from 0 to 1 in the MAPbI_{3-x}Cl_x/DMA system were investigated in order to improve morphology and surface coverage of the perovskite layer. A composition comprising 10% Br substitution in the perovskite precursor solution yielded an optimal power conversion efficiency of 16%, constituting a ~30% enhancement compared to the binary system via the formation of smooth, defect free films and a deeper valence band energy. These devices exhibit stable performance with a narrow distribution of device characteristics and negligible hysteresis. Compared to previous work using ternary halid perovskites, we were able to acheive a substantial increase in performance via the use of single, ternary halide containing precursor solution dissolved in a novel solvent (DMA), which led to improved morphology and device characterisitcs compared to the binary system. The approach reported here constitutes a significant advance in the application of ternary perovskite materials, providing a simple and effective way to prepare high performacne perovskite active layers in a one-step process. This approach has excellent promise for application in roll-to-roll produced modules as well as for deposition on flexible substrates.

CHAPTER 6. The introduction of perovskite seed layer for high performance perovskite solar

The content of this chapter is published in *J. Mater. Chem. A*, **6**, 20138 (2018)

6.1 Research background

Organic-inorganic halide perovskites have emerged as potential materials for next generation solar cells due to their own outstanding optoelectronic properties and unique physical characteristics which are originated from the long diffusion length and low carrier recombination.^{3, 4, 6, 51, 71, 72} Last 5 years, organic-inorganic halide perovskite based solar cells (PeSCs) have rapidly evolved to exhibit remarkable performance over 22.7% power conversion efficiencies (PCEs) in conventional mesoporous architecture (n-i-p structure) which is composed of bottom electrode/compact TiO₂/mesoporous TiO₂/perovskite /hole transport layer/top electrode.⁷³ However, the n-i-p structure of PeSCs need high temperature (> 400 °C) to sinter compact and mesoporous TiO₂ layer, which increases the fabrication cost of the device and restricts the flexible plastic substrates.^{3, 32, 52} Furthermore, n-i-p structure requires expensive high work function metal electrode such as Au and Pt in top electrode position. This high cost fabrication of n-i-p perovskite structure can be a concern of the commercialization market. As an alternative to these problems, inverted structure (p-i-n structure) PeSCs has extensively studied due to their several advantages such as easy fabrication, hysteresis-less, long-term stability.^{16, 34, 74, 75} In addition, p-i-n structure provides not only low temperature solution processable that offer a wide choice of the flexible substrates but also low cost of device processing for commercial application.⁷⁶ However, the PCE of p-i-n structure PeSCs is still lower than that of the n-i-p structure PeSCs because of low open circuit voltage (V_{oc}) of 1.00 V compared to 1.15 V in n-i-p structure PeSCs as certified device standard.^{77, 78}

Several attempts have been tried for fabricating perovskite active layer to make a homogenous crystalline, high dense and full surface coverage perovskite film.⁷⁹ Although the mechanism of perovskite layer forming is not clear, attempts have been made to achieve the homogeneous film and pinhole-free perovskite layer.⁸⁰⁻⁸³ As the results of these efforts, many methods likewise solvent engineering, intermolecular exchange, solvent vapor-annealing and additive-assisted deposition have been developed to achieve the high quality perovskite film by controlling the perovskite grain boundary and crystalline growth behavior.^{7, 8, 52, 84} Although, these methods are excellent guideline for high quality film, there have been some shortcomings for each other. For example, solvent engineering method

requires the consistent location of the dropping the anti-solvent on the perovskite film which makes the partially ununiform crystal grains on the whole perovskite film, which leads to cause poor device reproducibility and adverse for large-scale production.⁸⁵

To achieve high quality perovskite film, we demonstrated, for the first time, to employ the easy and effective process for high efficiency p-i-n planar structure of PeSCs by handling the compact seed perovskite layer (CSPL). The compact seed layer induces the assisting vertical growth of perovskite crystal domains as well as improving adhesion between hole transport layer (HTL) and perovskite active layer, which leads to increase optoelectronic properties of perovskite film. The solar cells architecture is comprised PTAA/perovskite seed layer: perovskite /Phenyl-C61-butyric acid methyl ester (PC₆₁BM) /Al layers on top of indium tin oxide (ITO) substrates. With our new device architecture, we achieved record V_{OC} of 1.16 V and PCEs of 19.24% using pure crystal perovskite with negligible hysteresis while retaining high V_{OC} and fill factor (FF) value.

6.2 Experimental details

Materials preparation

A Poly[bis(4-phenyl)(2,4,6-trimethylphenyl)amine] (PTAA) and F₄-TCNQ were purchased from Jilin OLED. Anhydrous *N*-Methyl-2-pyrrolidone (NMP), anhydrous Dimethyl sulfoxide (DMSO), 2-Propanol (IPA) and anhydrous *N,N*-dimethylformamide (DMF) were purchased from Sigma-Aldrich and were used without purification. Lead Iodide (PbI₂, 99.999%) were purchased from Alfa Aesar. Methylammonium iodide (MAI) was reported previous literature. Formamidinium acetate, Hydriodic acid (57% in water with a stabilizer), hydrobromic acid (48% in water), and methylamine (40% in methanol) were purchased from Sigma-Aldrich, Fluka, and TCI. Formamidinium iodide (FAI) was synthesized as reported elsewhere. Briefly, 15 g of formamide acetate was reacted with 30 mL of hydriodic acid in a 100 mL round-bottomed flask at 0 °C for 1 h with stirring. Methylamine bromide (MABr) was also synthesized by combining 27.86 mL of methylamine and 44 mL of hydriodic acid in a 250 mL round-bottomed flask at 0 °C for 2 h with stirring. From the solution, a light yellow colored precipitate was obtained by evaporating the solutions at 70 °C for 1 h. The resulting products were dissolved in ethanol and precipitated using diethyl ether. This procedure was repeated until white powders were obtained, and then recrystallized from ethanol and diethyl ether with slow gas diffusion over the 3 days. After recrystallization, the resulting powders were collected and dried at 60 °C for 24 h. The other organic cations were purchased from Dyesol and lead salts were bought from TCI. Spiro-OMeTAD and FK209 were purchased from EM-Index.

Solar Cell Fabrication and Characterization

p-i-n structure: 10 mg PTAA was dissolved in 1 ml di-methylchlorobenzene (DCB) with 1wt% of F₄-TCNQ and stirred at 60 °C for overnight. To prepare perovskite precursor solutions, 1.3 mM of PbI₂ was dissolved in 1ml DMF and MAI precursor was varied from 50 mg/ ml to 65mg/ ml in IPA. The obtained solution was stirred at room temperature for 30 min. ITO-coated glass substrates were cleaned by ultra-sonication in deionized water, acetone and isopropyl alcohol for 10 min each. PTAA layer was deposited on cleaned ITO substrates by spin-casting at 4000 rpm for 30s, followed by annealing at 140 °C for 10 min. For without CSPL devices, MAI precursor solutions were spin-cast at 3000 rpm for 30s and PbI₂ were spin-coated at 5000 rpm for 30s. The films were dried on a hot-plate at 100 °C for 2 min in air atmosphere. For with CSPL devices, previous two step method performed twice. On top of the perovskite layer, a 25 mg/ml solution of PC₆₁BM in 1:1 mixture of chlorobenzene and chloroform was spin-cast at 1500 rpm. Subsequently, an Al electrode with a thickness of 100 nm was deposited on the PC₆₁BM layer under vacuum (<10⁻⁶ Torr) by thermal evaporation.

n-i-p structure: 10 mm-patterned FTO glass (Pilkington, TEC-8, 8 Ωsq⁻¹) was washed with 10 % of

Deconex solution and cleaned with deionized water, acetone, ethanol, and isopropyl alcohol for 10 min each in an ultrasonic bath, before being exposed to a UVO cleaner for 15 min. An electron transfer layer (ETL) of TiO₂ was deposited on the cleaned FTO substrates using air spray pyrolysis. 20 mM titanium diisopropoxide bis(acetylacetonate) in an ethanol solution was coated on the FTO glass at 450 °C for 10 min and sintered at 450 °C for 1 h and slowly cooled to ambient temperature. This procedure gives a blocking layer of anatase TiO₂ with a thickness of around 50-60 nm. Prior to perovskite deposition, the substrates were exposed on a UVO cleaner for 15 min. The perovskite precursor solutions were prepared by mixing FAI (1.2M), PbI₂ (1.32M), MABr (0.18M) and PbBr₂ (0.18M) in anhydrous DMF:DMSO = 4:1 (v:v). For without CSPL devices, the perovskite precursor solution was spin coated in a two-step method at 2000 rpm for 5 s followed by 6000 rpm for 20 s. During the second step, 1M of toluene was poured onto the spinning substrate slowly prior to the end of the procedure. The substrates were then annealed at 400 °C for 4 s, respectively. For with CSPL devices, previous two step method performed twice. After perovskite film annealing, the substrates were cooled down for 10 minute and a hole transfer layer was spin coated at 4000 rpm for 10 s. A Spiro-OMeTAD (EM index) in chlorobenzene (70 mM) was mixed with 7.5 μL of a 4-tert-butylpyridine (TBP) additive and 7.5 μL of a Li-bis(trifluoromethanesulfonyl) imide (Li-TFSI) solution (170 mg/1 mL acetonitrile) before adding suitable tris(2-(1h-pyrazol-1-yl)-4-tert-butylpyridine)-cobalt(III) tris(bis(trifluoromethylsulfonyl) imide) (FK209, Dyesol). Finally, an Au counter electrode (70 nm) was deposited by thermal evaporation under high vacuum.

Device characterization

Scanning electron microscope measurements (SEM) were performed using an S-4800 Hitachi high-Technology microscope. SEM samples were prepared by coating perovskite precursor solutions onto glass substrates by spin-coating. For X-ray diffraction (XRD) measurements, perovskite films were coated on PTAA-coated glass substrates and diffractograms were collected using a Bruker, D8 ADVANCE diffractometer at a scan rate of 2.4° min⁻¹. UV-vis absorption was measured using a Varian Cary 5000 spectrophotometer. AFM images were obtained using a Veeco Multimode AFM microscope in a tapping mode. The current density-voltage (J-V) characteristics of the solar cells were measured using a Keithley 2635A Source Measure Unit. Solar cell performance was carried out under illumination by an Air Mass 1.5 Global (AM 1.5 G) solar simulator with an irradiation intensity of 100 mW cm⁻². Apertures (13.0 mm²) made of thin metal were attached to each cell before measurement for J-V characteristics. External quantum efficiency (EQE) measurements were obtained with a PV measurements QE system under ambient conditions, with monochromated light from a xenon arc lamp. The monochromatic light intensity was calibrated with a Si photodiode and chopped at 100 Hz.

6.3 Results and discussion

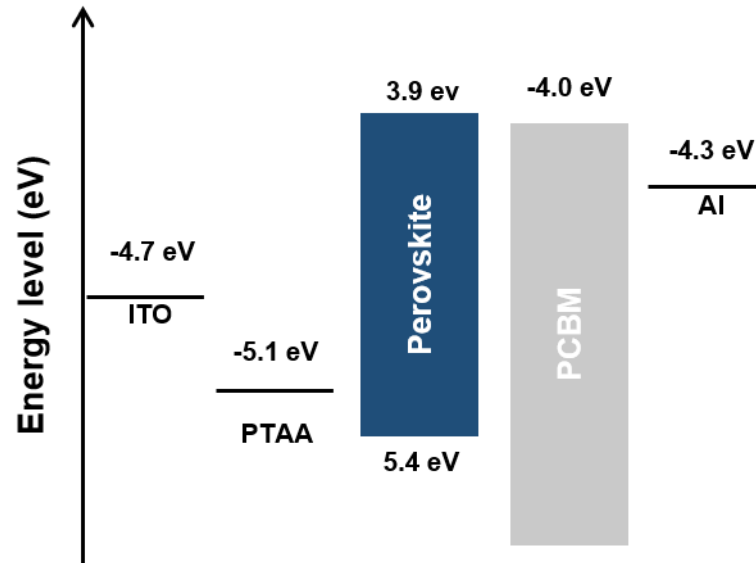


Figure 6. 1. Energy band diagram of perovskite solar cells.

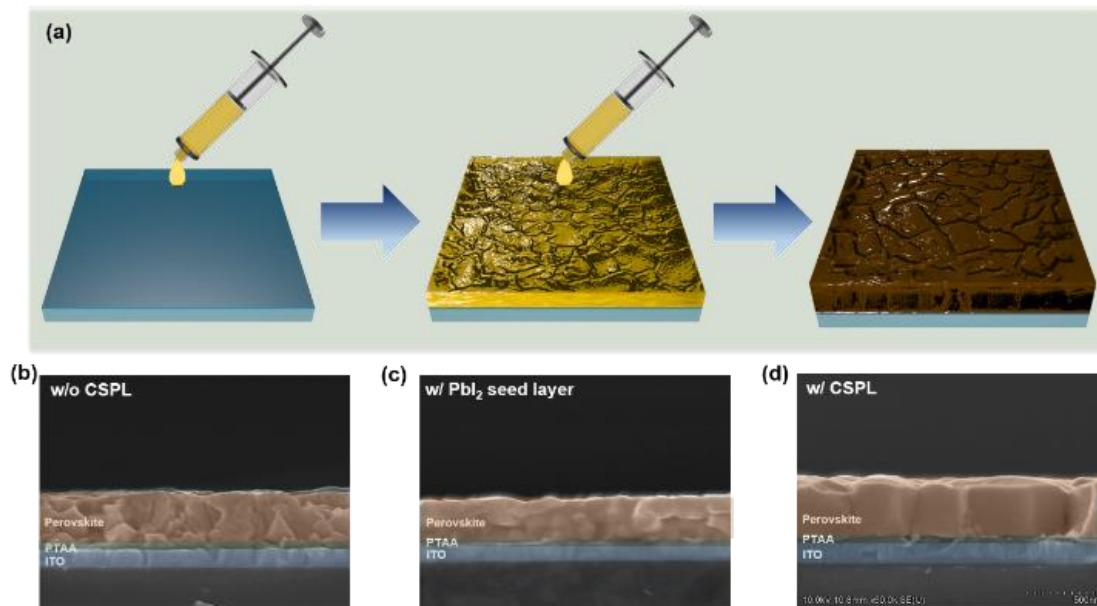


Figure 6. 2. (a) Schematic process of perovskite fabrication, first compact seed perovskite layer (CSPL) deposition on PTAA substrate then perovskite photoactive layer coated on CSPL and cross-sectional SEM image of perovskite film (b) without CSPL, (c) with PbI₂ seed layer and (d) with CSPL.

To examine the influence of seed layer on crystallization of perovskite film growth, cross-sectional scanning electron microscopy (SEM) images of whole perovskite layers were collected. **Figure 6. 1** and **Figure 6. 2** shows energy band diagram of PeSCs and the photoactive perovskite film cross-sectional SEM images respectively without seed layer (**Figure 6. 2b**), with PbI₂ seed layer (**Figure 6.**

2c) and with CSPL (Figure 6. 2d) which were deposited on PTAA substrate by spin-coating respectively. After then photoactive perovskite layer was coated on each layer once more and annealed for 2 mins at 100 °C. The difference of cross-sectional SEM images in Figure 6. 2b ~ d directly indicates the perovskite film quality with seed layer which demonstrated vertically well-grown high quality perovskite crystal film with high dense, highly uniform crystallinity and, large grain size compared to without seed layer and PbI_2 seed layer. Cross-sectional SEM images directly displays the perovskite seed layer that can be a nucleation point to make a high crystalline perovskite film. The constructed homogeneous perovskite crystal film increases the optical and electrical property which also leads to reduce charge recombination and increases charge carrier diffusion length.^{4, 14}

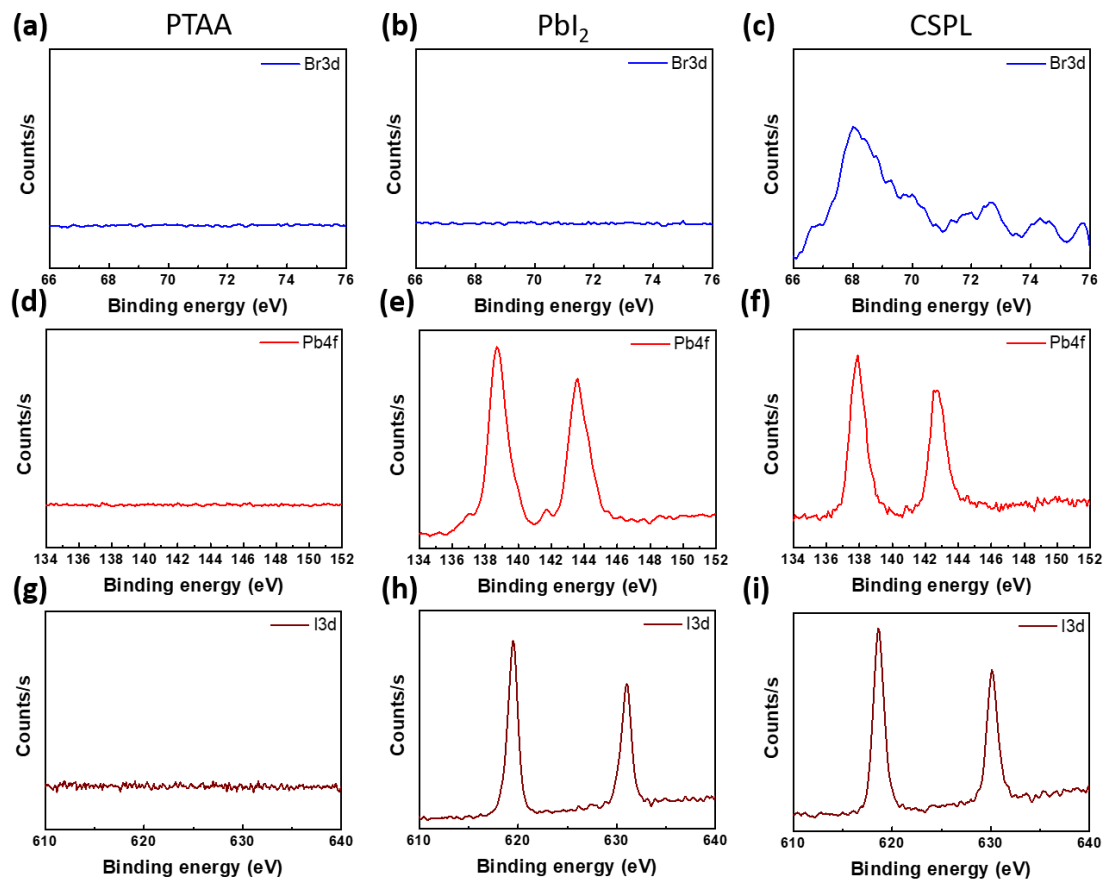


Figure 6. 3. XPS result of PTAA control substrate, PbI_2 seed layer and CSPL films respectively in height direction, after washed by DMF solvent, in width direction, (a)~(c) Br3d, (d)~(f) Pb4f and (g)~(i) I3d peak position.

To clarify the presence of the seed layer after washing by DMF perovskite solvent, X-ray photoelectron spectroscopy (XPS) was measured since photoactive perovskite layer was also coated on CSPL with the same dissolved solvent. On the PTAA (control) substrate, PbI_2 seed layer, and $\text{MAPbBr}_x\text{I}_{3-x}$ perovskite seed layer was deposited respectively. All substrates were washed by DMF solvent. We carefully measured XPS with certain peak positions Pb4f, I3d, and Br3d to see the presence of each atom after washing the first deposited films. The survey of XPS measurement of PTAA control

substrate, PbI_2 seed layer and CSPL films were shown in **Figure 6. 3a ~ i** and **Figure 6. 4** clearly show the certain peak positions Br3d peak around 66 ~ 70 eV, Pb4f peak around 137 ~ 145 eV, and I3d peak around 615 ~ 635 eV. Control PTAA substrate does not show the any peaks at each position, but PbI_2 seed layer has strong Pb4f peaks at 137.9 eV and 142.7 eV and I3d peaks at 630.1 eV and 618.6 eV only.^{86, 87} And, MAPbBrI_{3-x} perovskite seed layer has all three Pb4f, I3d and, Br3d peak position. XPS data directly show that after washing by DMF solvent, thin layer of $\text{MAPbBr}_{x-1}\text{I}_3$ perovskite is still on the substrate which can be a nucleation point to make perfect perovskite crystal.

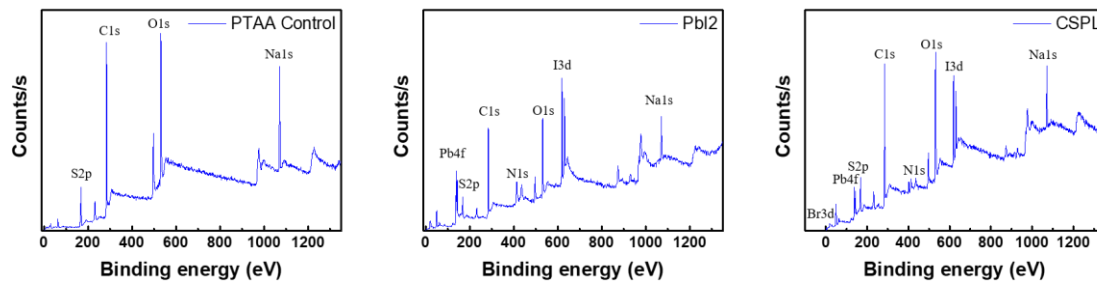


Figure 6. 4. XPS survey spectrum of PTAA control, PbI_2 seed layer and CSPL films after washing by DMF solvent.

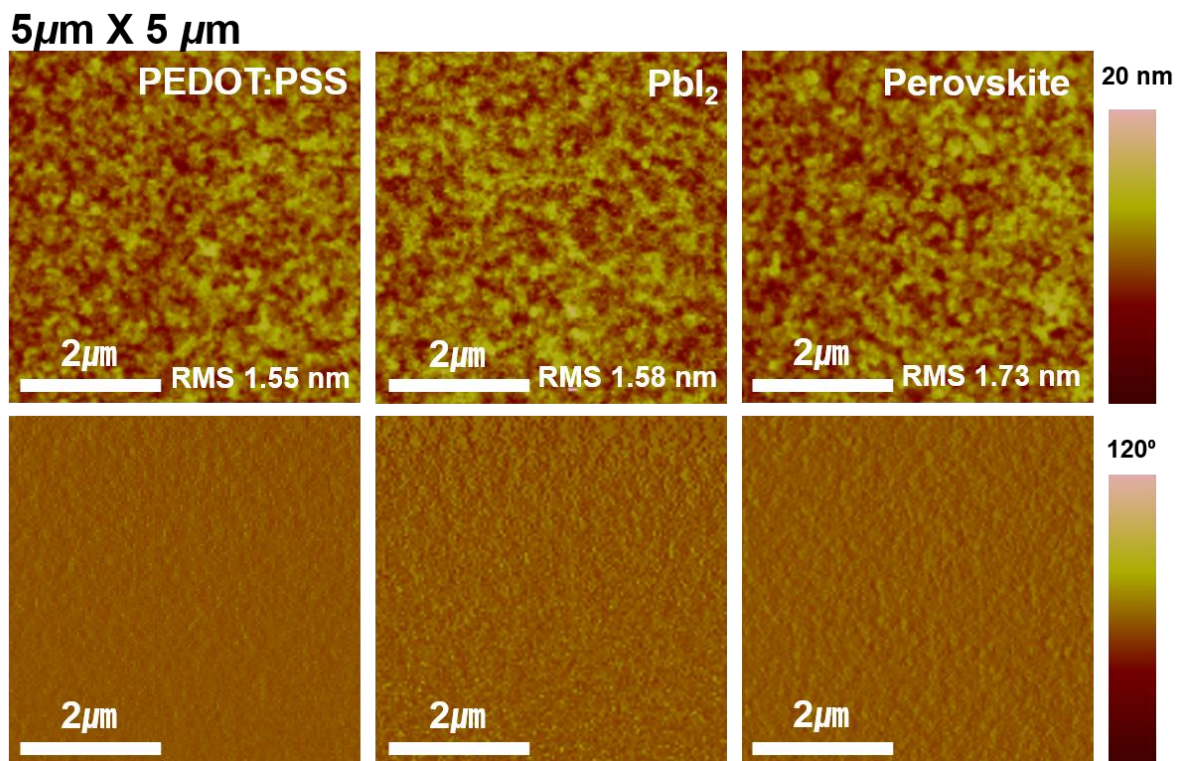


Figure 6. 5. Atomic force microscope (AFM) surface image of PEDOT control substrate, PbI_2 , CSPL films respectively, after washed by DMF solvent.

To see the reflective intensity of the seed layer, the packing characteristics were collected by 2D-Grazing-Incidence Wide-Angle X-ray Scattering (2D-GIWAXS). Photo active perovskite layer (**Figure 6. 6a**), PbI_2 seed layer (**Figure 6. 6b**) and, perovskite seed layer (**Figure 6. 6c**) of 2D-GIWAXS images and corresponding in-plane (**Figure 6. 6d**) and out-of-plane (**Figure 6. 6e**) line-cut profiles are displayed respectively. From XPS measurement, the presence of the seed layer was confirmed even after washing by DMF solvent. From 2D-GIWAXS, crystal orientation of the perovskite or seed layer with the intensity of strong and distinct diffraction rings were obtained at $q_z \approx 10, 20, 22,4 \text{ \AA}^{-1}$, corresponding to the (110), (220) and (310) crystal planes which indicates that textured perovskite crystal with an orthorhombic crystal structure (**Figure 6. 6a**).^{88, 89} The bright and strong peaks in the images suggest that the film possess good crystallization and large grain size, which obviously contributed to the improved performance of PeSCs. 2D-GIWAXS patterns of perovskite seed layer has similar peak position and shape compared with control perovskite film at (110), (220) and (310). These results support that the thin seed perovskite layer perfectly constructs the perovskite crystal. The XPS and 2D-GIWAXS results are direct evidence that after washing the first perovskite layer (seed layer), very strong crystal structure of perovskite was constructed to influence on forming a good quality of second main perovskite layer.

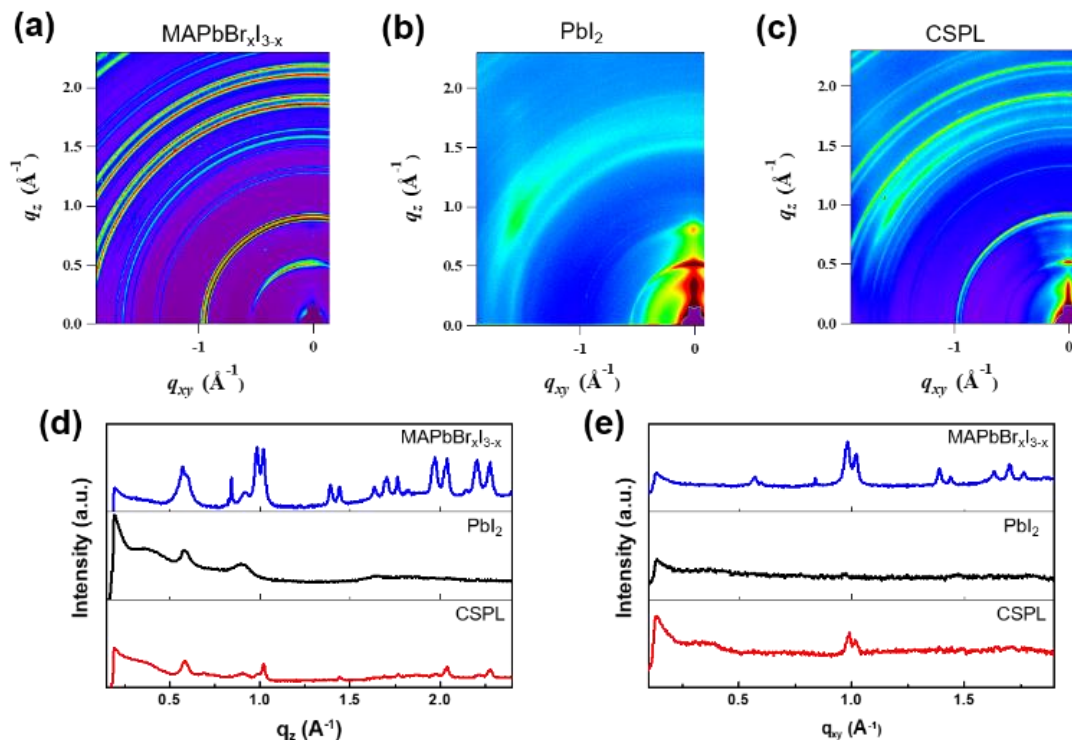


Figure 6. 6. Two-dimensional grazing incidence wide angle X-ray scattering (2D-GIWAXS) images on the substrates after washed by DMF solvent (a) $\text{MAPbBr}_x\text{I}_{3-x}$, (b) PbI_2 and (c) CPSL film. 2D-GIWAXS patterns corresponding line-cuts in (d) in-plane and (e) out of-plane directions of $\text{MAPbBr}_x\text{I}_{3-x}$, PbI_2 , and CPSL film respectively.

In order to develop a deeper understanding of the charge recombination characteristics of the devices, the incident-light-intensity-dependent J_{SC} in **Figure 6. 7a** and V_{OC} in **Figure 6. 7b** characteristics were measured under short-circuit conditions. **Figure 6. 7a** shows a log-log plot of J_{SC} as a function of the light intensity. The power-law dependence of J_{SC} on light intensity was fitted using the following equation.

$$J_{SC} \propto I^\alpha \quad (\text{Eq. 6-1})$$

where I is the intensity of incident light and α is an exponent constant for PeSCs devices (generally 0.85 – 1). The α value was calculated to be 0.963 for without seed layer device, suggesting significant charge recombination under short-circuit condition. These results can be interpreted that interfacial engineering by seed layer eliminated the energy barrier which leads to charge recombination at the interfaces between perovskite layer and charge transport layer. **Figure 6. 7b** shows a semilogarithmic plot of V_{OC} as a function of the light intensity. The V_{OC} of conventional p-n junction based model is as follows:^{90, 91}

$$V_{OC} = \frac{E_{gap}}{q} - \frac{kT}{q} \ln \left(\frac{(1-p)\gamma N_c^2}{PG} \right) \quad (\text{Eq. 6-2})$$

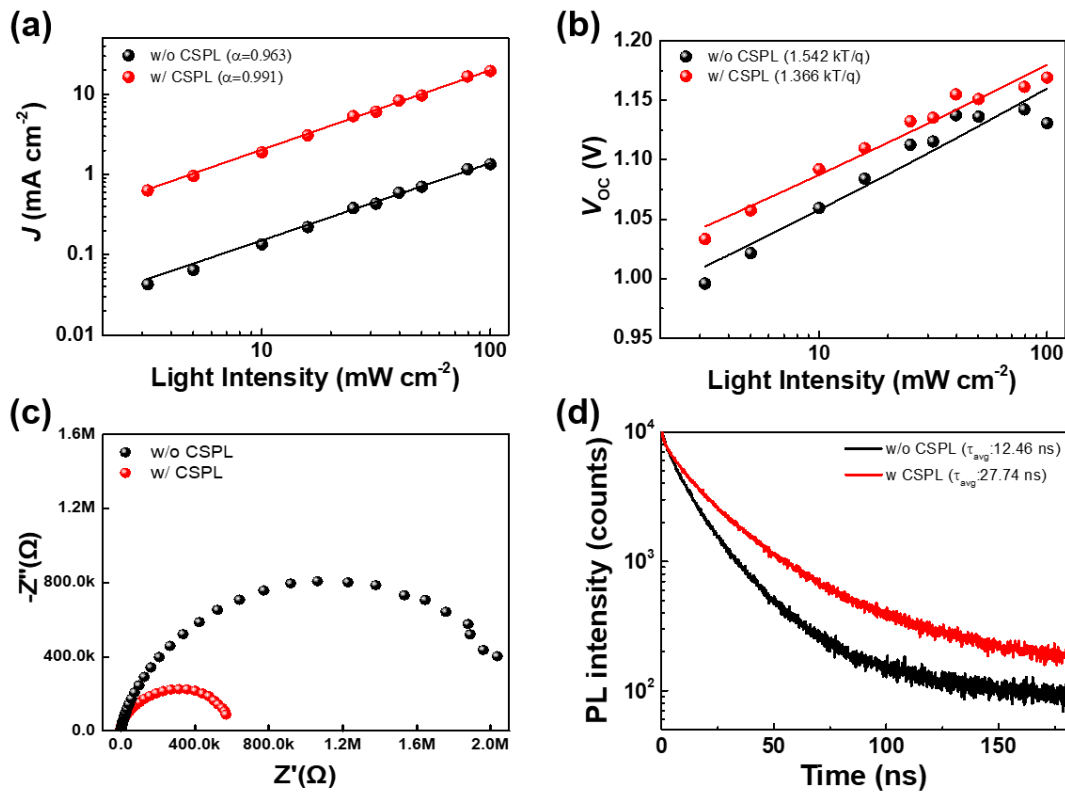


Figure 6. 7. Charge recombination and transport characteristics: light intensity dependence of (a) J_{sc} (b) V_{oc} of perovskite device and (c) impedance spectroscopy and (d) Time correlated single photon counting (TCSPC) of perovskite film without and with CSPL.

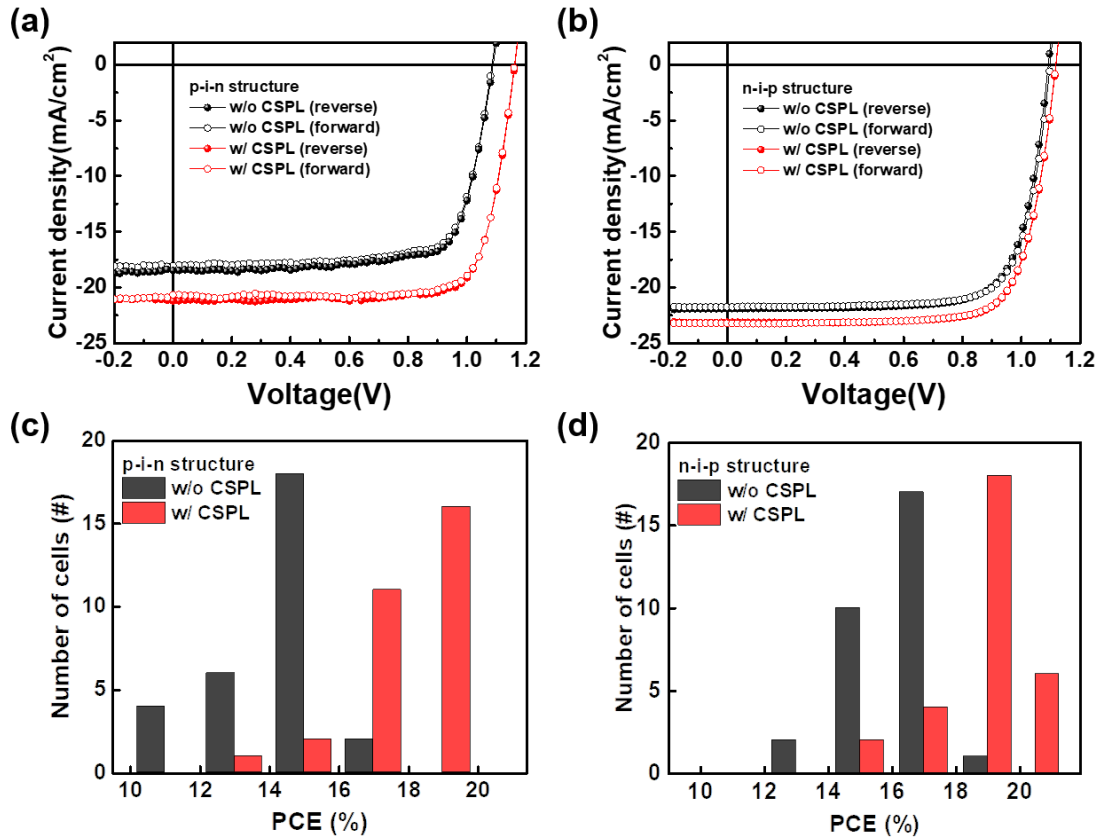


Figure 6. 8. J-V characteristics of perovskite solar cells without and with CSPL including forward and reverse scan direction of (a) p-i-n structure and (b) n-i-p structure. And PCE histogram of (c) p-i-n structure and (d) n-i-p structure devices statistics from a total of 30 solar cell devices respectively comprising without and with CSPL.

Table 6. 1. Solar cell characteristics of p-i-n and n-i-p structure perovskite solar cells without and with CSPL in forward and reverse scan directions.

Device type	CSPL	Scan direction	$J_{sc}(mAcm^{-2})$	$V_{oc}(V)$	FF	$PCE(\%)$
p-i-n	X	Reverse	18.47	1.09	0.75	15.07
		Forward	18.07	1.09	0.75	14.73
	O	Reverse	21.21	1.16	0.78	19.24
		Forward	20.67	1.16	0.79	19.05
n-i-p	X	Reverse	21.86	1.11	0.76	18.32
		Forward	21.77	1.10	0.76	18.22
	O	Reverse	23.06	1.13	0.78	20.37
		Forward	23.15	1.13	0.77	20.08

where, E_{gap} is the band gap of the semiconductor; in this case, the energy difference between highest occupied molecular orbital of PTAA and PCBM conduction band edge, q is the elementary charge, k is the Boltzmann constant, T is temperature, P is the dissociation probability of the bound electron—hole pairs, γ is the Langevin recombination constant, N_C is effective density of states, and G is generation rate of bound electron—hole pairs.

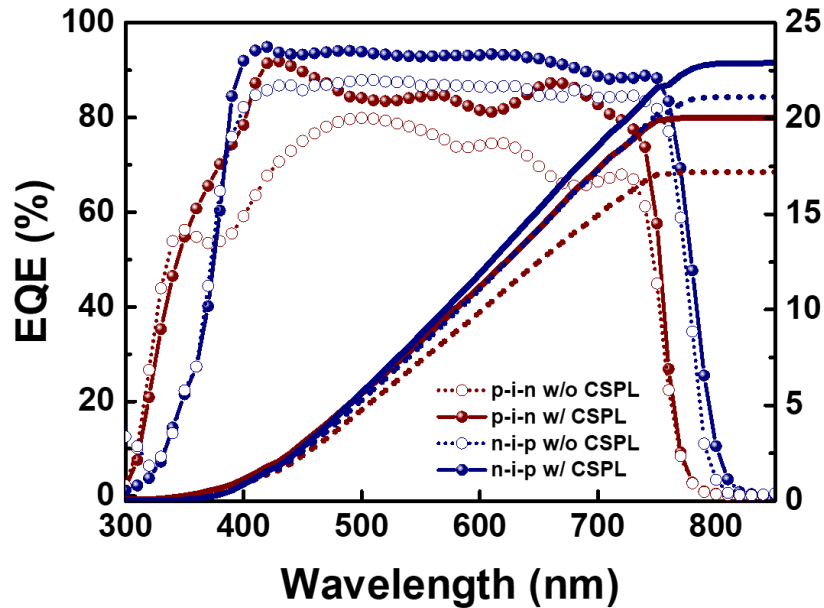


Figure 6. 9. EQE and calculated J_{sc} of p-i-n structure and n-i-p structure of CSPL perovskite solar cells. (p-i-n w/o CSPL: $17.25 J_{\text{sc}}(\text{mAcm}^{-2})$, p-i-n w/ CSPL: $20.05 J_{\text{sc}}(\text{mAcm}^{-2})$, n-i-p w/o CSPL: $21.13 J_{\text{sc}}(\text{mAcm}^{-2})$, n-i-p w/ CSPL: $22.90 J_{\text{sc}}(\text{mAcm}^{-2})$).

If the shockley—Read—Hall (SRH) recombination is involved, a stronger dependence of V_{OC} on the light intensity with a slope greater than kT/q will be obtained. The semilogarithmic plots of V_{OC} against light intensity give slopes of $1.324 kT/q$ and $1.542 kT/q$ respectively. The V_{OC} for without seed layer device decreases faster than for the with seed layer device as the light intensity is reduced, indicating significant SRH recombination involved under open-circuit condition. Impedance spectroscopy was also performed to support the results of light intensity in seed layer perovskite film on electrical characteristics. As **Figure 6. 7c** shown, both with and without seed layer devices were obtained semicircle in the range of 100 Hz to 2 MHz. Smaller semi circuit of the device with seed layer indicates the reduction in the charge transfer resistance due to high crystalline film.⁹² Time correlated single photon counting (TCSPC) luminescence decay of with and without CSPL was described in **Figure 6. 7d**. We prepared samples with configuration of glass/perovskite and glass/CSPL:perovskite, where thick perovskite film (thickness: 460 ± 20 nm) was used for optimum device performance. The average PL decay time (τ_{avg}) was obtained of 12.46 ns for glass/perovskite, and 27.74 ns for

glass/CSPL:perovskite respectively. Comparing the PL decay with and without CSPL devices, the lifetime with CSPL film has about 2 times higher than without CSPL film which directly ensures the formed high quality film. The optically intrinsic longer PL lifetime can be attributed to the achieving high performance photovoltaic device because the generated carrier can be easily diffused to each layer and then collected to each electrode as reported previously.⁴

Table 6. 2. Solar cells characteristic of p-i-n structure perovskite devices without and with and without CSPL based on PEDOT:PSS HTL.

	J_{sc} (mA cm ⁻²)	V_{oc} (V)	FF	PCE (%)
w/o S.L.	18.39	0.93	0.75	12.81
w/ S.L.	20.09	1.00	0.79	16.25

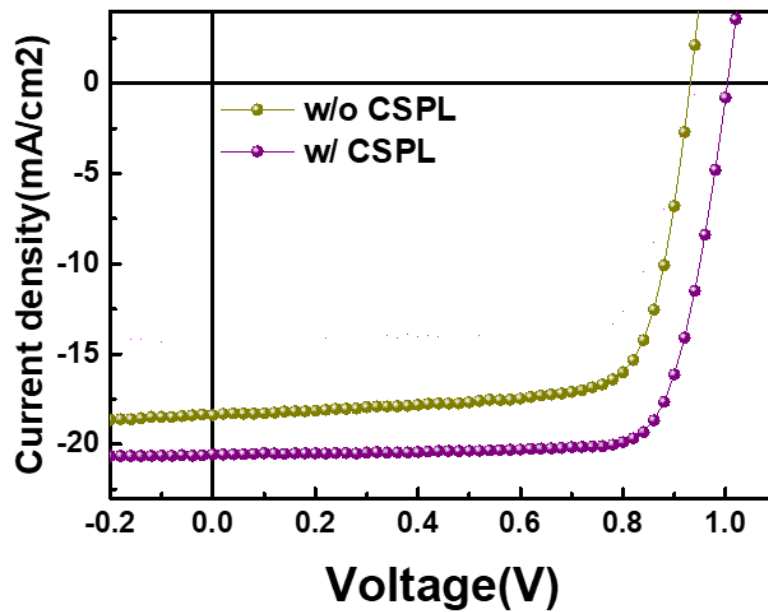


Figure 6. 10. Characteristics of perovskite solar cells without and with CSPL based on PEDOT:PSS HTL.

The current density-voltage (J-V) characteristics for p-i-n and n-i-p structure perovskite devices with or without seed perovskite layer are summarized in **Table 6. 1** while the relevant data are plotted in **Figure 6. 8**. The p-i-n structure perovskite solar cells were prepared with the architecture ITO/PTAA/CSPL: MAPbBr_xI_{3-x}/PC₆₁BM/Al. The thickness of the PC₆₁BM was varied to not only cover whole perovskite photoactive layer which the photogenerated carriers can be effectively transported by PC₆₁BM interfacial layer but also prevent direct contact between perovskite layer and Al electrode. The p-i-n perovskite devices without seed layer exhibited a short-circuit current density (J_{sc}) of 18.47 mA cm⁻², V_{oc} of 1.09 V, fill factor (FF) of 0.75% and overall PCE of 15.07%, while p-i-n perovskite devices

with seed layer achieved excellent PCEs including a J_{SC} of 21.21 mA cm^{-2} , V_{OC} of 1.16 V , FF of 78% and PCE of 19.25% due to high dense and vertical growth bulk like perovskite crystalline film. Notably, V_{OC} is remarkably increased about 0.07 V which is one of the highest V_{OC} value in p-i-n structure perovskite solar cells with pure crystal perovskite film. The increased V_{OC} is majorly related to the leakage current in the device. As clearly checked the reduced charge recombination from Shockley—Read—Hall (SRH) recombination and PL decay, seed layer has crucial impact on the forming high quality perovskite film to achieve the device performance improvement. In the forward scan direction, in addition, the perovskite devices were achieved PCE of 19.05% with a J_{SC} of 20.67 mA cm^{-2} , a V_{OC} of 1.16 V and a FF of 79% . The device has a negligible photocurrent hysteresis and fixed high V_{OC} value attributed to reducing trap states at the grain boundaries as shown in **Figure 6. 8a and b**.

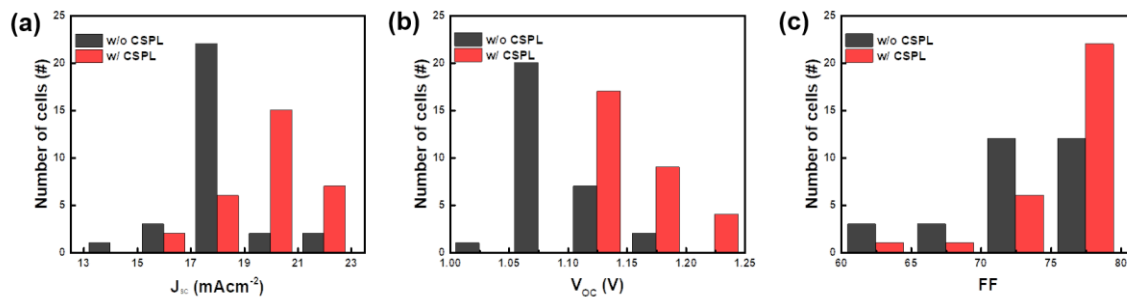


Figure 6. 11. Histogram of device statistics from a total of 30 p-i-n structure solar cell devices (ITO/PTAA/seed layer/MAPbBr_xI_{3-x}/PC61BM/Al) comprising without and with CSPL. (a) Short circuit current density, (b) open circuit voltage, (c) fill factor.

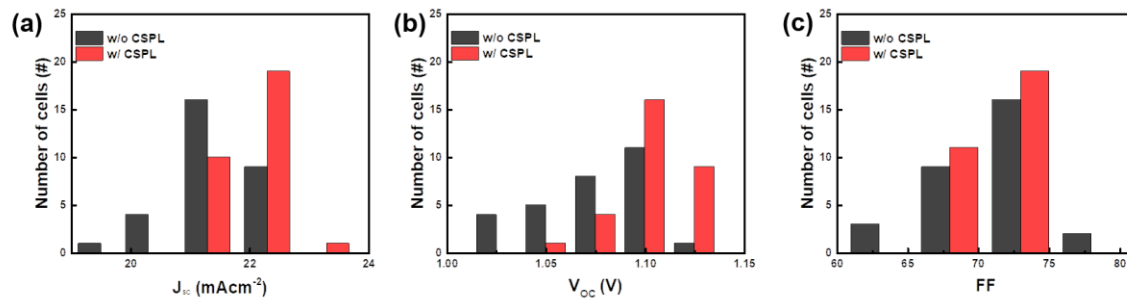


Figure 6. 12. Histogram of n-i-p device statistics from a total of 30 solar cell devices (FTO/bl-TiO₂/Mesoporous TiO₂+Perovskite((FAPbI₃)_{0.85}(MAPbBr₃)_{0.15})/Spiro-MeOTAD/Au) comprising without and with CSPL. (a) Short circuit current density, (b) open circuit voltage, (c) fill factor.

An external quantum efficiency (EQE) of the perovskite devices with seed layer shows broad spectral response in the range of $300\text{-}780 \text{ nm}$ with peak of 91.8% at wavelength of 430 nm which is the highest EQE value at blue region and calculated current density is 20.05 mA cm^{-2} , as shown in **Figure 6. 9**. The integrated photocurrent from EQE shows only 3% mismatch with obtained value from J-V curve that

implies well agreement and substantiates the observed JSC. Additionally, PEDOT:PSS was employed as HTL which is well known materials for p-i-n architecture to determine the effect of seed perovskite layer on other interfaces. As shown in **Figure 6. 10** and **Table 6. 2**, the perovskite devices with seed layer shows good performance including a J_{SC} , V_{OC} , FF and PCE of 20.09 mA cm⁻², 1.00 V, 0.79 FF and 16.25 % compared to perovskite devices without seed layer yield poor PCEs including J_{SC} of 18.39 mA cm⁻², V_{OC} of 0.93 V, FF of 75 % and PCE of only 12.81 % which directly shows that CSPL structure has the effect on the various HTL. To confirm the effect of CSPL in n-i-p structure PeSCs, n-i-p structure PeSCs was fabricated as following architecture FTO/bl-TiO₂/Mesoporous TiO₂:Perovskite ((FAPbI₃)_{0.85}(MAPbBr₃)_{0.15})/Spiro-OMeTAD/Au. The device performance was reached 20.37% with CSPL compared to with put CSPL 18.50% as shown in **Figure 6. 7b**. To directly compare the seed layer effect on the solar cells, the histograms of PCE, for p-i-n structure device **Figure 6. 7c**, n-i-p structure device for **Figure 6. 7d** and, J_{SC} , V_{OC} , and FF for p-i-n structure device **Figure 6. 10**, n-i-p structure device for **Figure 6. 11** for 30 individual devices that were fabricated using with and without seed layer. The average PCE with perovskite seed layer was not only higher in value but also showed a narrower distribution of values than the without seed layer devices in both p-i-n and n-i-p structure devices.

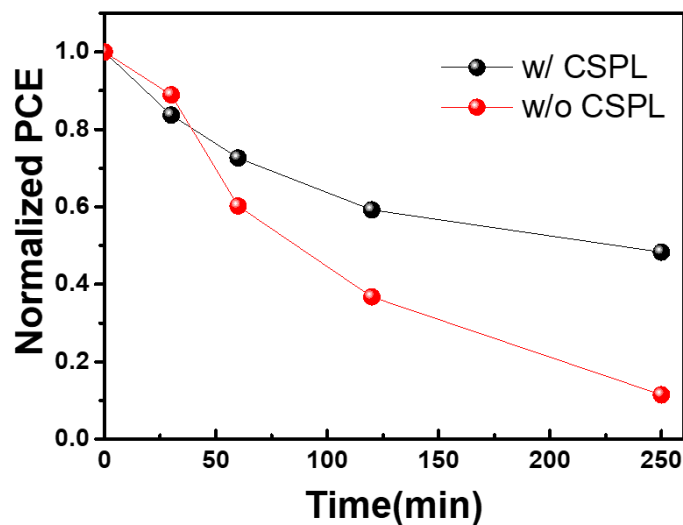


Figure 6. 13. Stability test was performed for non-encapsulated cells (with and without CSPL PeSCs) under an air about 40% humidity condition.

Especially, p-i-n structure devices with perovskite seed layer exhibited higher VOC value from 1.1 to 1.2 with high reproducibility with maintained JSC and FF. With the simple device structure (ITO/HTL/perovskite/PCBM/Al), we achieved high average PCEs with CSPL which is comparable to or higher than those of complexed p-i-n perovskite structure performance using multiple ETL and HTL such as C60 and BCP reported in the previous studies.^{85, 93} We expect that our new CSPL device

structure has potential and can be widely applied to perovskites field. We tested the solar cells stability with and without CSPL under an air about 40% humidity condition as shown in **Figure 13**. For the device with CSPL, 50% of the initial PCE was retained after 250 mins, whereas devices without CSPL was rapidly decreased less than 10% of the initial PCE after 250 mins. This result indicates that the device CSPL improves stability of the devices due to high quality perovskite crystalline structure.

6.4 Conclusion

In summary, we developed simple and effective way to fabricate high performance p-i-n planar heterojunction perovskite/PC₆₁BM hybrid solar cells by controlling the seed perovskite layer with low-temperature solution processing techniques. Seed perovskite layer has an enormous influence on vertical growth of perovskite crystal grains and adhesion between HTL and perovskite photoactive layer, leading to improve opto-electric properties of materials and overcome the problem of having lower open circuit voltage in inverted structure PeSCs. The PCE was achieved 19.25% in the p-i-n structure PeSCs with record open circuit voltage of 1.16 V and 20.37% of PCE in n-i-p structure devices with pure crystal perovskite film. The approach reported in this study constitutes a significant advance in the application of perovskite film formation, providing a easy and way to prepare high performance perovskite active layers in a both p-i-n and n-i-p architecture system. Also, this low temperature processing for high performance can apply to the application in roll-to-roll produced modules as well as for deposition on flexible substrates.

CHAPTER 7. Ultrathin, Lightweight and Flexible Perovskite Solar Cells with an Excellent Power-Per-Weight Performance

The content of this chapter is in preparation for the publication in a journal.

7.1 Research background

With the recent development in the field of energy harvesting devices, flexible and wearable photovoltaic devices have attracted a significant amount of attention as portable and wearable power sources in applications such as smart windows, wearable personal electronic devices, and wearable textiles.⁹⁴⁻⁹⁶ In particular, lightweight and ultrathin solar cells can minimize energy consumption by increasing the power-per-weight, which provides primary benefits for future power sources in specific applications, such as miniaturized drones or blimps, aerospace electronics, and weather balloons.⁹⁴ To increase the power-per-weight, researchers have developed various lightweight solar cells based on silicon, organic, and perovskite solar cell (PSC) technologies.^{94, 97-100} Among these, PSCs, which feature solution processability and high light absorption coefficient, are considered a promising flexible and lightweight power source; both the device efficiency and stability of PSCs have progressed rapidly.^{3, 6, 72} The development of planar-heterojunction perovskite materials enables the construction of flexible PSCs on polymer substrates because PSCs are compatible with low-temperature solution processing.^{101, 102} In addition, the high absorption coefficient of the perovskite material enables the active layer of the device to be very thin (less than 1 μm), resulting in a PSC with high flexibility.¹⁰³ Recently, Martin et al. reported a high power-per-weight of $\sim 23 \text{ W}\cdot\text{g}^{-1}$ for flexible PSCs fabricated on ultrathin polymer foils, which introduces the possibility of lightweight PSC devices.⁹⁴

During the fabrication of such lightweight PSCs, the device integration with flexible transparent electrodes is a critical factor that should be carefully considered to ensure proper device performance and mechanical stability for flexible PSCs. Therefore, the realization of lightweight and flexible PSCs requires the fabrication of flexible transparent electrodes with high conductivity and excellent mechanical robustness as replacements for the conventional indium tin oxide (ITO) electrodes, whose brittle nature has limited their use in flexible applications.^{104, 105} Till date, several approaches for the fabrication of high-performance flexible PSCs using various alternatives to ITO, such as metal nanowire,¹⁰⁶⁻¹⁰⁸ carbon nanotube (CNT),^{109, 110} graphene^{97, 111} and metal mesh.^{100, 112} Among these conducting nano-materials, silver nanowire (AgNW) networks have been known as an attractive flexible transparent electrode in various photovoltaic devices owing to their excellent electrical and

optical properties as well as outstanding mechanical flexibility.¹¹³⁻¹¹⁵ In addition, AgNW networks can be readily deposited using solution processing, such as spin-coating,¹¹⁶ bar-coating,^{114, 117} spray-coating,¹¹⁸ and vacuum filtration.¹¹⁹ However, such conventional solution-based processes result in random AgNW networks, which limits the application of AgNWs in high-performance flexible PSCs due to the problems related to NW aggregation; specifically, low transmittance and high surface roughness.^{113, 120} In particular, during the fabrication of PSCs, AgNWs are severely damaged by the halogen ions present in the perovskite active layer, resulting in the formation of a nonconducting silver halide phase, which decreases the electrical conductivity of the AgNWs.¹⁰⁰

To overcome the aforementioned limitations, researchers have attempted to prevent the diffusion of halogen ions by depositing passivation layers onto random AgNW networks.^{107, 108} Lee et al. reported that the iodide ions in PbI_2 and $\text{CH}_3\text{NH}_3\text{I}$ lead to a chemical reaction between AgNWs and iodine species, resulting in the formation of AgI, which in turn leads to the diffusion of Ag^+ from the AgNWs through defect sites in stacked layers. Thus, they developed AgNW-based flexible PSC devices with an amorphous metal oxide protective layer on both sides of the AgNW layer; their device achieved power conversion efficiency (PCE) of 11.23%.¹⁰⁸ Kim et al. reported the fabrication of all-solution-based transparent electrodes with random AgNW networks embedded in both sol-gel ITO and zinc oxide layers, which effectively prevented the formation of silver halides during the fabrication of PSCs. However, such methods require complex fabrication processes to form the oxide/metal NW/oxide structure or a thick buffer layer to fully cover protruding NWs in random AgNW networks. In addition, further improvement in the device efficiency remains a challenge that must be overcome to enable the practical application of AgNWs in flexible devices. Therefore, a method that enables manipulation of the surface morphology of AgNW networks to efficiently prevent silver halide formation and simultaneously improve device efficiency is needed.

In this study, we demonstrate the fabrication of PSC devices with orthogonal AgNW transparent electrodes. The orthogonal orientation of the AgNWs effectively prevents the formation of silver halide during the PSC device fabrication because of the smooth surface morphology, resulting in a higher device efficiency of 15.18% for the orthogonal AgNW electrodes on glass substrates compared with that (10.3%) of electrodes with random AgNWs. In addition, we present ultralight and flexible PSC devices with orthogonal AgNW electrodes fabricated on ultrathin (1.3- μm -thick) polyethylene naphthalate (PEN) foils. In addition to achieving an outstanding power-per-weight of $29.4 \text{ W}\cdot\text{g}^{-1}$ with a PCE of 12.85%, the PSCs can be attached to an arbitrary surface because of their low thickness and weight.

7. 2 Experimental details

Fabrication of ultrathin transparent electrodes with orthogonal AgNW arrays.

To support ultrathin PEN foil as the substrate, planar PDMS films were prepared by mixing silicone elastomer base (Sylgard 184, Dow Corning) and curing agent in a ratio of 10:1. The mixture of liquid PDMS prepolymer was poured into Petri dishes and stored in a vacuum desiccator for 30 min to eliminate air bubbles. The liquid PDMS prepolymer was then solidified at 90°C for 3h. The 1.3- μm -thick PEN foil was physically adhered onto a planar PDMS film. The PEN foil on the PDMS film was treated with O₂ plasma for 5 min to provide hydrophilicity and surface wettability. The as-treated PEN foil was then functionalized with amine groups using 0.1% poly-L-lysine (PLL) chemical solution in H₂O, which were spin-coated onto substrates at 4000 rpm for 60s. Next, orthogonal AgNW networks were fabricated on substrates terminated with amine functional groups by second-step capillary printing. Here, 0.5 wt.% AgNW dispersions (average length and average diameter of 25 ± 5 and 32 ± 5 nm, respectively) in ethanol (Nanopyxis Corp.) were used.

Materials and preparation of perovskite.

IPA and anhydrous N,N-dimethylformamide (DMF) were purchased from Sigma-Aldrich and were used without purification. Lead(II) iodide (PbI₂, 99.999%) was purchased from Alfa Aesar. Poly(3,4-ethylenedioxythiophene):poly(4-styrenesulfonate) (PEDOT:PSS, PH1000) was acquired from H. C. Starck (Germany). MAI was prepared according to a previously reported procedure.³² To prepare perovskite precursor solutions, 1.4 mM of PbI₂ was dissolved in 1 mL of DMF, and the concentration of MAI precursor was varied from 50 to 65 mg·mL⁻¹ in IPA. A 25 mg·mL⁻¹ solution of PC61BM was prepared in a 1:1 mixture of chlorobenzene and chloroform. The obtained solution was stirred at room temperature for 30 min.

Device fabrication.

ITO-coated glass substrates were cleaned by ultra-sonication in deionized water, acetone, and isopropyl alcohol for 10 min each. For glass/ITO devices, a PEDOT:PSS layer was deposited onto cleaned ITO substrates by spin-casting at 4000 rpm for 30 s, followed by annealing at 140°C for 10 min. For glass/AgNW and flexible AgNW substrates, a PH1000 was spin cast for 2000 rpm for 40 s and annealed 140°C for 15 min. An AI4083 layer was deposited onto the PH1000 layer by spin-casting at 1500 rpm for 30 s, followed by annealing at 140°C for 10 min. For ultralight substrates, a PH1000 layer was spin cast at 2000 rpm for 40 s and annealed at 80°C for 30 min. An AI4083 layer was then deposited onto the PH1000 layer by spin-casting at 1500 rpm for 30 s, followed by annealing at 80°C for 30 min. On top of the hole transport layer, MAI precursor solutions were spin cast at 3000 rpm for 30 s and PbI₂ solution was spin-coated at 5000 rpm for 30 s. The films were dried on a hotplate at 100°C for 2 min

under air atmosphere. After the substrates cooled, SVA was carried out using 40 μL of DMSO solvent for 2 min at 100°C . On top of the perovskite layer, PC61BM was spin cast at 1500 rpm. Subsequently, an Al electrode with a thickness of 100 nm was deposited onto the PC61BM layer under vacuum ($<10^{-6}$ Torr) by thermal evaporation.

Characterization

The J - V characteristics of the solar cells were measured using a Keithley 2635A source meter. Solar cell performance was characterized with the cells under illumination by an air mass 1.5 global (AM 1.5G) solar simulator with an irradiation intensity of $100 \text{ mW}\cdot\text{cm}^{-2}$. Apertures (13.0 mm^2) made of thin metal were attached to each cell before measurement of the J - V characteristics. EQE measurements were obtained with a PV measurement QE system under ambient conditions with monochromated light from a Xe arc lamp. The monochromatic light intensity was calibrated with a Si photodiode and chopped at 100 Hz. XPS measurements were carried out using an ESCALAB 250XI from Thermo Fisher Scientific. The power-per-weight is defined as the ratio between the device output power per unit area under AM 1.5G $100 \text{ mW}\cdot\text{cm}^{-2}$ illumination and device weight per unit area. The ultralight PSCs achieved a PCE of 12.85% and weighed $\sim 4.37 \text{ g}\cdot\text{m}^{-2}$. Therefore, the device would generate a $128.5 \text{ W}\cdot\text{m}^{-2}$ power output, with a specific weight of $29.4 \text{ W}\cdot\text{g}^{-1}$

7.3 Results and discussion

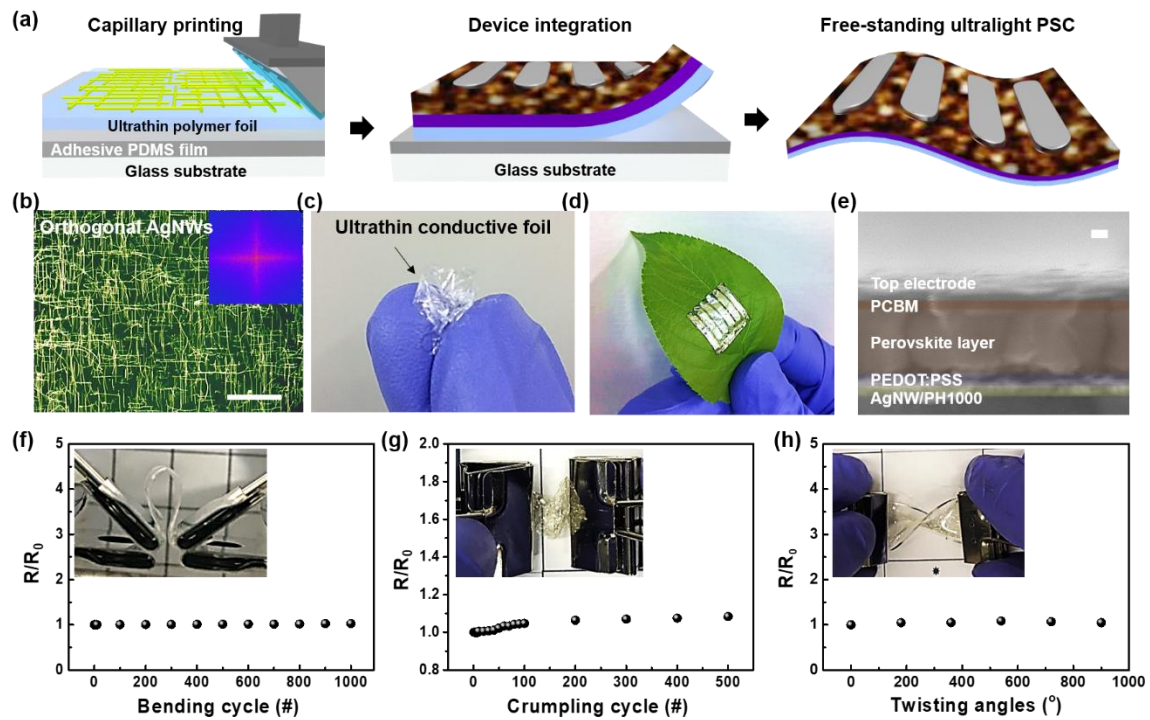


Figure 7. 1. (a) Schematics of the fabrication procedure for ultrathin orthogonal AgNW transparent electrodes produced on 1.3- μm -thick PEN foil. (b) Dark-field optical microscopy image of the orthogonal AgNW arrays; the corresponding FFT pattern is shown in the inset. The scale bar indicates 40 μm . (c) The ultrathin orthogonal AgNW transparent electrode foil, crumpled by a person's finger. (d) An ultrathin and lightweight PSC device mounted onto the surface of a leaf. (e) Cross-sectional SEM image of the device structure for a PSC with the orthogonal AgNW array. The scale bar is 100 nm. (f–h) Mechanical properties of the orthogonal AgNW transparent electrode foils. Variation in resistance of orthogonal AgNW electrode foil as a function of (f) bending cycles at a bending radius of 2 mm, (g) crumpling cycles, and (h) twisting angles. The inset images show corresponding deformation (twisting, crumpling, bending) of the orthogonal AgNW electrode foil adhered to the PDMS thin film

Figure 7. 1a shows the schematic of fabrication process for ultralight and flexible PSC with orthogonal AgNW transparent electrodes on ultrathin 1.3 μm -thick PEN foils. Firstly, we prepared polydimethylsiloxane (PDMS) films, which are subsequently laminated to glass substrate. This preparation step is followed by the lamination step of ultrathin 1.3 μm -thick PEN foils to the PDMS film in which ultrathin PEN foils are physically attached to the surface of PDMS film for easy handling during the device fabrication. And, the orthogonal AgNW electrodes are fabricated using capillary printing technique via multi-step process.¹¹³ Next, PH1000 and AI4083 layers are over-coated for a passivation layer and hole transporting layers (HTLs) on orthogonal AgNW electrodes, respectively. The perovskite active layers are fabricated by a standard two-step method in regular succession.¹²¹ After

the deposition of top electrodes, as-fabricated ultrathin PSC devices on PEN foil are physically released and free-standing. Here, orthogonal AgNW electrodes provide several advantages as high-performance flexible transparent electrodes, such as uniform electrical current path, smooth surface morphologies, and superior transmittance, which increase charge carrier diffusion lengths and reduce charge recombination to achieve high device performance of PSCs.^{4, 14} Dark-field optical micrograph of orthogonal AgNW network indicates highly oriented NW surface morphology with the inset of fast Fourier transform (FFT) image, which exhibits crossed line patterns, corresponding to its surface geometry (**Figure 7. 1b**) In the contrary, random AgNW network showed disordered surface structures with blurry circular patterns of FFT image (**Figure 7. 2**). Optical transmittance in the visible wavelength of 400 – 800 nm was measured for orthogonal and random AgNW networks. We confirmed that orthogonal AgNW electrodes provide higher transmittance (92.3% at 550 nm wavelength) than random AgNW electrodes with similar sheet resistance (90.8% at 550 nm wavelength) due to lower percolation threshold (**Figure 7. 3**).¹¹⁴ The ultrathin conductive foil with orthogonal AgNW networks (**Figure. 7. 1c**) is highly flexible and transparent. **Figure 7. 1d** shows an ultralight and flexible PSC with an orthogonal AgNW electrode foil adhered to the surface of a leaf, demonstrating the high adhesive capability due to the very small thickness and lightness of the device, which can facilitate the use of our PSCs as a wearable power source. **Figure 7. 1e** shows a cross-sectional scanning electron microscopy (SEM) image of our PSC with orthogonal AgNW electrodes. PSC devices are based on p–i–n device structures with a configuration of polyethylene naphthalate (PEN)/orthogonal AgNW electrode/PH1000/poly(3,4-ethylenedioxythiophene):poly(styrenesulfonate) (PEDOT:PSS)/CH₃NH₃PbI₃ (MAPbI₃)/phenyl-C61-butyric acid methyl ester (PCBM)/aluminum (Al). The energy band diagram of the PSC devices is shown in **Figure 7. 4**.

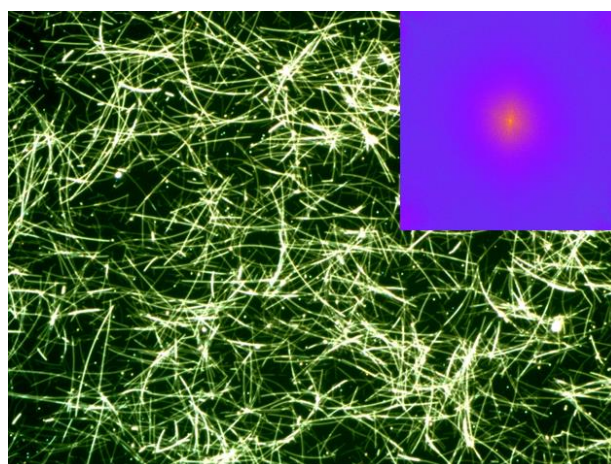


Figure 7. 2. Dark-field optical micrograph of a random AgNW network. The fast Fourier transform (FFT) image of the optical micrograph (inset) shows a blurred circular pattern, reflecting the randomness of the corresponding surface geometric structure. The scale bar indicates 40 μm.

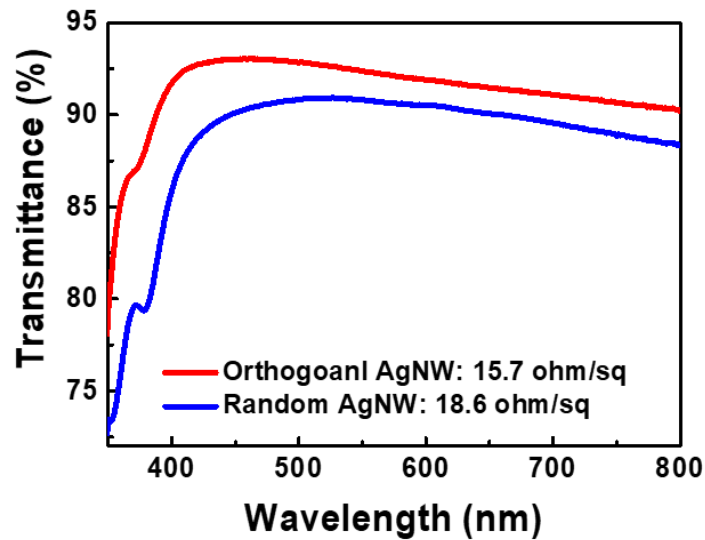


Figure 7. 3. The optical transmittance of orthogonal AgNW and random AgNW electrodes deposited onto glass substrates. Samples were scanned over the visible wavelength range (350–800 nm). The corresponding sheet resistances of the electrodes are given in the figure. The glass substrate was used as a reference

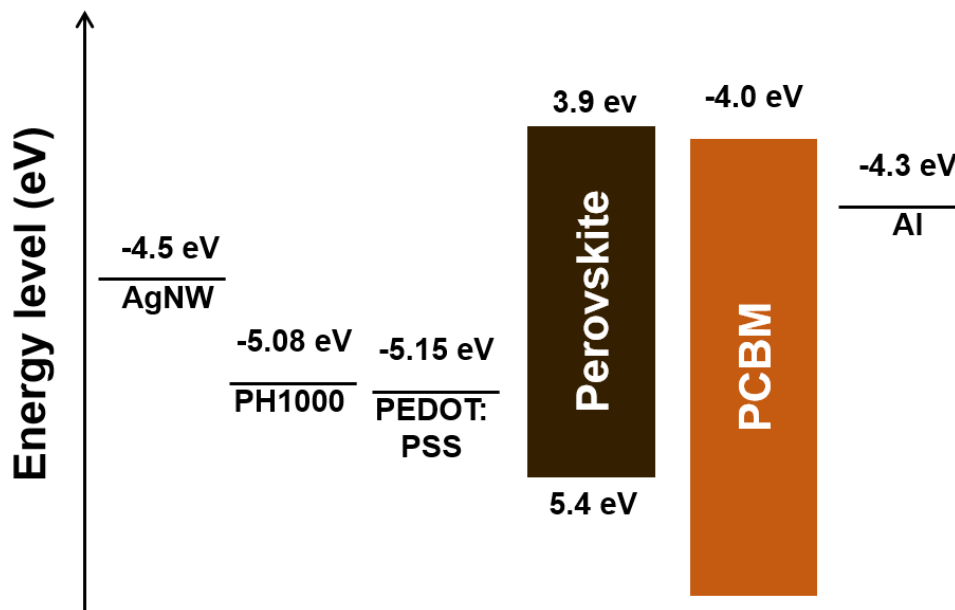


Figure 7. 4. The energy band diagram for the PSC with an orthogonal AgNW electrode.

To investigate the mechanical robustness of the orthogonal AgNW electrode foils, the resistance of the orthogonal AgNW electrodes was monitored under various mechanical deformations, such as bending, crumpling, and twisting. The orthogonal AgNW electrode foil sustains its electrical resistance without substantial variation during repeated bending cycles (1000 times) at a bending radius of 2 mm (Fig. 1f), repeated crumpling cycles (500 times) (**Figure 7. 1g**), and twisting deformation at twisting angles from 0° to 90° (**Figure 7. 1h**). The outstanding mechanical durability of the orthogonal AgNW

electrode foils is attributed to their uniform conductive networks bonding via an electrostatic force induced by chemically modified substrates with amine functional groups.

During the fabrication of AgNW-based PSC devices, the formation of nonconducting silver halides, which substantially reduces the electrical conductivity of the AgNW electrodes, is a critical issue. To address this problem, we deposited a PH1000 layer as a passivation layer to minimize the formation of AgI during fabrication of the AgNW-based PSC devices.⁷ The smooth surface morphologies of the orthogonal AgNW electrodes laminated with a PH1000 layer can effectively prevent the reaction between AgNWs and iodide ions. On the contrary, protruding NWs induced by the aggregation of random AgNW networks cannot be fully covered by PH1000 layers, allowing iodide ions to easily diffuse into exposed AgNWs, resulting in a decrease of the electrical conductivity (**Figure 7. 5a**)

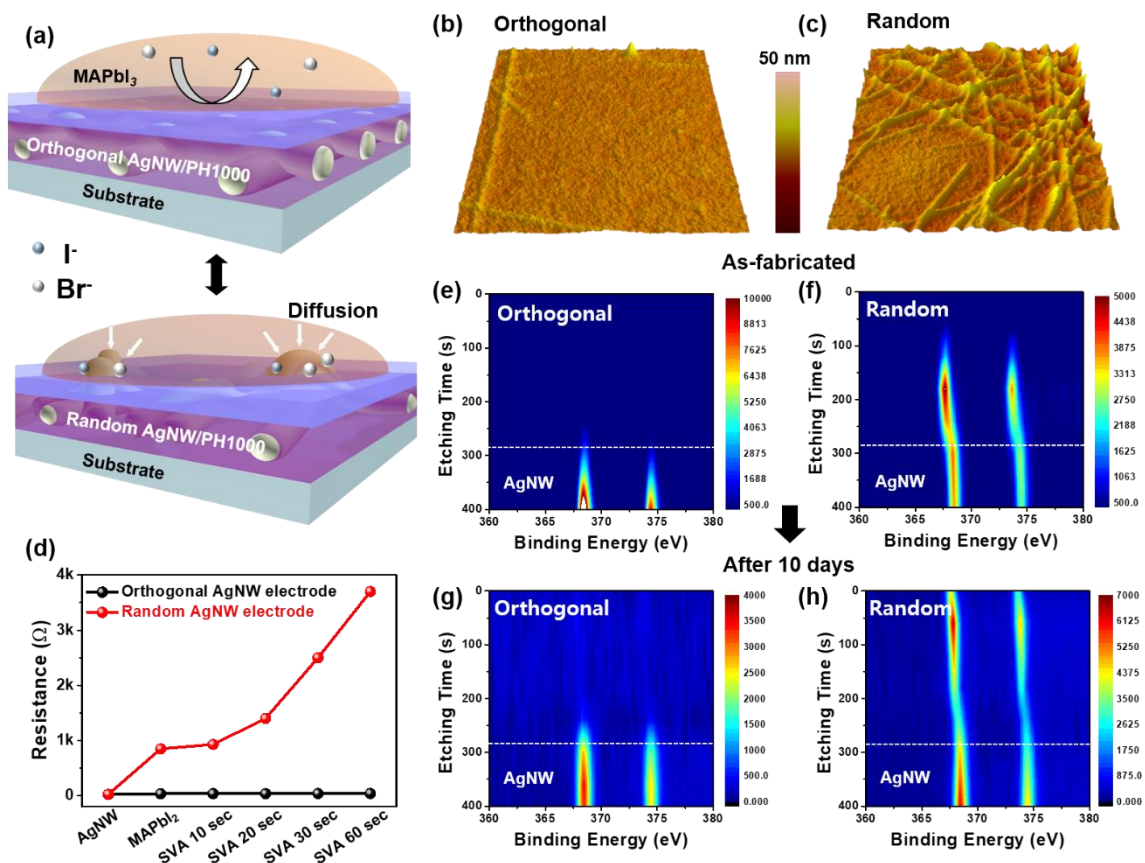


Figure 7. 5. (a) Schematic of silver halide formation in PSCs fabricated on random and orthogonal AgNW electrodes. (b,c) AFM images of the surface of PEDOT:PSS coated onto (b) a PH1000/orthogonal AgNW electrode and (c) a PH1000/random AgNW electrode, respectively. (d) Variation in the resistance of both the random and orthogonal AgNW electrodes as a function of the SVA time. (e–h) Mapping images for the binding energy of Ag3d originating from XPS depth profiles of PSCs with orthogonal AgNW and random AgNW electrodes (e,f) before and (g,h) after aging for 10 day

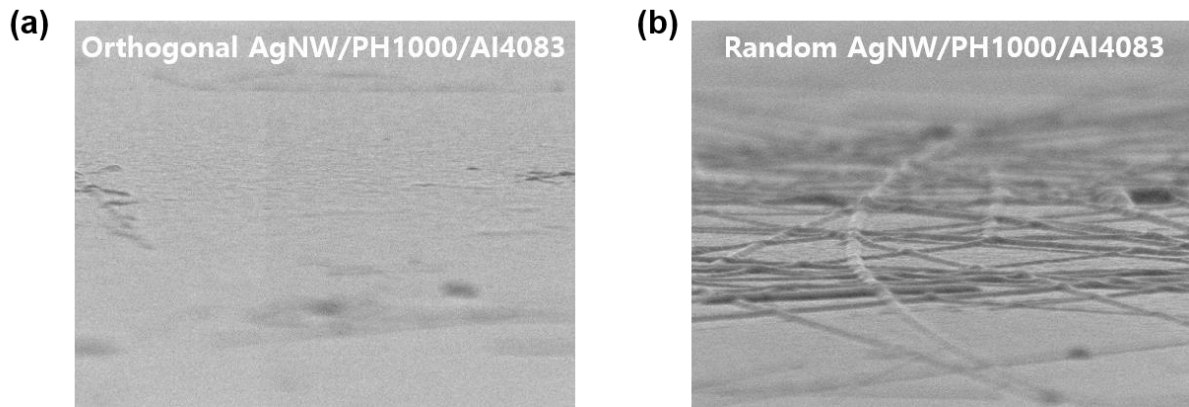


Figure 7. 6. Tilted SEM images of the surface of PEDOT:PSS coated onto (a) a PH1000/orthogonal AgNW electrode and (b) a PH1000/random AgNW electrode.

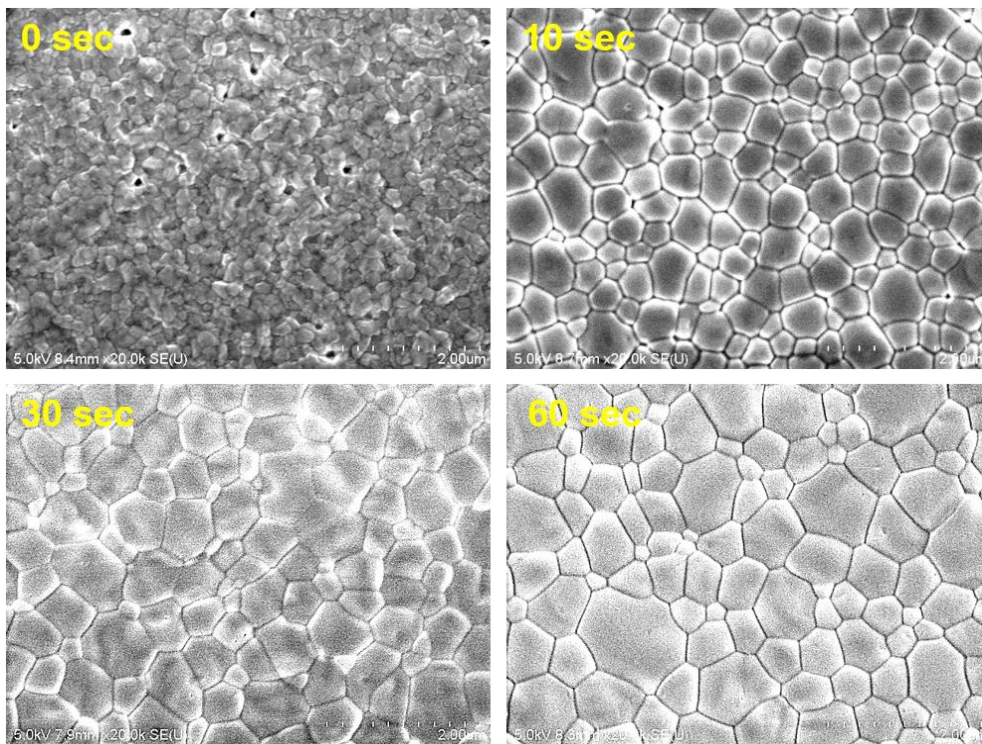


Figure 7. 7. SEM images of the surface of perovskite active layers deposited onto PEDOT:PSS/PH1000/AgNW; the images correspond to different SVA times.

To verify the smooth surface morphologies of the orthogonal AgNW electrodes, we analyzed the surface of PEDOT:PSS (AI4083) layers deposited onto PH1000/orthogonal and random AgNW electrodes (**Figure 7. 6**). The AI4083/PH1000 layer does not efficiently cover the whole area of the random AgNW network because the AgNWs are aggregated, resulting in a poor surface morphology. On the contrary, the orthogonal AgNW/PH1000 electrode exhibits a uniform and smooth surface morphology with excellent surface coverage of AgNWs. To further investigate the smooth morphologies of orthogonal AgNW electrodes, we measured the surface roughness of PEDOT:PSS

films deposited onto orthogonal and random AgNW/PH1000 electrodes using atomic force microscopy (AFM). **Figure. 2b and 2c** reveal that the surface of the PEDOT:PSS film on orthogonal AgNW/PH1000 electrodes is smoother (root-mean-square roughness, $R_q = 1.47$ nm) than that on the random AgNW electrodes ($R_q = 4.8$ nm), which is consistent with the surface morphologies observed by SEM. These topological results indicate that the orthogonal AgNW/PH1000 electrodes can prevent the formation of AgI more effectively than random AgNW electrodes.

To certify the capability of orthogonal AgNW electrode to prevent the AgI formation in the fabrication of PSC device, we monitored the variation in the sheet resistance of orthogonal and random AgNW/PH1000/AI4083 films during the device fabrication in which the deposition of perovskite films are followed by solvent vapor annealing (SVA) process with dimethyl sulfoxide (DMSO) solution. Here, it is widely known that DMSO vapor provide a wet environment condition so that MAI and PbI_2 precursor molecules and ions can diffuse a long distance, resulting in an increase of grain size from 200 nm to over 1 μm as a function of SVA time for improving device efficiency (**Figure 7. 7**).¹²² However, the diffusion of iodine species into AgNW electrode during SVA can promote the AgI formation, leading to further degradation in electrical conductivity. As a result, orthogonal AgNW electrodes maintain initial electrical resistance without significant loss of electrical conductivity during an entire fabrication process while random AgNW networks show severe damage in an electrical resistance with a rapid increase of the sheet resistance (**Figure 7. 5d**). Note that thicker PH1000 layer does not guarantee high device performance, which results in a decrease of charge collection efficiency and series resistance, although they fully cover the protruding NWs of random AgNW network.¹²³ These topological results indicate that orthogonal AgNW/PH1000 electrodes can effectively prevent the formation of AgI than random AgNW electrodes.

To further validate the capability of orthogonal AgNW electrode to prevent the AgI formation for the fabrication of PSCs, we measured X-ray photoelectron spectroscopy (XPS) depth profile analysis in which orthogonal AgNW/HTL/perovskite and random AgNW/HTL/perovskite films were prepared for comparison, respectively. Binding energy of Ag ion for both samples were measured using X-ray photoelectron spectroscopy (XPS) after the solvent?? aging process for 10 days in the globe box at room temperature (Figures 2g and 2h). Random AgNW electrode sample was obtained Ag^+ and Ag metal peaks at 367.9 eV and 368.2 eV which indicate the presence of Ag^+ ion was founded in the top regime of the cell stack by reacting with iodine of perovskite layer, whereas in the case of the orthogonal AgNW electrode showed only Ag metal peak at 368.2 eV after 250s etching times past, implying that orthogonal AgNW system effectively prevents the perovskite photoactive layer from contacting AgNW electrode.¹²⁴

To better understand the ability of the orthogonal AgNW electrode to prevent AgI formation, we performed X-ray photoelectron spectroscopy (XPS) depth profile analysis of orthogonal AgNW/PH1000/HTL/perovskite and random AgNW/PH1000/HTL/perovskite films. The as-fabricated

films were subjected to an aging process for 10 days in a N₂-filled glove box at room temperature. The mapping images of the binding energy of Ag⁺ ions before and after the aging treatment were constructed using XPS analysis (**Figure 7. 5e–h**). The y-axis scale in the mapping images indicates the etching time, which corresponds to the depth of the device. The XPS spectrum of an as-fabricated sample with a random AgNW network shows both Ag⁺ ions and Ag metal peaks at 367.9 and 368.2 eV, respectively, indicating that Ag⁺ ions were present in the perovskite active layer because of the reaction of Ag metal with the iodine of the perovskite solution. On the contrary, the spectra of the orthogonal AgNW electrodes show only a Ag metal peak at 368.2 eV; thus, Ag atoms did not diffuse from their corresponding positions in the AgNWs (**Figure 2e and f**). In addition, the spectrum of the orthogonal AgNW network aged for 10 days shows no changes in the binding energy or peak position, whereas the random AgNW network aged for 10 days exhibited remarkable diffusion of Ag⁺, as evidenced by a shift in the binding energy, leading to AgI formation along the top regime of the device (**Figure 2g and h**). These XPS results imply that the orthogonal AgNW system effectively prevents direct contact between the perovskite photoactive layer and AgNW electrode.¹²⁵[ref]

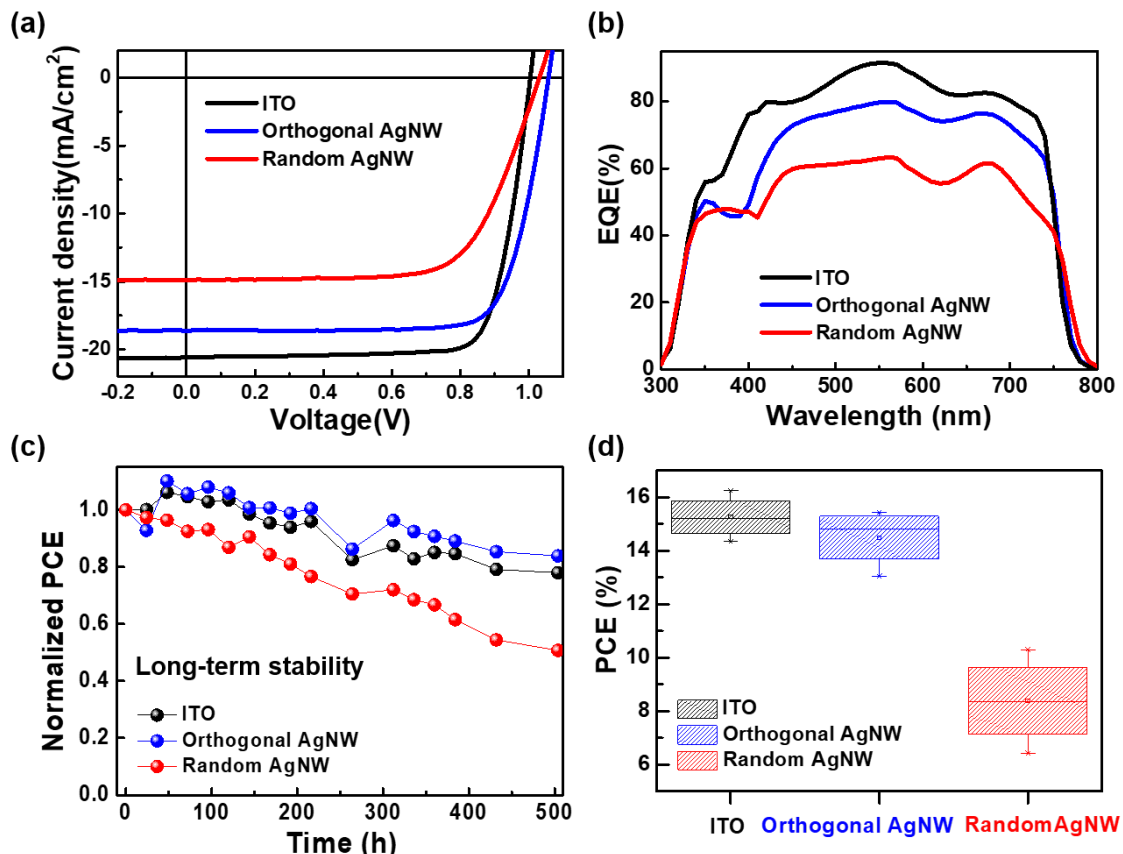


Figure 7. 8. (a) J–V characteristic and (b) IPCE of PSC devices with ITO, orthogonal AgNW, and random AgNW electrodes. (c) Long-term stability of PSCs under a controlled atmosphere (N₂-filled glove box). (d) The quantitative PCE values of PSCs with ITO, orthogonal AgNW, and random AgNW electrodes.

Table 7. 1. J–V characteristics of PSC devices with ITO, orthogonal AgNW, and random AgNW electrodes fabricated on glass substrates.

Electrode	J_{sc} (mA cm ⁻²)	V_{oc} (V)	FF	PCE (%)	Cal. J_{sc}
ITO	20.09	1.00	0.79	16.25	19.79
Orthogonal AgNW	18.63	1.06	0.77	15.18	17.51
Random AgNW	14.88	1.03	0.68	10.43	14.07

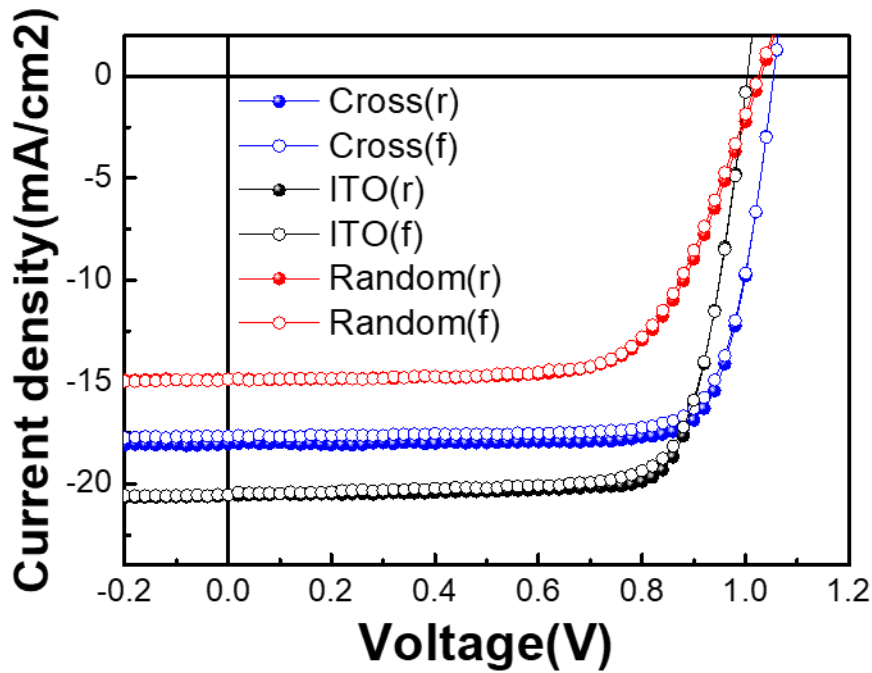


Figure 7. 9. J–V hysteresis characteristics of a PSC with ITO, orthogonal AgNW and random AgNW electrode measured with forward and reverse bias

Table 7. 2. Summarized J – V hysteresis characteristics of a PSC with ITO, orthogonal AgNW and random AgNW electrode measured with forward and reverse bias.

Electrode	Scan direction	J_{sc} (mA/cm ²)	V_{oc} (V)	FF	PCE (%)
ITO	Reverse	20.32±0.366	1.00±0.003	0.78±0.005	16.00±0.258
	Forward	20.46±0.099	1.00±0.001	0.76±0.002	15.68±0.072
Orthogonal AgNW	Reverse	14.38±0.602	1.03±0.001	0.67±0.012	9.88±0.555
	Forward	14.27±0.576	1.02±0.012	0.67±0.01	9.80±0.519
Random AgNW	Reverse	18.20±0.301	1.06±0.008	0.78±0.015	15.06±0.174
	Forward	17.98±0.282	1.05±0.003	0.78±0.014	14.81±0.285

To validate the effect of the orthogonal AgNW electrode on the device performance of AgNW-based PSCs, we measured the current density–voltage (J – V) characteristics for PSC devices with ITO, orthogonal AgNW, and random AgNW electrodes under AM 1.5G illumination at $100 \text{ mW}\cdot\text{cm}^{-2}$ (**Figure 7. 8a**). The control perovskite solar cells were prepared with the architecture ITO/PEDOT/MAPbBr_xI_{3-x}/PC61BM/Al. The PSCs with orthogonal AgNW have a structure with orthogonal AgNW/PH1000/AI4083/MAPbBr_xI_{3-x}/PC61BM/Al while the PSCs with random AgNW have a structure with random AgNW/PH1000/AI4083/MAPbBr_xI_{3-x}/PC61BM/Al. The PSCs with ITO electrodes exhibited a short-circuit current density (J_{SC}) of $20.09 \text{ mA}\cdot\text{cm}^{-2}$, open-circuit voltage (V_{OC}) of 1.00 V, fill factor (FF) of 79%, and overall PCE of 16.25% (**Table 7. 1**). Notably, the PSCs with orthogonal AgNW electrodes achieved an outstanding PCE of 15.18% with a J_{SC} of $18.63 \text{ mA}\cdot\text{cm}^{-2}$, V_{OC} of 1.06 V, and FF of 77%, whereas those with random AgNW electrodes yielded a lower PCE of 10.43% with J_{SC} of $14.84 \text{ mA}\cdot\text{cm}^{-2}$, V_{OC} of 1.03 V, and FF of 68%. The improved V_{OC} in the HTL/Perovskite device can be understood by examining the schematic energy diagram shown in Figure S3. The V_{OC} is usually determined by built in potential (V_{bi}) in the devices. In this case, V_{bi} in devices is dependent on the work function of AgNW/PH1000/PEDOT:PSS rather than on the work function of ITO/PEDOT. When the work function of AgNW/PH1000/PEDOT:PSS is effectively aligned with ionization potential of perovskite photoactive layer, the potential energy loss at the interface will be minimized.[ref] The high performance of the PSCs with the orthogonal AgNW electrodes is attributed to the uniform and homogenous perovskite photoactive layer on the flat HTL, which can increase the charge collection efficiency and reduce the recombination by the smooth surface of the orthogonal AgNW electrodes without forming AgI. In the forward scan direction, the PSCs with orthogonal AgNW electrodes exhibited a PCE of 15.43% with a J_{SC} of $18.60 \text{ mA}\cdot\text{cm}^{-2}$, V_{OC} of 1.05 V, and FF of 79%, which are comparable to the characteristics of the backward scan, indicating that our PSC devices provide reliable device performance with negligible photocurrent hysteresis (**Figure 7.9 and Table 7.2**).¹²⁶ **Figure 7. 8b** shows an external quantum efficiency (EQE). The PSC devices with ITO, orthogonal and random AgNW electrodes show broad spectral response in the range of 300-780 nm and calculated current density is $19.79 \text{ mA}\cdot\text{cm}^{-2}$, $17.51 \text{ mA}\cdot\text{cm}^{-2}$, and $14.07 \text{ mA}\cdot\text{cm}^{-2}$, respectively. The integrated photocurrent of both devices show only 6% mismatch with obtained value from J - V curve which implies well agreement and substantiates the observed J_{SC} .

To characterize the stability of PSCs with orthogonal AgNW electrode, the device performance was continuously monitored with aging time for 500 hours in the globe box. The PSC with orthogonal AgNW electrode showed an improvement in long-term stability compared to the PSC with random AgNW electrode as shown in **Figure 7. 8c**. For PSC devices with orthogonal AgNW electrode, 85% of the initial PCE was retained after 500 hours while PSC devices with random AgNW electrode rapidly decreased less than 50% after 500 hours. This improved stability of device with orthogonal AgNW electrode could be attributed to preventing the reaction Ag⁺ with I⁻ ions due to the smooth surface,

which shows good agreement with XPS depth profile. **Figure 7. 8d** presents the statistical analyses of device performance obtained from PSCs with ITO, orthogonal and random AgNW electrodes, respectively. Both devices with ITO and orthogonal AgNW electrodes showed high reproducibility with small variation in device efficiency, whereas PSCs with random AgNW electrodes have large variation in device performance.

To demonstrate the application of our orthogonal AgNW electrodes in a flexible device, we fabricated flexible PSCs with orthogonal AgNW electrodes on 1.3- μm -thick PEN foils (ultrathin PSCs) and on 120- μm -thick PEN films (thin PSCs). **Figure 7. 10a** shows the J–V characteristics of the ultrathin and thin PSCs with orthogonal AgNW electrodes. Device efficiencies of 13.05% and 12.85% were achieved for the ultrathin PSC and thin PSC devices with orthogonal AgNW electrodes, respectively, which constitute the highest PCEs reported thus far for a flexible PSC with AgNW electrodes¹²⁷⁻¹³⁰ (**Table 7. 3**).

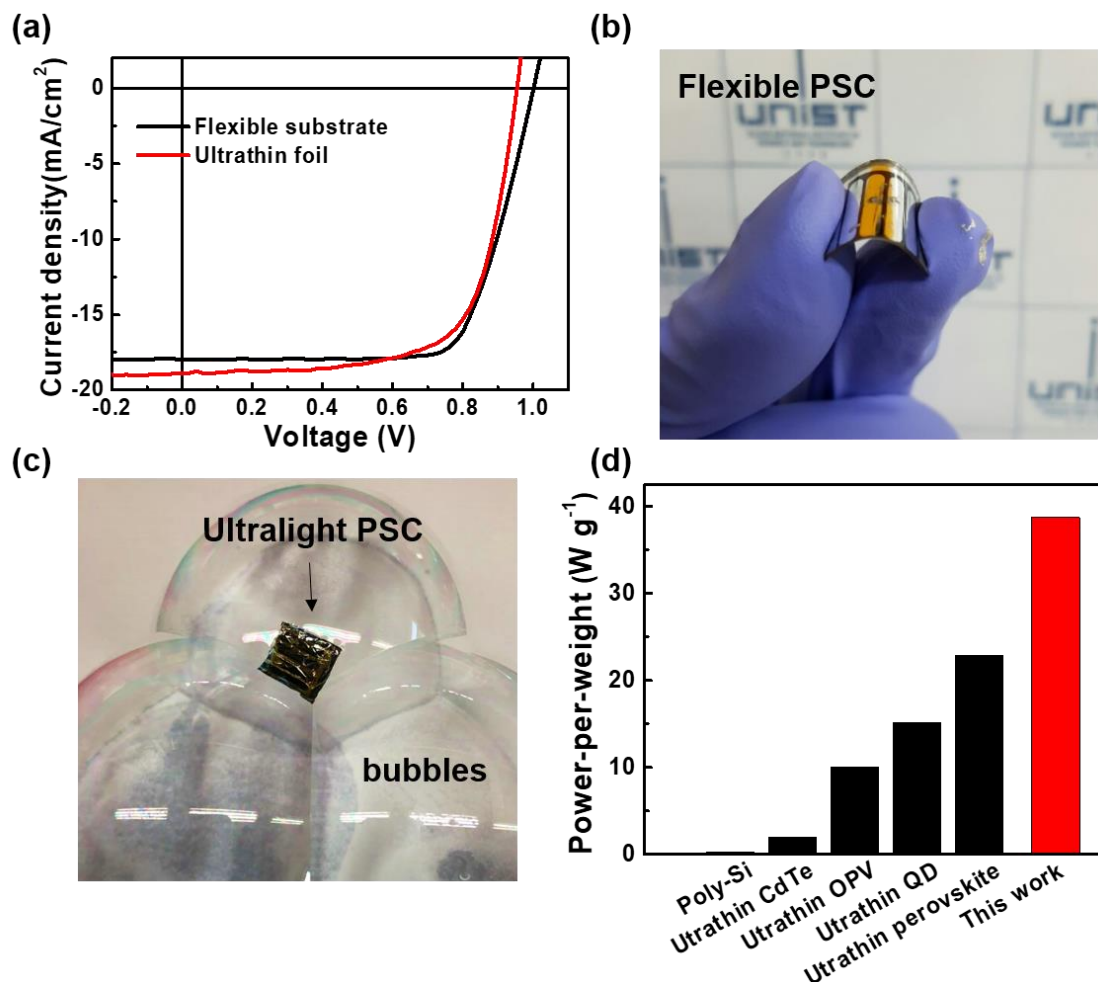


Figure 7. 10. (a) J–V characteristics of a flexible PSC with an orthogonal AgNW electrode fabricated on a 1.3- μm -thick PEN foil and a 120- μm -thick PEN film. (b) Photograph of a flexible PSC fabricated on an orthogonal AgNW electrode. (c) An ultralight PSC suspended in bubbles. (d) Comparison of the power-per-weight performances of the ultralight PSC and other types of light solar cells.

Table 7. 3. Comparison of the device performance of our PSC with orthogonal AgNW arrays and those of other AgNW-based PSC devices.

Device structure	J_{sc} (mA/cm ²)	V_{oc} (V)	FF	PCE (%)	Ref.
Glass/AZO/AgNW/a-AZO/ZnO/Perovskite/Spiro-OMeTAD/Au	18.5	1.12	67.4	13.93	Adv. Energy Mater. 2018 ¹³⁰
Glass/FTO/TiO ₂ /Perovskite/Spiro-OMeTAD/AgNWs/PDMS	15.24	1.07	68.8	11.12	Adv. Funct. Mater. 2018 ¹²⁷
ITO/PTAA:F4TCNQ/Perovskite/PCBM/AgNW@Au	18.5	0.99	64.3	11.0	Sol. Energy Mater. Sol. Cells 2017 ¹²⁸
Au/Spiro-OMeTAD/CH ₃ NH ₃ PbI ₃ /mAl ₂ O ₃ /ZnO/ITO/AgNW/ITO	13.17	1.04	61.8	8.44	Nanoscale 2016 ¹⁰⁷
AgNW/ZnO:F/TiO ₂ /Perovskite/Spiro-OMeTAD/Ag	12.2	0.685	39.5	3.29	J. Mater. Chem. A 2015 ¹²⁹
Glass/orthogonal AgNW/PH1000/PEDOT:PSS/MAPbI₃/PCBM/Al	18.63	1.06	0.77	15.18	This work
Flexible film/orthogonal AgNW/PH1000/PEDOT:PSS/MAPbI₃/PCBM/Al	17.99	1.00	0.72	13.05	This work
Ultrathin foil/orthogonal AgNW/PH1000/PEDOT:PSS/MAPbI₃/PCBM/Al	18.88	0.95	0.69	12.85	This work

To evaluate the mechanical stability for flexible PSC with orthogonal AgNW electrode, the variation of device performance of flexible PSCs was measured under 1000 bending cycles at 5 mm of bending radius (**Figure 7. 10b**). The device performance for flexible PSC remains 80% of the initial PCE over 1000 bending cycles without significant degradation of PCE value.(**Figure 7. 11**)

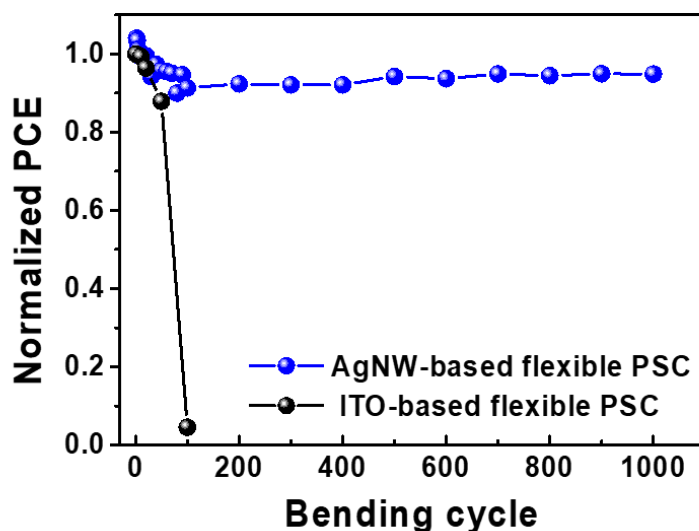


Figure 7. 11. Variation in normalized device efficiency of PSCs with ITO and orthogonal AgNW electrodes under repeated (1000 times) bending cycles



Figure 7. 12. Photograph of an ultralight PSC device on an electronic scale, demonstrating its extremely low weight. The device size is 13 mm x 13mm

One of important advantages of our devices is their lightweight property, which enables our devices to be floated even onto the surface of bubbles without bursting (**Figure 7. 10c**). The ultralight property of our PSCs is highly advantageous in terms of the power-per-weight in the field of aerospace electronics or miniaturized blimps. For the proof-of-concept demonstration, we calculated the power-per-weight of our device, which weighed 0.74 mg (**Figure 7. 12**); our ultralight and flexible PSC device exhibited an excellent power-per-weight of $29.4 \text{ W}\cdot\text{g}^{-1}$ at a weight of $4.37 \text{ g}\cdot\text{m}^{-2}$, which represents the highest value reported among various lightweight solar cells (**Figure 7. 10d**).^{94, 97-99}

7.4 Conclusion

In summary, we demonstrated ultrathin, lightweight, and flexible PSC devices with orthogonal AgNW transparent electrodes fabricated on ultrathin polymer foils. The orthogonal AgNW electrodes provide a smooth surface morphology and exhibit outstanding electrical and optical properties, which effectively prevent the formation of nonconducting AgI, resulting in an improved device efficiency, achieving a PCE of 15.18% in comparison with that of a device with random AgNW electrodes (10.3%). A PCE value of 13.05% for the flexible PSC with orthogonal AgNW electrodes was achieved, which is the highest device efficiency reported till date for an AgNW-based flexible PSC device. Furthermore, our ultralight PSC device fabricated on 1.3- μm -thick foil achieved a PCE of 12.85% with an excellent power-per-weight of $29.4 \text{ W}\cdot\text{g}^{-1}$ at weight of $4.37 \text{ g}\cdot\text{m}^{-2}$.

CHAPTER 8. Summary

In the thesis, I have investigated to improve morphology of perovskite photoactive layer via mixed solvent, chemical composition and compact seed perovskite layer (CSPL). And then apply CSPL technique to lightweight and flexible solar cell using silver nanowire electrode. Detailed summary as follows:

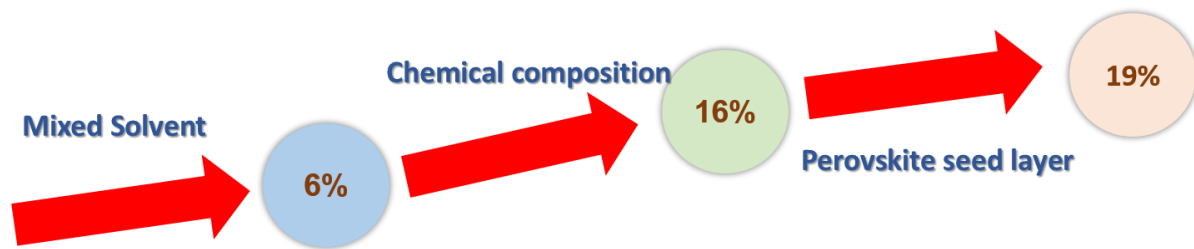


Figure 8. 1. Summary of morphology control of photoactive layer for high efficient perovskite solar cells.

First, we have successfully fabricated high performance p-i-n structure PeSCs using a DMF:GBL solvent mixture to improve the surface coverage and morphology of the perovskite layer. The perovskite and PCBM films were completely and sequentially deposited on PEDOT:PSS/ITO substrate via low-temperature solution processing. Employ of a mixture of DMF and GBL to process the perovskite precursor solution enhances interfacial contacts and reduces the defect between perovskite and PCBM layer by smooth perovskite film and uniform crystal domains, lead to improve exciton dissociation efficiency and reduces recombination losses at the perovskite/PCBM interface. Furthermore, this topic is the first report to introduce a mixed solvent system for the control perovskite film morphology in perovskite planar heterojunction solar cells.

Second, we synthesized a series of perovskite light absorbers with composition $Cs_xMA_{1-x}PbI_3$ and evaluated their performance in p-i-n type perovskite solar cells. High performance was achieved via 10% Cs doping in the $MAPbI_3$ perovskite structure, resulting in a ~40% enhancement in device efficiency via improvement in light absorption and morphology as well an increased energy difference between the valance band of perovskite and LUMO level of PCBM. Our approach to perovskite design offers the possibility to achieve even higher open-circuit voltages by employing tandem device structures

Third, we have investigated the influence of structural composition on the optoelectronic properties of the materials in order to achieve homogenous perovskite films by fractional substitution of $PbCl_2$ with $PbBr_2$ in the precursor solution. A composition comprising 10% Br substitution in the perovskite precursor solution yielded an optimal power conversion efficiency of 16%, constituting a ~30% enhancement compared to the binary system via the formation of smooth, defect free films and a deeper

valence band energy. These devices exhibit stable performance with a narrow distribution of device characteristics and negligible hysteresis. Compared to previous work using ternary halid perovskites, we were able to achieve a substantial increase in performance via the use of single, ternary halide containing precursor solution dissolved in a novel solvent (DMA), which led to improved morphology and device characteristics compared to the binary system. The approach reported here constitutes a significant advance in the application of ternary perovskite materials, providing a simple and effective way to prepare high performance perovskite active layers in a one-step process.

Next, we developed simple and effective way to form perovskite photoactive layer by controlling the seed perovskite layer with low-temperature solution processing techniques. Seed perovskite layer has an influence on vertical growth of perovskite crystal and adhesion between HTL and perovskite film, leading to improve optical and electrical properties of materials and overcome the problem of having lower open circuit voltage in inverted structure PeSCs. The PCE was achieved 19.25% in the p-i-n structure PeSCs with record open circuit voltage of 1.16 V and 20.37% of PCE in n-i-p structure devices with pure crystal perovskite film. The approach reported in this study constitutes a significant advance in the application of perovskite film formation, providing an easy and way to prepare high performance perovskite active layers in a both p-i-n and n-i-p architecture system.

Finally, we demonstrated ultrathin, lightweight, and flexible perovskite devices with orthogonal AgNW transparent electrodes. The orthogonal AgNW electrodes provide a smooth surface morphology and show outstanding electrical and optical properties, which prevent the formation of nonconducting AgI. A PCE value of 13.05% for the flexible PSC with orthogonal AgNW electrodes was achieved, which is the highest device efficiency reported till date for an AgNW-based flexible PSC device. Furthermore, our ultralight PSC device fabricated on 1.3- μm -thick foil achieved a PCE of 12.85% with an excellent power-per-weight of $29.4 \text{ W}\cdot\text{g}^{-1}$ at weight of $4.37 \text{ g}\cdot\text{m}^{-2}$

References

1. G. Li, R. Zhu and Y. Yang, *Nat. Photonics*, 2012, **6**, 153.
2. B. E. Hardin, H. J. Snaith and M. D. McGehee, *Nat. Photonics*, 2012, **6**, 162.
3. M. M. Lee, J. Teuscher, T. Miyasaka, T. N. Murakami and H. J. Snaith, *Science*, 2012, **338**, 643-647.
4. S. D. Stranks, G. E. Eperon, G. Grancini, C. Menelaou, M. J. P. Alcocer, T. Leijtens, L. M. Herz, A. Petrozza and H. J. Snaith, *Science*, 2013, **342**, 341-344.
5. G. Xing, N. Mathews, S. Sun, S. S. Lim, Y. M. Lam, M. Grätzel, S. Mhaisalkar and T. C. Sum, *Science*, 2013, **342**, 344-347.
6. A. Kojima, K. Teshima, Y. Shirai and T. Miyasaka, *J. A. Chem. Soc.*, 2009, **131**, 6050-6051.
7. Q. Chen, H. Zhou, Z. Hong, S. Luo, H.-S. Duan, H.-H. Wang, Y. Liu, G. Li and Y. Yang, *J. A. Chem. Soc.*, 2014, **136**, 622-625.
8. N. J. Jeon, J. H. Noh, Y. C. Kim, W. S. Yang, S. Ryu and S. I. Seok, *Nat. Mater.*, 2014, **13**, 897-903.
9. G. Wang, D. Li, H.-C. Cheng, Y. Li, C.-Y. Chen, A. Yin, Z. Zhao, Z. Lin, H. Wu, Q. He, M. Ding, Y. Liu, Y. Huang and X. Duan, *Science. Adv.*, 2015, **1**.
10. J. K. Lee, W. L. Ma, C. J. Brabec, J. Yuen, J. S. Moon, J. Y. Kim, K. Lee, G. C. Bazan and A. J. Heeger, *J. A. Chem. Soc.*, 2008, **130**, 3619-3623.
11. C. Eames, J. M. Frost, P. R. F. Barnes, B. C. O'Regan, A. Walsh and M. S. Islam, *Nat. commun.*, 2015, **6**, 7497.
12. H. D. Kim, H. Ohkita, H. Benten and S. Ito, *Adv. Mater.*, 2016, **28**, 917-922.
13. M. Saliba, T. Matsui, K. Domanski, J.-Y. Seo, A. Ummadisingu, S. M. Zakeeruddin, J.-P. Correa-Baena, W. R. Tress, A. Abate, A. Hagfeldt and M. Grätzel, *Science*, 2016, **354**, 206-209.
14. G. E. Eperon, S. D. Stranks, C. Menelaou, M. B. Johnston, L. M. Herz and H. J. Snaith, *Energy. Environ. Sci.*, 2014, **7**, 982-988.
15. S. De Wolf, J. Holovsky, S.-J. Moon, P. Löper, B. Niesen, M. Ledinsky, F.-J. Haug, J.-H. Yum and C. Ballif, *J. Phys. Chem. Lett.*, 2014, **5**, 1035-1039.
16. C. S. Ponseca, T. J. Savenije, M. Abdellah, K. Zheng, A. Yartsev, T. Pascher, T. Harlang, P. Chabera, T. Pullerits, A. Stepanov, J.-P. Wolf and V. Sundström, *J. A. Chem. Soc.*, 2014, **136**, 5189-5192.
17. E. M. Hutter, G. E. Eperon, S. D. Stranks and T. J. Savenije, *J. Phys. Chem. Lett.*, 2015, **6**, 3082-3090.
18. J. Burschka, N. Pellet, S.-J. Moon, R. Humphry-Baker, P. Gao, M. K. Nazeeruddin and M. Grätzel, *Nature*, 2013, **499**, 316-319.
19. M. Liu, M. B. Johnston and H. J. Snaith, *Nature*, 2013, **501**, 395-398.
20. J. H. Heo, S. H. Im, J. H. Noh, T. N. Mandal, C.-S. Lim, J. A. Chang, Y. H. Lee, H.-j. Kim, A. Sarkar, K. Nazeeruddin, M. Grätzel and S. I. Seok, *Nat. Photonics*, 2013, **7**, 486-491.
21. G. Xing, N. Mathews, S. Sun, S. S. Lim, Y. M. Lam, M. Grätzel, S. Mhaisalkar and T. C. Sum, *Science*, 2013, **342**, 344-347.
22. J. H. Noh, S. H. Im, J. H. Heo, T. N. Mandal and S. I. Seok, *Nano Lett.*, 2013, **13**, 1764-1769.

23. H.-S. Kim, I. Mora-Sero, V. Gonzalez-Pedro, F. Fabregat-Santiago, E. J. Juarez-Perez, N.-G. Park and J. Bisquert, *Nat. Commun.*, 2013, **4**.
24. N.-G. Park, *J. Phys. Chem. Lett.*, 2013, **4**, 2423-2429.
25. I. Chung, B. Lee, J. He, R. P. H. Chang and M. G. Kanatzidis, *Nature*, 2012, **485**, 486-489.
26. H.-S. Kim, C.-R. Lee, J.-H. Im, K.-B. Lee, T. Moehl, A. Marchioro, S.-J. Moon, R. Humphry-Baker, J.-H. Yum, J. E. Moser, M. Gratzel and N.-G. Park, *Sci. Rep.*, 2012, **2**.
27. E. Edri, S. Kirmayer, D. Cahen and G. Hodes, *J. Phys. Chem. Lett.*, 2013, **4**, 897-902.
28. T. Baikie, Y. Fang, J. M. Kadro, M. Schreyer, F. Wei, S. G. Mhaisalkar, M. Graetzel and T. J. White, *J. Mater. Chem. A*, 2013, **1**, 5628-5641.
29. J.-H. Im, C.-R. Lee, J.-W. Lee, S.-W. Park and N.-G. Park, *Nanoscale*, 2011, **3**, 4088-4093.
30. J. M. Ball, M. M. Lee, A. Hey and H. J. Snaith, *Energy Environ. Sci.*, 2013, **6**, 1739-1743.
31. L. Etgar, P. Gao, Z. Xue, Q. Peng, A. K. Chandiran, B. Liu, M. K. Nazeeruddin and M. Grätzel, *J. A. Chem. Soc.*, 2012, **134**, 17396-17399.
32. M. J. Carnie, C. Charbonneau, M. L. Davies, J. Troughton, T. M. Watson, K. Wojciechowski, H. Snaith and D. A. Worsley, *Chem. Commun.*, 2013, **49**, 7893-7895.
33. D. Bi, L. Yang, G. Boschloo, A. Hagfeldt and E. M. J. Johansson, *J. Phys. Chem. Lett.*, 2013, **4**, 1532-1536.
34. J.-Y. Jeng, Y.-F. Chiang, M.-H. Lee, S.-R. Peng, T.-F. Guo, P. Chen and T.-C. Wen, *Adv. Mater.*, 2013, **25**, 3727-3732.
35. P. Docampo, J. M. Ball, M. Darwich, G. E. Eperon and H. J. Snaith, *Nat. Commun.*, 2013, **4**.
36. S. Sun, T. Salim, N. Mathews, M. Duchamp, C. Boothroyd, G. Xing, T. C. Sum and Y. M. Lam, *Energy Environ. Sci.*, 2014, DOI: 10.1039/c3ee43161d.
37. J. Y. Kim, S. H. Kim, H. H. Lee, K. Lee, W. Ma, X. Gong and A. J. Heeger, *Adv. Mater.*, 2006, **18**, 572-576.
38. H. Choi, S.-J. Ko, Y. Choi, P. Joo, T. Kim, B. R. Lee, J.-W. Jung, H. J. Choi, M. Cha, J.-R. Jeong, I.-W. Hwang, M. H. Song, B.-S. Kim and J. Y. Kim, *Nat. Photonics*, 2013, **7**, 732-738.
39. J. Peet, J. Y. Kim, N. E. Coates, W. L. Ma, D. Moses, A. J. Heeger and G. C. Bazan, *Nat. Mater.*, 2007, **6**, 497-500.
40. K. Tanaka, T. Takahashi, T. Ban, T. Kondo, K. Uchida and N. Miura, *Solid State Communications*, 2003, **127**, 619-623.
41. D. B. Mitzi, *J. Mater. Chem.*, 2004, **14**, 2355-2365.
42. M. D. Perez, C. Borek, S. R. Forrest and M. E. Thompson, *J. A. Chem. Soc.*, 2009, **131**, 9281-9286.
43. J.-H. Im, J. Chung, S.-J. Kim and N.-G. Park, *Nanoscale Res. Lett.*, 2012, **7**, 353.
44. T. M. Koh, K. Fu, Y. Fang, S. Chen, T. C. Sum, N. Mathews, S. G. Mhaisalkar, P. P. Boix and T. Baikie, *J. Phys. Chem. C*, 2013, DOI: 10.1021/jp411112k.
45. S. Pang, H. Hu, J. Zhang, S. Lv, Y. Yu, F. Wei, T. Qin, H. Xu, Z. Liu and G. Cui, *Chem. Mater.*, 2014, **26**, 1485-1491.
46. Y. Zhao and K. Zhu, *J. Phys. Chem. Lett.*, 2013, **4**, 2880-2884.
47. G. E. Eperon, V. M. Burlakov, P. Docampo, A. Goriely and H. J. Snaith, *Adv. Func. Mater.*, 2014, **24**, 151-157.
48. C. C. Stoumpos, C. D. Malliakas and M. G. Kanatzidis, *Inorganic Chem.*, 2013, **52**, 9019-9038.
49. M. Nikl, K. Nitsch, J. Chval, F. Somma, A. R. Phani, S. Santucci, C. Giampaolo, P. Fabeni, G. P. Pazzi and

- X. Q. Feng, *J. Phys. Cond. Mater.*, 2000, **12**, 1939.
50. S. Kondo, A. Masaki, T. Saito and H. Asada, *Solid State Communications*, 2002, **124**, 211-214.
51. H. Zhou, Q. Chen, G. Li, S. Luo, T.-b. Song, H.-S. Duan, Z. Hong, J. You, Y. Liu and Y. Yang, *Science*, 2014, **345**, 542-546.
52. W. S. Yang, J. H. Noh, N. J. Jeon, Y. C. Kim, S. Ryu, J. Seo and S. I. Seok, *Science*, 2015, **348**, 1234-1237.
53. O. Malinkiewicz, A. Yella, Y. H. Lee, G. M. Espallargas, M. Graetzel, M. K. Nazeeruddin and H. J. Bolink, *Nat. Photonics*, 2014, **8**, 128-132.
54. C.-H. Chiang, Z.-L. Tseng and C.-G. Wu, *J. Mater. Chem. A*, 2014, **2**, 15897-15903.
55. J.-Y. Jeng, K.-C. Chen, T.-Y. Chiang, P.-Y. Lin, T.-D. Tsai, Y.-C. Chang, T.-F. Guo, P. Chen, T.-C. Wen and Y.-J. Hsu, *Adv. Mater.*, 2014, **26**, 4107-4113.
56. Y.-F. Chiang, J.-Y. Jeng, M.-H. Lee, S.-R. Peng, P. Chen, T.-F. Guo, T.-C. Wen, Y.-J. Hsu and C.-M. Hsu, *Phys. Chem. Chem. Phys.*, 2014, **16**, 6033-6040.
57. J. H. Heo, H. J. Han, D. Kim, T. K. Ahn and S. H. Im, *Energy & Environmental Science*, 2015, **8**, 1602-1608.
58. S. Colella, E. Mosconi, P. Fedeli, A. Listorti, F. Gazza, F. Orlandi, P. Ferro, T. Besagni, A. Rizzo, G. Calestani, G. Gigli, F. De Angelis and R. Mosca, *Chem. Mater.*, 2013, **25**, 4613-4618.
59. E. Mosconi, A. Amat, M. K. Nazeeruddin, M. Grätzel and F. De Angelis, *J. Phys. Chem. C*, 2013, **117**, 13902-13913.
60. E. Edri, S. Kirmayer, M. Kulbak, G. Hodes and D. Cahen, *J. Phys. Chem. Lett.*, 2014, **5**, 429-433.
61. B. Cai, Y. Xing, Z. Yang, W.-H. Zhang and J. Qiu, *Energy Environ. Sci.*, 2013, **6**, 1480-1485.
62. P. W. Liang, C. C. Chueh, X. K. Xin, F. Zuo, S. T. Williams, C. Y. Liao and A. K. Y. Jen, *Adv. Energy Mater.*, 2015, **5**, n/a-n/a.
63. H. Choi, J. Jeong, H.-B. Kim, S. Kim, B. Walker, G.-H. Kim and J. Y. Kim, *Nano Energy*, 2014, **7**, 80-85.
64. P.-W. Liang, C.-Y. Liao, C.-C. Chueh, F. Zuo, S. T. Williams, X.-K. Xin, J. Lin and A. K. Y. Jen, *Adv. Mater.*, 2014, **26**, 3748-3754.
65. A. Poglitsch and D. Weber, *J. Chem. Phys.*, 1987, **87**, 6373-6378.
66. C.-G. Wu, C.-H. Chiang, Z.-L. Tseng, M. K. Nazeeruddin, A. Hagfeldt and M. Gratzel, *Energy Environ. Sci.*, 2015, **8**, 2725-2733.
67. D. Shi, V. Adinolfi, R. Comin, M. Yuan, E. Alarousu, A. Buin, Y. Chen, S. Hoogland, A. Rothenberger, K. Katsiev, Y. Losovyj, X. Zhang, P. A. Dowben, O. F. Mohammed, E. H. Sargent and O. M. Bakr, *Science*, 2015, **347**, 519-522.
68. N. J. Jeon, J. H. Noh, W. S. Yang, Y. C. Kim, S. Ryu, J. Seo and S. I. Seok, *Nature*, 2015, **517**, 476-480.
69. T. M. Brenner, D. A. Egger, L. Kronik, G. Hodes and D. Cahen, *Nat. Rev. Mater.*, 2016, **1**, 15007.
70. G. F. Burkhard, E. T. Hoke and M. D. McGehee, *Adv. Mater.*, 2010, **22**, 3293-3297.
71. L. M. Herz, *Annu. Rev. Phys. Chem.*, 2016, **67**, 65-89.
72. M. B. Johnston and L. M. Herz, *Acc. Chem. Res.*, 2016, **49**, 146-154.
73. M. Liu, M. B. Johnston and H. J. Snaith, *Nature*, 2013, **501**, 395.
74. O. Malinkiewicz, A. Yella, Y. H. Lee, G. M. Espallargas, M. Graetzel, M. K. Nazeeruddin and H. J. Bolink, *Nat. Photonics*, 2013, **8**, 128.
75. Y. Deng, Q. Dong, C. Bi, Y. Yuan and J. Huang, *Adv. Energy Mater.*, 2016, **6**, n/a-n/a.

76. T. Liu, K. Chen, Q. Hu, R. Zhu and Q. Gong, *Adv. Energy Mater.*, 2016, **6**, 1600457-n/a.
77. J. Jeong, H.-B. Kim, H. Kim, B. Walker, S. Song, J. Heo, Y. J. Yoon, Y. Jo, H. Choi, G.-H. Kim, D. S. Kim and J. Y. Kim, *Acs Energy Lett.*, 2016, **1**, 712-718.
78. M. Saliba, T. Matsui, J.-Y. Seo, K. Domanski, J.-P. Correa-Baena, M. K. Nazeeruddin, S. M. Zakeeruddin, W. Tress, A. Abate, A. Hagfeldt and M. Gratzel, *Energy. Environ. Sci.*, 2016, **9**, 1989-1997.
79. Y. Bai, X. Meng and S. Yang, *Adv. Energy Mater.*, 2017, DOI: 10.1002/aenm.201701883, 1701883.
80. Y. Jo, K. S. Oh, M. Kim, K.-H. Kim, H. Lee, C.-W. Lee and D. S. Kim, *Adv. Mater. Inter.*, 2016, **3**, 1500768-n/a.
81. Y. Shao, Y. Yuan and J. Huang, *Nat. Energy*, 2016, **1**, 15001.
82. L. Meng, J. You, T.-F. Guo and Y. Yang, *Acc. Chem. Res.*, 2016, **49**, 155-165.
83. J. Burschka, N. Pellet, S.-J. Moon, R. Humphry-Baker, P. Gao, M. K. Nazeeruddin and M. Grätzel, *Nature*, 2013, **499**, 316.
84. J. H. Heo, D. H. Song, H. J. Han, S. Y. Kim, J. H. Kim, D. Kim, H. W. Shin, T. K. Ahn, C. Wolf, T.-W. Lee and S. H. Im, *Adv. Mater.*, 2015, **27**, 3424-3430.
85. D. Luo, L. Zhao, J. Wu, Q. Hu, Y. Zhang, Z. Xu, Y. Liu, T. Liu, K. Chen, W. Yang, W. Zhang, R. Zhu and Q. Gong, *Adv. Mater.*, 2017, **29**, 1604758-n/a.
86. R. Lindblad, D. Bi, B.-w. Park, J. Oscarsson, M. Gorgoi, H. Siegbahn, M. Odelius, E. M. J. Johansson and H. Rensmo, *J. Phys. Chem. Lett.*, 2014, **5**, 648-653.
87. T.-W. Ng, H. Thachoth Chandran, C.-Y. Chan, M.-F. Lo and C.-S. Lee, *Acs Appl. Mater & Inter.*, 2015, **7**, 20280-20284.
88. Z. Wu, S. Bai, J. Xiang, Z. Yuan, Y. Yang, W. Cui, X. Gao, Z. Liu, Y. Jin and B. Sun, *Nanoscale*, 2014, **6**, 10505-10510.
89. Y. Yang, S. Feng, M. Li, W. Xu, G. Yin, Z. Wang, B. Sun and X. Gao, *Sci. Rep.*, 2017, **7**, 46724.
90. L. J. A. Koster, V. D. Mihailetschi, R. Ramaker and P. W. M. Blom, *Appl. Phys. Lett.*, 2005, **86**, 123509.
91. M. Liu, M. Endo, A. Shimazaki, A. Wakamiya and Y. Tachibana, *J. Photo. Sci. Technology*, 2017, **30**, 577-582.
92. R. S. Sanchez, V. Gonzalez-Pedro, J.-W. Lee, N.-G. Park, Y. S. Kang, I. Mora-Sero and J. Bisquert, *J. Phys. Chem. Lett.*, 2014, **5**, 2357-2363.
93. Q. Wang, C. Bi and J. Huang, *Nano Energy*, 2015, **15**, 275-280.
94. M. Kaltenbrunner, G. Adam, E. D. Głowacki, M. Drack, R. Schwödiauer, L. Leonat, D. H. Apyaydin, H. Groiss, M. C. Scharber and M. S. White, *Nat. Mater.*, 2015, **14**, 1032.
95. M. B. Schubert and J. H. Werner, *Mater. Today*, 2006, **9**, 42-50.
96. S. Pan, Z. Yang, P. Chen, J. Deng, H. Li and H. Peng, *Ange. Chemi*, 2014, **126**, 6224-6228.
97. Z. Liu, P. You, C. Xie, G. Tang and F. Yan, *Nano Energy*, 2016, **28**, 151-157.
98. X. Zhang, V. A. Öberg, J. Du, J. Liu and E. M. Johansson, *Energy. Environ. Sci.*, 2018.
99. M. Kaltenbrunner, M. S. White, E. D. Głowacki, T. Sekitani, T. Someya, N. S. Sariciftci and S. Bauer, *Nat. commun.*, 2012, **3**, 770.
100. Y. Li, L. Meng, Y. M. Yang, G. Xu, Z. Hong, Q. Chen, J. You, G. Li, Y. Yang and Y. Li, *Nat. commun.*, 2016, **7**, 10214.
101. T. Liu, K. Chen, Q. Hu, R. Zhu and Q. Gong, *Advanced Energy Materials*, 2016, **6**, n/a-n/a.

102. Y. Bai, X. Meng and S. Yang, *Adv. Energy Mater.*, DOI: 10.1002/aenm.201701883, n/a-n/a.
103. M. M. Lee, J. Teuscher, T. Miyasaka, T. N. Murakami and H. J. Snaith, *Science*, 2012, 1228604.
104. K. Ellmer, *Nat. Photonics*, 2012, **6**, 809.
105. A. Kumar and C. Zhou, *ACS nano*, 2010, **4**, 11-14.
106. F. Guo, H. Azimi, Y. Hou, T. Przybilla, M. Hu, C. Bronnbauer, S. Langner, E. Spiecker, K. Forberich and C. J. Brabec, *Nanoscale*, 2015, **7**, 1642-1649.
107. A. Kim, H. Lee, H.-C. Kwon, H. S. Jung, N.-G. Park, S. Jeong and J. Moon, *Nanoscale*, 2016, **8**, 6308-6316.
108. E. Lee, J. Ahn, H. C. Kwon, S. Ma, K. Kim, S. Yun and J. Moon, *Adv. Energy Mater.*, 2018, **8**, 1702182.
109. S. Seo, I. Jeon, Y. Sato, C. Delacou, A. Anisimov, K. Suenaga, E. Kauppinen, Y. Matsuo and S. Maruyama, *B. A. Phys. Soc.*, 2018.
110. Z. Li, S. A. Kulkarni, P. P. Boix, E. Shi, A. Cao, K. Fu, S. K. Batabyal, J. Zhang, Q. Xiong and L. H. Wong, *ACS nano*, 2014, **8**, 6797-6804.
111. Q. Luo, H. Ma, Q. Hou, Y. Li, J. Ren, X. Dai, Z. Yao, Y. Zhou, L. Xiang and H. Du, *Adv. Func. Mater.*, 2018.
112. D. Bryant, P. Greenwood, J. Troughton, M. Wijdekop, M. Carnie, M. Davies, K. Wojciechowski, H. J. Snaith, T. Watson and D. Worsley, *Adv. Mater.*, 2014, **26**, 7499-7504.
113. S. Kang, T. Kim, S. Cho, Y. Lee, A. Choe, B. Walker, S.-J. Ko, J. Y. Kim and H. Ko, *Nano Lett.*, 2015, **15**, 7933-7942.
114. S. Cho, S. Kang, A. Pandya, R. Shanker, Z. Khan, Y. Lee, J. Park, S. L. Craig and H. Ko, *ACS nano*, 2017, **11**, 4346-4357.
115. S. De, T. M. Higgins, P. E. Lyons, E. M. Doherty, P. N. Nirmalraj, W. J. Blau, J. J. Boland and J. N. Coleman, *ACS nano*, 2009, **3**, 1767-1774.
116. J.-Y. Lee, S. T. Connor, Y. Cui and P. Peumans, *Nano Lett.*, 2008, **8**, 689-692.
117. L. Hu, H. S. Kim, J.-Y. Lee, P. Peumans and Y. Cui, *ACS nano*, 2010, **4**, 2955-2963.
118. V. Scardaci, R. Coull, P. E. Lyons, D. Rickard and J. N. Coleman, *Small*, 2011, **7**, 2621-2628.
119. W. Xiong, H. Liu, Y. Chen, M. Zheng, Y. Zhao, X. Kong, Y. Wang, X. Zhang, X. Kong and P. Wang, *Adv. Mater.*, 2016, **28**, 7167-7172.
120. W. Gaynor, G. F. Burkhard, M. D. McGehee and P. Peumans, *Adv. Mater.*, 2011, **23**, 2905-2910.
121. J. Burschka, N. Pellet, S.-J. Moon, R. Humphry-Baker, P. Gao, M. K. Nazeeruddin and M. Grätzel, *Nature*, 2013, **499**, 316.
122. Z. Xiao, Q. Dong, C. Bi, Y. Shao, Y. Yuan and J. Huang, *Adv. Mater.*, 2014, **26**, 6503-6509.
123. H. Back, J. Kim, G. Kim, T. K. Kim, H. Kang, J. Kong, S. H. Lee and K. Lee, *Sol. Energy Mater. Sol. Cells*, 2016, **144**, 309-315.
124. B. V. Crist, *XPS Reports*, 2007, **1**.
125. B. Crist, *A review of XPS data-banks*, 1990.
126. H.-B. Kim, H. Choi, J. Jeong, S. Kim, B. Walker, S. Song and J. Y. Kim, *Nanoscale*, 2014, **6**, 6679-6683.
127. Y. Fang, Z. Wu, J. Li, F. Jiang, K. Zhang, Y. Zhang, Y. Zhou, J. Zhou and B. Hu, *High-Performance Hazy Silver Nanowire Transparent Electrodes through Diameter Tailoring for Semitransparent Photovoltaics*, 2018.

128. T. Liu, W. Q. Liu, Y. T. Zhu, S. P. Wang, G. Wu and H. Z. Chen, *Sol. Energy Mater. Sol. Cells*, 2017, **171**, 43-49.
129. J. Han, S. Yuan, L. Liu, X. Qiu, H. Gong, X. Yang, C. Li, Y. Hao and B. Cao, *J. Mater. Chem. A*, 2015, **3**, 5375-5384.
130. E. Lee, J. Ahn, H.-C. Kwon, S. Ma, K. Kim, S. Yun and J. Moon, *Adv. Energy Mater.*, 2018, **8**, 1702182.

Acknowledgements

무엇인가 완전히 익히기엔 짧은, 그렇지만 지식의 미숙함을 지각하기엔 충분했던 시간이 흘러, 어느덧 올 것 같지 않았던 박사학위 논문을 마무리 지어야 할 때가 되었습니다. 학위 시작 전 가지고 있었던, 새로운 시작에 대한 설렘과 두려움이 아득한 기억의 조각으로 희미해져 가고 당시의 열정이 제가 되어 사라질 때마다 저에게 동기부여를 해주고 새로운 열정의 씨앗을 심을 수 있도록 제 옆에서 지켜보면서 끊임없는 힘을 주신 많은 분들에게 이 글을 통해 감사의 마음을 전하고자 합니다.

먼저 이 논문을 완성할 수 있도록 적극적인 지원과 조언을 아낌없이 주신 김진영 교수님께 감사 인사를 전합니다. 처음에 찾아 뵈는 때 물리학과 출신이라고 좋아하셨던 모습이 기억에 선명한데 교수님의 기대에 잘 보답하였는지 모르겠습니다. 논문의 주제가 연구실에서 새롭게 시작하는 것이고 세계적으로 활발히 연구되는 중이라 많은 시간과 노력이 필요 했는데 조금 더 잘 할 수 있지 않았을까 하는 아쉬움이 남습니다. 하지만 교수님께서 기다려 주시고 격려 해주신 덕분에 많은 결과를 낼 수 있었습니다. 다시 한번 감사하고 존경합니다.

제 부족한 논문을 발전시키는데 많은 교수님들께서 도움을 주셨습니다. 먼저 석사과정 동안 연구를 하는 방법과 기본자세에 대해서 알려주신 박혁규 교수님, 논문 심사 때 유익한 조언을 많이 해주신 석상일 교수님, 엘지 디스플레이 과제를 같이 하면서 새로운 도전에 접근하는 방법과 방향을 알려주신 송명훈 교수님, 태양전지를 이용한 응용연구를 할 수 있게 도와주신 고현협 교수님, 연구하다가 막히는 부분이 있을 때 마다 항상 적절한 조언과 도움을 주신 한국에너지기술연구원 김동석 센터장님과 조임현 박사님께도 감사의 인사를 전합니다.

긴 시간동안 함께 동거동락했던 NREL 구성원들에게도 고마움을 전합니다. 처음 연구실 왔을때부터 남달랐던 효성이, 진정한 학자의 길이 먼저 잘 보여줬지만 마피아는 못하는 김성범 교수님, 부족한 영어를 척하면 척 알아듣고 쉽게 설명해줬던 Bright 명보 교수님, 물어보고 실험할 것이 많았는데 너무 짧게 있다가 떠나신 이정훈 교수님, 최근 2년동안 많이 괴롭혔는데 잘 받아준 기환이형, 그래도 많은 결과 낼 수 있어서 다행이라고 생각해요. 최근 한국으로 돌아온 서진이형, 예전에 야식 먹으면서 이것저것 토크했던 거 다시 할 수 있었음 좋겠네요. 실험실 식구들의 부러움을 많은 받고 있는 국제 커플 명희, 남반구에서 너무나도 안락한 생활을 하고 있는 태효, 조만간 다시 한국에 돌아올

수 있을거여. 인생선배이자 아직 대면대면 어색어색 한 헤림이, 이제 좀 친해지려니 졸업이네요. 그리고 중국 네이티브라고 자주 놀렸는데 끝까지 한결 같은 반응해준 세영이, 알겠지만 미안하진 않아~. 처음부터 지금까지 비슷한 주제로 같이 열심히 하고 고생한 학범이도 수고 많았고 양보해준 주제도 보답해야 되는데 기회가 있었음 좋겠네. 그리고 실험실 처음 들어왔을 때부터 말동무 잘해주고 박학다식한 정우, 축하하고 앞으로도 자주 애용할게. 입렐 동기인 송이도 앞으로 남은 거 마무리 잘하고 디펜스 무사히 마치길 바랄게. 이제 후배님들 남았네. 묵묵하고 조용히 할 일 잘하는 택호, 우리 실험실의 golden generation 중 첫째인 강택이, 같이 TEG 열심히 공부했는데 기대했던 것 보다 성과가 만나와 아쉬운 나경이, 담에 다른 기회에 뭉쳐보자. 형들 말 잘 따라주고 잘 따라준 영진이, XPS, UPS 찍어준다고 정말 수고했다. 나한테 잔소리 많이 들은 재원이도 한 단계씩 발전하는걸 보니 신기하다. 그리고 같은 팀원인 형수, 새로운 곳에서 많은 지식을 배워오길, 윤섭이도 축구실력만큼 연구성과를 내길 기대할게. 신입생답지 않은 패기로움을 보여준 초, 실험실 구성원 모두 리스펙하는 지우, 학부 때부터 열심히 연구실 다니는 우진이까지 같은 팀이 아니라 많이 부딪혀 보지 못해 아쉽네. 마지막으로 늦깎이 대학원생 인생 선배인 종득이도 앞으로 대성하길~ 최선을 다해 도와줄게.

지친 일상에 활력을 준 친구들에게도 감사함을 전합니다. 먼저 고등학교 때부터 이어져온 진유모 친구들 태경, 영섭, 기욱, 영현, 현진, 지황, 구태, 현진, 형석, 귀봉, 종욱, 이제는 다들 한 가정의 가장이 되거나 배불뚝이 아재들이 되었지만 항상 고등학교 모습 그대로인게 참 답답하고 신기하네, 남아있는 놈들도 분발하자. 학부 때부터 같이 고생한 동기 규범, 기락, 승현, 지용, 현우, 영진, 중희, 형민, 승훈형, 이제 만나기 쉽지 않지만 각자의 자리에서 최선을 다하자. 그리고 내가 수용할 수 없는 흥을 가지고 있는 영남, 8월에 큰 행사를 준비하고 있는 새로미, 학위 받는다고 고생했고 둘 다 슬슬 맛먹는데 아직 난 맘의 준비가 안됐다.

끝으로 항상 손자에게 웃으면서 모든 걸 아낌없이 주시는 할아버지, 할머니, 동생, 오랫동안 꾸준히 옆에서 친구처럼 머물러준 희진이, 마지막으로 믿음직하지 못한 아들을 항상 믿고 꾸준히 지지해 주신 부모님께 제 작은 결실을 받칩니다.